北海道大学大学院情報科学院

[博士論文]

Study on Hybrid-Type PM Motor for BEV/HEV Traction to Reduce PM Cost

PM コスト低減のための BEV/HEV 牽引用ハイブリッドタイプ PM モーターに関する研究

令和 5 年 3 月

主指導教員　小笠原 悟司　教授

提出者

専攻　情報科学専攻

学生番号　46195208

学生氏名　朴　志成

Abstract

According to international carbon dioxide emission regulations, the demand for eco-friendly vehicles is rapidly increasing. The core technology of eco-friendly cars is electrification. A traction motor is a key component for the implementation of electrification. Traction motors require high power density and wide variable speed operation. Therefore, the inner permanent magnet synchronous motor (IPMSM) is mainly adopted. High energy density NdFeB sintered magnet (Nd-PM) is applied to IPMSM for traction motor. The core materials of Nd-PM are neodymium (Nd), a light rare earth, and dysprosium (Dy), a heavy rare earth. Due to the problem that these raw materials are exclusively mined in a specific country, the price skyrocketed in 2011, which became a big problem in the industrial aspect. Therefore, there is a strong demand in the industry for technologies that do not use or reduce these raw materials.

As an existing research case that can reduce the use of rare earth, there is a hybrid type permanent magnet motor (HPMM). HPMM is a motor that uses low-cost ferrite magnets (Fe-PM) to partially replace Nd-PM. However, most of the existing research cases are within 5kW and do not sufficiently reflect the characteristics required for traction motors for automobiles.

Therefore, in this study, compared to traction motors for automobiles that are actually mass-produced, we propose a novel HPMM that can reduce PM price and minimize the use of rare earth under the same torque and power density.

In this study, two types of target motors are presented. The first is a traction motor for the NISSAN LEAF electric vehicle, and the second is a traction motor for the TOYOTA PRIUS 4th generation hybrid vehicle. Benchmarking is performed for each target motor, and a new HPMM topology is proposed under the same stator structure as the target motor. The proposed HPMM meets the durability and efficiency characteristics required in automobiles and achieves the same power density as the target motor.

Keywords: Permanent magnet synchronous motor, NdFeb PM, Ferrite PM, Hybrid PM motor, Dy-free PM, Demagnetization durability, Switching ripple current, Enhancing efficiency.

Contents

Chapter 1. Introduction

1.1 Background and Trend

The history of electric motors began with the discovery of electromagnetic phenomena in the first half of the 19th century. DC motors, induction motors (IM), and synchronous motors (SM) were developed in the late 19th century and put into practice in the early 20th century. Since then, due to the development of magnetic materials, power control semiconductors, and control techniques, various electric motors have achieved small size and weight reduction, high output and high efficiency, and many developments have been made.

DC motor are historically the oldest and are easy to control. However, since there is a rectifying mechanism in the structure, wear occurs due to mechanical contact during rotation, which is disadvantageous for variable speed high-speed driving. In recent years, the variable speed drive system is being replaced by an IM or SM.

The IM is simple in structure and robust. In addition, the degree of completion is high because the research on the control system has been long. However, the efficiency is low in the low-speed operation region, and copper loss is always generated by the slip phenomenon inside the rotor.

Recently, due to the development of high-performance permanent magnet (PM), PMSMs with improved power density and efficiency compared to conventional SMs have been in the spotlight. In PMSM, the field flux is not dependent on an external power source, but is supplied by PMs. As a result, the efficiency and power density are higher than other motors. In addition, due to the development of rare-earth magnets such as neodymium-PM (Nd-PM), which have high energy density, research on replacing existing systems with PMSM in each field has been actively conducted. In particular, it is actively applied to the driving field of eco-friendly vehicles such as electric vehicles (EV) and hybrid electric vehicles (HEV), and PMSM with Nd-PM has become the mainstream of traction motors for vehicles.

PMSM are classified into surface-mounted PM synchronous motors (SPMSM) and Interior PM synchronous motors (IPMSM) by mechanical structure. SPMSM has a magnet attached to the rotor surface, so there is a risk of scattering during high-speed rotation. In addition, since the magnetically effective air gap is large, the armature reaction is small, which limits high-speed operation.

On the other hand, IPMSM can prevent the scattering of the PM by centrifugal force by inserting the PM into the core of the rotor. IPMSM can generate not only PM torque by magnet but also reluctance torque that SPM does not have, which has high torque density and is advantageous for high-speed operation [1-7]. In addition, since the degree of design freedom is high, it is advantageous to improve performance through various optimization techniques, etc. [8-11]. Due to these advantages, IPMSM is mainly adopted and studied for traction motors for vehicles that require high output in a wide range of speed [12-27]. In addition, in recent years, eco-friendly vehicles such as EVs and HEVs are rapidly emerging as alternative solutions in the transportation sector to reduce dependence on fossil fuels and reduce emissions [28-31]. Therefore, it can be expected that the demand for IPMSM will increase explosively due to the active dissemination of eco-friendly vehicles.

Nd-PM is mainly applied to IPMSM for vehicle traction and it is the most widely used rare earth magnet [32]. Nd-PM was developed by General Motors and Sumitomo Special Metals in 1984, respectively, and can be divided into sintered type and bonded type according to the manufacturing process [33-35]. Nd-PM has the highest energy density among existing PM [36-38], and the sintered type is mainly used for traction motors for vehicles. In addition, Nd-PM containing some heavy rare earths such as dysprosium (Dy) and terbium (Tb) have been applied to maintain sufficient coercive force in high temperature environmental conditions [39]. However, there is a problem with stable supply as most of the major raw materials such as Nd, Dy, and Tb are mined in a specific country. In 2011, the price of each raw material soared, causing a major blow to the industry [40-42].

Although Nd-PM occupies a small volume and weight in the entire motor system, it is very expensive, so it occupies a high proportion in terms of cost [43, 44]. Due to this risk of Nd-PM, non-rare earth traction motors have been actively studied to replace the conventional IPMSM for traction. Representative examples include separately excited synchronous motor (SESM) [45, 46], switched reluctance motor (SRM) [47-53], synchronous reluctance motor (SynRM) [54, 55], ferrite PM (Fe-PM) based motor [56-63], and IM [64-66]. A disadvantage of SESM is the wear of the contact brushes. To overcome this, in [46], a non-contact field power supply system using a rotary transformer method was constructed. However, the non-contact field power system is very expensive, and since each device is attached in the axial direction of the motor, it is

disadvantageous compared to the IPMSM in terms of system volume. SRM has a problem of acoustic noise due to structural reasons, and SynRM has a high reactive power component and low power factor, resulting in low power density. Fe-PM based motor has low torque density because the remanence of Fe-PM is 1/3 of that of Nd-PM. In addition, Fe-PM, unlike Nd-PM, has a property of easily losing magnetism at low temperatures, and does not provide a solution to this problem. IM was applied and commercialized in early models such as Tesla Model S, but it was replaced with IPMSM after Model 3, the latest model, to improve mileage and reduce weight. Therefore, non-rare earth motors are not a realistic alternative as traction motors for vehicles, and there are few commercial cases for traction for vehicles or they are being replaced by IPMSM.

Recently, there are studies on hybrid-type PM motors (HPMM) that simultaneously apply Fe-PM to the rotor to realize the same torque density as IPMSM and reduce the Nd-PM usage [67-74]. Existing research cases of HPMM can be divided into parallel type (P-HPMM) and series type (S-HPMM) based on the *d*-axis magnetic equivalent circuit. However, in the conventional HPMM research, most of the motor output range is 5 kW or less, and research on the parallel type in which magnetic flux concentration is advantageous is mainly dealt with. Traction motors for HEV and EV range in output from 30kW to 200kW. In addition, a review of high torque density, demagnetization reliability in consideration of vehicle environmental temperature conditions, and mechanical stability according to high-speed rotation is required for vehicle traction motors [75-77]. Since most of the research results of the conventional HPMM are in the category of small motors, these characteristics required for vehicles are not sufficiently reflected. Therefore, it is necessary to present an alternative that can prepare for the expansion of the eco-friendly vehicle market, minimize the resource risk of Nd-PM and reduce the PM cost through research on the topology of HPMM that fully considers the characteristics of the vehicle.

1.2 Purpose and Outline

The purpose of this study is to propose a novel HPMM that can reduce the use of Nd-PM and PM cost compared to a commercialized target motor by considering the characteristics of the vehicle. The target car models are BEV and HEV, and finally, two types of HPMM topologies are proposed.

The structure of this thesis is as follows.

Chapter 1 summarizes the research background, trend, purpose, and outline of the thesis.

Chapter 2 introduces HPMM and examines structural characteristics, classification, and PM materials. It also explains the electrification system for eco-friendly vehicles and the considerations required for vehicles. In addition, since HPMM belongs to the category of PMSM, the main mathematical characteristic equations for PMSM are introduced.

Chapter 3 proposes an HPMM for BEV traction with improved reluctance torque. The target motor is a 120kW NISSAN LEAF traction motor. A sample of the target motor was obtained, and disassembly and specification analysis were performed. The performance characteristics and problems of the conventional parallel-type (P-HPMM) and series-type HPMM (S-HPMM) under the same stator structure as the target motor will be described. In addition, to improve the problems of the conventional HPMM, a novel HPMM is proposed, and a design concept, process, and performance characteristics are presented. Finally, the validity of the proposed topology is verified through detailed comparison with the target motor.

Chapter 4 proposes an HPMM for HEV traction to which Dy-free Nd-PM is applied. Dy is one of the heavy rare earth elements with high price volatility, and is contained in a small amount to improve the coercive force of Nd-PM. Due to the development of manufacturing technologies for Nd-PM such as fine powdering and Dy diffusion process, it is possible to realize a coercive force of up to 21 kOe without Dy [78, 79]. However, Nd-PM of 25 kOe or more is mostly used for traction motors for vehicles due to environmental temperature conditions [80]. Nd-PM tends to lose magnetism at high temperatures, whereas Fe-PM, on the other hand, is robust at high temperatures. Therefore, this chapter examines whether each PM can create synergy with each other in terms of demagnetization durability under the HPMM structure, and proposes an HPMM with similar performance to the target motor. The target motor is a 53kW Toyota PRIUS 4th MG2 traction motor. As in Chapter 3, the sample of the actual target motor was disassembled and the specifications were analyzed. Two parallel models and two series models are presented under the

same structure as the target motor, and Dy-free HPMM suitable for HEV is proposed through comparison of each model.

Chapter 5 describes the efficiency characteristics considering the switching ripple current. The comparative models are the target IPMSM and the finally proposed HPMM presented in Chapter 4. In actual motor driving, it is driven by a current that reflects harmonics of several orders of magnitude. Therefore, Chapter 5 presents methods for generating harmonic currents with inverter switching frequencies from 5 kHz to 20 kHz. In addition, the efficiency characteristics of the two models are analyzed based on the current waveform. The analysis results prove that the proposed HPMM is superior in terms of efficiency compared to the target IPMSM.

Chapter 6 discusses the results of this study and future plans.

Chapter 2. Overview of Hybrid PM Motor for Vehicle Traction

2.1 BEV and HEV Electrification Systems

The eco-friendly vehicle market, such as battery electric vehicle (BEV) and hybrid electric vehicle (HEV), is undergoing rapid growth. As shown in Fig. 2.1, rapid growth is expected to continue in the future through response to the strengthening of fuel economy regulations by major automakers and policy support from each country. The short mileage, which has been a major drawback of BEV, is being improved dramatically due to the development of lithium-ion batteries with high energy density.

Eco-friendly vehicles can be classified as shown in Table 2.1 according to the driving method, and there are representative BEV and HEV. An electric vehicle is a system that uses electric energy stored in a battery to generate mechanical power through a power conversion device and an electric motor and transmit it to the wheel. HEV is a system in which an internal combustion engine (ICE), an electric motor, and a control module are simultaneously mounted. The main power is generated preferentially in the ICE, and the power of the electric device plays a secondary role. The main roles of the electric motor and control module in the HEV are to assist the power so that the engine can be operated at the optimum efficiency point, regenerative braking, and to drive the EV in some speed sections.

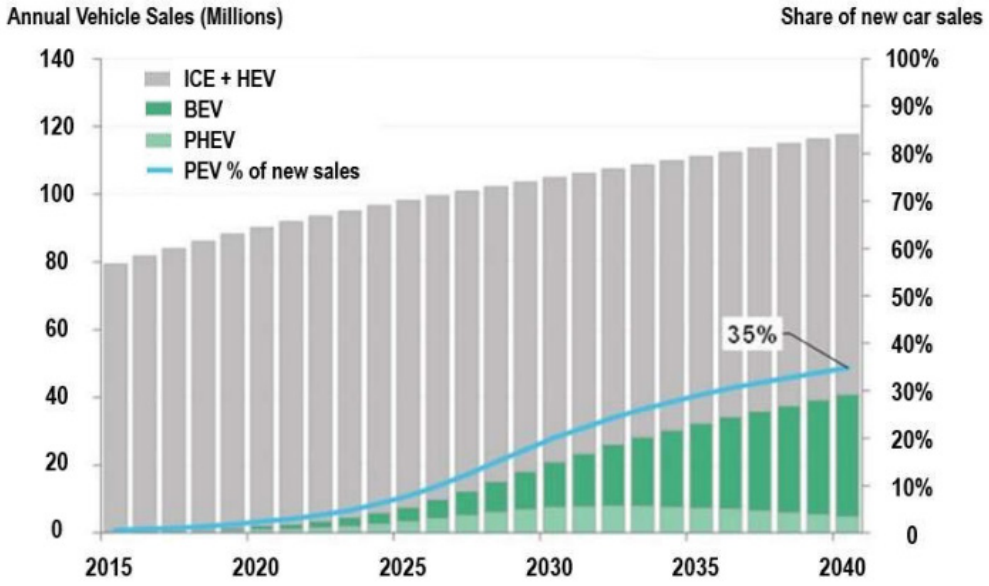

Fig. 2.1 Projected EDV sales [44].

Table 2.1 Electric vehicle classification according to the driving method

Classification	Battery electric vehicle (BEV)	Hybrid electric vehicle (HEV)
Driving source	Electric machine	Electric machine+ [1)]ICE
Power source	Electricity	Electricity + Coal fuel
Drive type	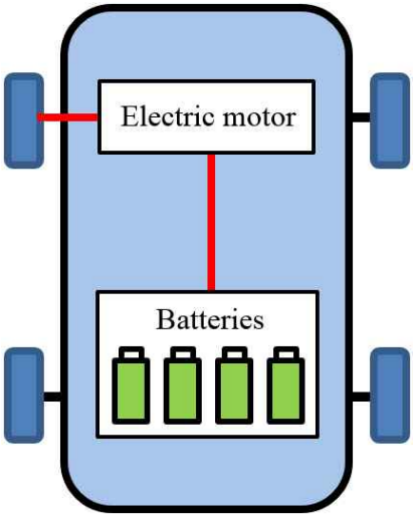	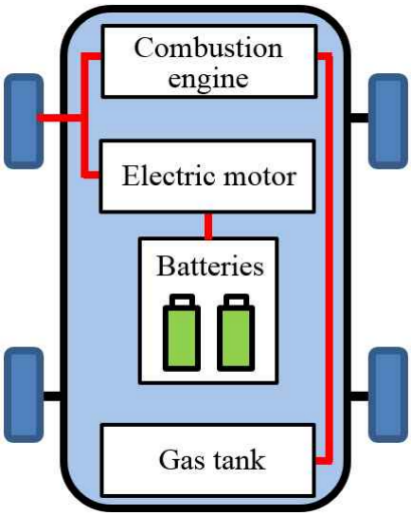
Features	Zero emission Need to charge	No charging required Exhaust gas present

[1)]internal combustion engine

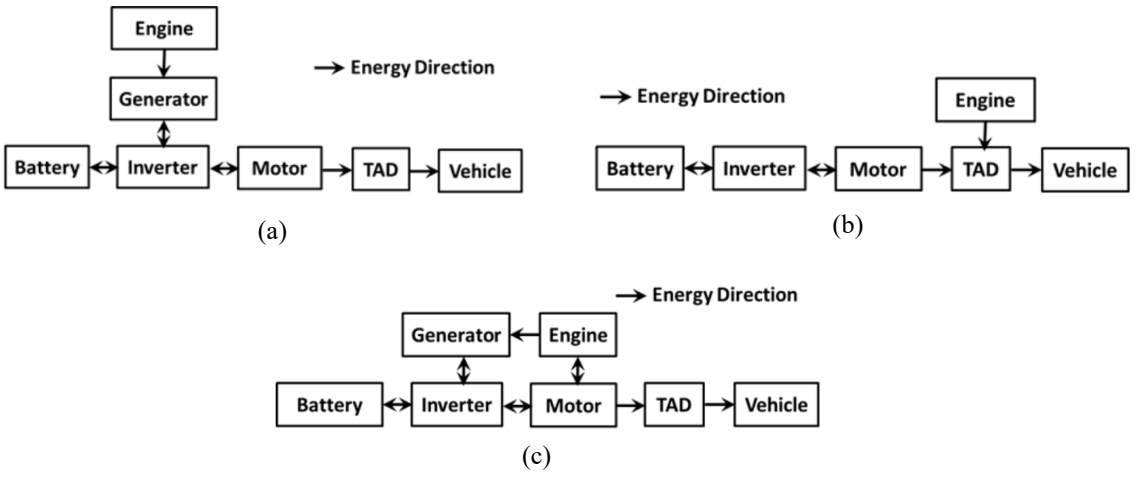

Fig. 2.2 Three typical types of HEV (a) Series (b) Parallel (c) Split [81].

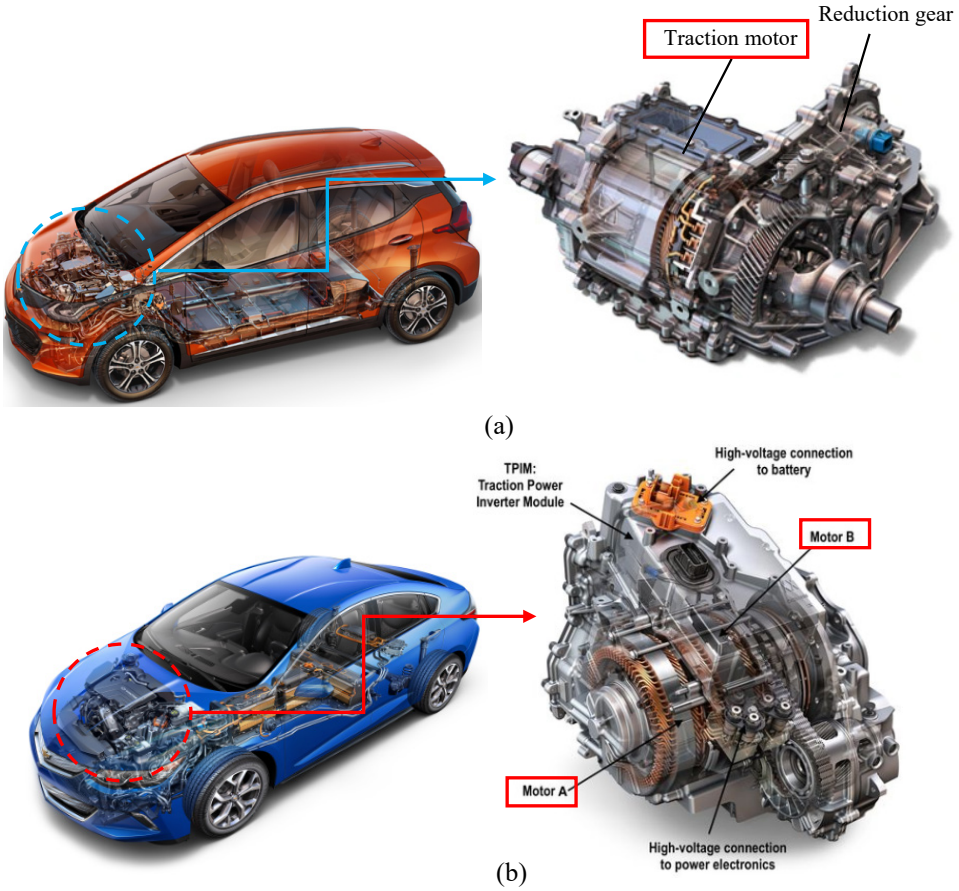

Fig. 2.3 BEV and HEV drive unit (a) GM Bolt EV [84] (b) GM Volt HEV [85]

In the case of such HEV, as shown in Fig. 2.2, according to the configuration and energy flow of ICE, motor, and generator, it can be divided into parallel type, series type, and split type.

The series HEV obtains regenerative power according to the vehicle's motion state and enables the engine to operate in efficient conditions. However, more energy transfer steps lead to more power loss. Compared to series hybrids, parallel hybrids have lower energy conversion losses because engine power is transmitted directly to the driven wheels. Split hybrids are the combination of series hybrids and parallel hybrids. Parallel and split configurations provide better fuel economy than series configurations under highway driving conditions. The split configuration boasts high fuel efficiency not only in city driving but also in highway driving [82]. Therefore, most full-hybrid cars such as Toyota Prius, Toyota Lexus, GM, Chrysler and Ford Fusion Hybrid adopt a split configuration [16, 18, 83].

Fig. 2.3 is an example of a drive unit of BEV and HEV. As a typical commercialization example,

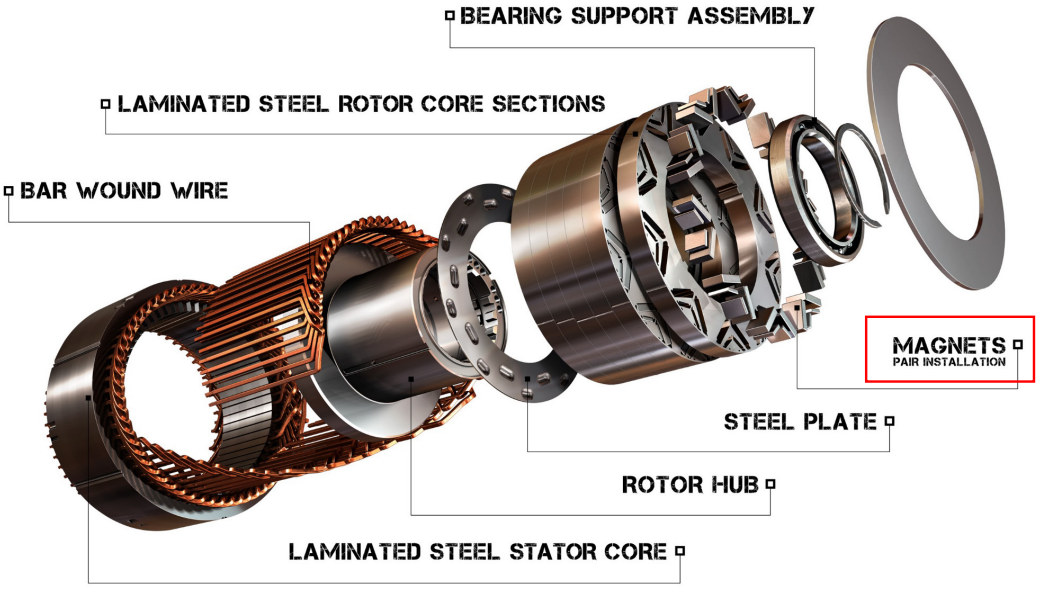

Fig. 2.4 Exploded view of traction motor (GM Volt Motor B) [86]

there are GM Bolt EV and GM Volt HEV. The drive unit for BEV has a structure in which the reducer is combined on the same axis as the traction motor. The reduction ratio of the reducer varies from 5:1 to 13:1, and technology development is progressing in the direction of increasing the reduction ratio in order to reduce the weight of the motor and improve the performance of the vehicle. In addition, most of the traction motors for BEV adopt a cylindrical structure. The HEV drive unit is mounted near the ICE, and as shown in Fig. 2.2, it is composed of a 1-motor or 2-motor system depending on the characteristics of the HEV system. Due to the characteristic of being mounted in a narrow space near the output shaft of the ICE, the structure of the motor is mostly pancake type. That is, the HEV motor has a large outer diameter and a small stack structure.

Fig. 2.4 is a exploded view of the active part of the traction motor. The main components of the active part of the traction motor are the stator and the rotor. The stator consists of a high-conductivity copper coil, an electrical steel plate, and an insulator. A current is conducted through the coil, and a magnetic field is generated due to the conducted current. The generated magnetic field exists in the form of magnetic flux density through an electric steel sheet with high magnetic permeability. An insulating material such as insulation paper is inserted between the coil and the electric steel sheet for insulation. The rotor is composed of an electric steel plate, a PM, and a shaft. The magnetic flux of the permanent magnet of the rotor and the magnetic flux generated

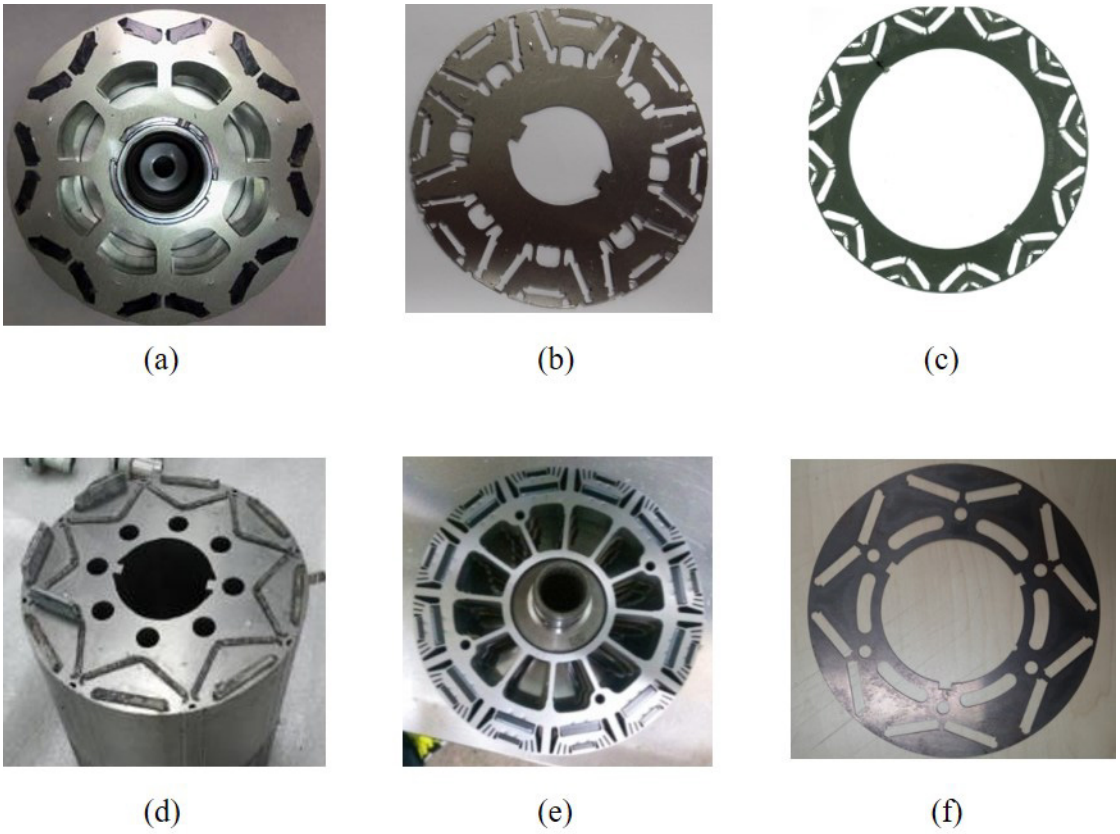

Fig. 2.5 Rotor structure of traction motor for BEV and HEV (a) Toyota Prius 3rd HEV (b) Toyota Prius 4th HEV (c) GM Volt 2nd HEV (d) Nissan Leaf EV (e) BMW i3 EV (f) Ford Focus EV

from the electric energy of the stator are interlinked and stored in the form of magnetic energy in the air gap. Magnetic energy is converted into a mechanical output form through the shaft according to the phase change with time. When a high energy density PM such as Nd-PM is applied to the rotor, field magnetic flux can be continuously generated without external power supply. Therefore, it is possible to improve the efficiency of the motor and suppress heat generation of the rotor.

Fig. 2.5 is an example of the rotor structure of the traction motors of BEVs and HEVs released so far. Most of them adopt PMSM, and high energy density Nd-PM are applied to the rotor. As mentioned in Chapter 1, Nd-PM is a high-risk material in terms of price and supply stability. The characteristics of Nd-PM and PMSM will be dealt with in detail in Sections 2.3 and 2.4.

2.2 Considerations as Vehicle Traction Motor

A traction motor for a vehicle requires a very high torque density to be mounted in a limited

space and to improve mileage or fuel efficiency. This is because the size of the motor is proportional to the torque. Therefore, very high coil current density is applied to reduce the size of the motor. When the coil current density becomes high, copper loss increases in the stator coil, generating heat, and causing a rapid temperature rise of the coil. A sudden rise in temperature may cause a reduction in the life of the motor's insulation system, as well as demagnetization of the PM. In order to prevent such temperature rise, most of the traction motors are applied with cooling technologies such as water cooling or oil direct injection. Under these cooling conditions, the coil temperature of the BEV traction motor is −40 to 160 ℃, and the HEV is managed from −40 to 180 ℃. Within this environmental temperature range, the traction motor must maintain driving reliability. The reason HEV is higher than BEV is that the traction motor of HEV is mounted near the ICE, so the heat generation characteristics near the ICE must be considered. In addition, the traction motor not only has a wide operating speed range, but also needs to consider the mechanical impact caused by the motion characteristics of the vehicle. Therefore, a traction motor for a vehicle needs sufficient consideration for the following requirements.

1. Compact and Lightweight

The available space for mounting the vehicle is limited, and since an increase in weight leads to a reduction in the driving efficiency of the vehicle, it is necessary to reduce the size and weight of the electric motor.

2. Driving Reliability

It must be strong against vibrations and shocks that may occur during an accident or when driving on an irregular road surface. In addition, it is essential to secure the reliability of performance even under poor vehicle temperature conditions. In particular, in the case of PMSM, it is necessary to sufficiently examine the change in PM performance according to temperature conditions.

3. Mechanical Stability

Traction motors for vehicles have a wide operating speed range. Therefore, high-speed rotation is required due to the driving characteristics, and mechanical stability must be secured even during

high-speed rotation. This is a very important design requirement, and it is necessary to have a sufficient safety factor when designing a traction motor.

The HPMM models to be proposed in this thesis will examine their effectiveness based on the above conditions, and at the same time, the PM cost reduction effect will be mentioned.

2.3 Hybrid PM Motor Definition and Characteristics

HPMM basically belongs to the category of PMSM. That is, the structure for inserting the PM inside the rotor is the same. However, the HPMM is a topology that focuses on low cost or higher performance compared to the conventional PMSM by inserting two or more types of PM with different characteristics into the rotor. That is, by applying Nd-PM and Fe-PM at the same time, the same performance as the existing PMSM is derived and the cost is reduced [68, 69]. Alternatively, by applying Nd-PM and Alico-PM, there is a research case for the purpose of optimizing the efficiency distribution by inducing the change of the magnetic flux of Alico-PM according to the phase change of the stator magnetic field [87]. Based on the former case in this thesis, it mainly deals with PM cost reduction of vehicle traction motors by applying Nd-PM and

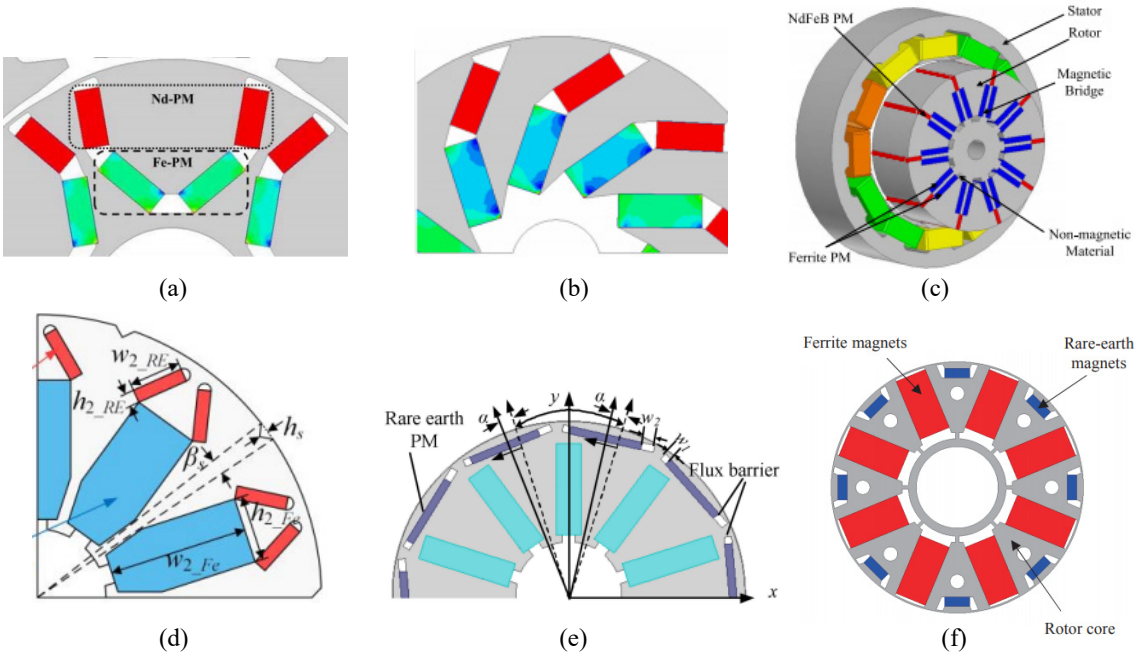

(a) (b) (c)

(d) (e) (f)

Fig. 2.5 HPMM Rotor Topology Study Case (a) [68] (b) [69] (c) [67] (d) [72] (e) [71] (f) [70]

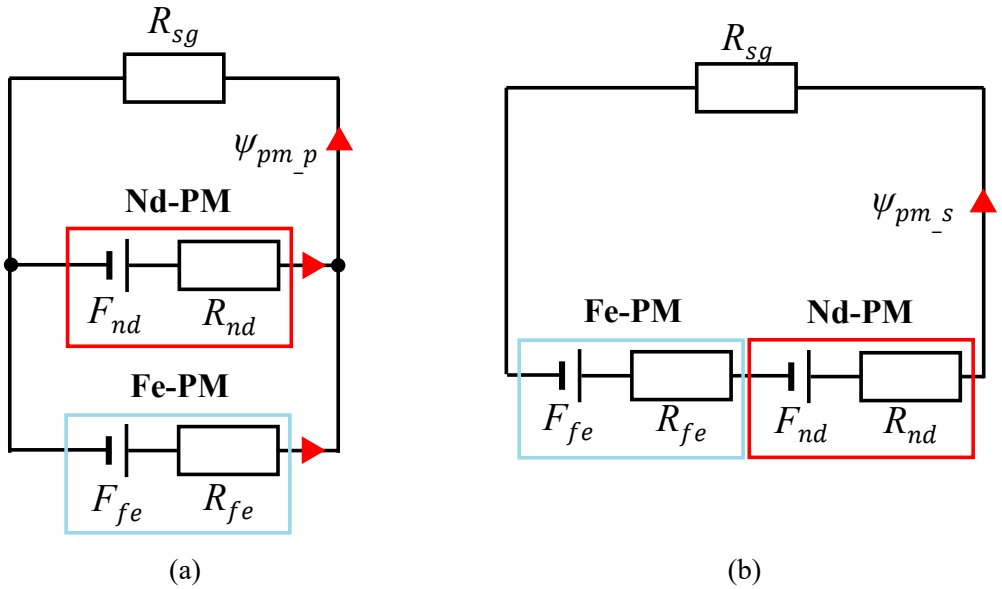

Fig. 2.6 Classification of HPMM according to *d*-axis magnetic equivalent circuit (a) parallel type (b) series type

Fe-PM at the same time.

2.3.1 Classification of Parallel and Series Type

HPMM using a mixture of Nd-PM and Fe-PM has been reported in the form of various topologies. Fig. 2.6 shows examples of HPMM presented for lower cost and higher performance compared to conventional PMSM by mixing Nd-PM and Fe-PM. Each research case shows various types of PM arrangement, but there are clearly distinguishable features. This is the case in which the magnetic flux of each PM is respectively concentrated in the *d*-axis direction and the case in which the magnetic flux of each PM is interconnected. Fig. 2.5 (a) to (d) is the former case, and (e) and (f) are the latter case. This means that it can be classified according to the *d*-axis magnetic equivalent circuit.

Fig. 2.6 is the classification according to the *d*-axis magnetic equivalent circuit of HPMM. Where, F_{nd} and F_{fe} are the magneto-motive force (MMF) of each PM, R_{nd} and R_{fe} are the reluctance of each PM, R_{sg} is the sum of the reluctance of air-gap and core, and ψ_{pm} is the PM flux linkage.

Fig. 2.6 In (a), the magnetic flux of each PM is composed of a parallel circuit, and (b) is composed of a series circuit. In a parallel circuit, the magnetic flux of each PM is concentrated in the *d*-axis direction, and high flux linkage can be obtained. Being able to obtain high flux linkage

means that the reluctance of the whole system is small. Conversely, a low reluctance may make the demagnetization durability weak against the reverse magnetic field of the stator. The series circuit has a structure in which the magnetic flux between each PM is interconnected, and has a higher reluctance compared to the parallel type. As a result, the *d*-axis PM flux is lower than that of the parallel type based on the use of the same PM. However, high reluctance is advantageous in terms of demagnetization durability, and it is possible to lower the *d*-axis inductance, which helps to improve the flux weakening control performance. These characteristics will be dealt with in Chapter 4.

In this thesis, based on the characteristics of parallel-type (P-HPMM) and series-type HPMM (S-HPMM) divided as described above, the structure and topology suitable for vehicle traction motors are proposed.

2.3.2 Comparison of Properties of Nd sintered PM and Ferrite PM applied to Hybrid PM Motor

In this thesis, HPMM for vehicle traction is proposed using Nd-PM and low-cost Fe-PM. Fe-PM is 1/10 the price of Nd-PM, and the residual magnetic flux density B_r is 1/3. The lineup of Nd-PM and Fe-PM products is shown in Fig. 2.7. In the case of the residual magnetic flux density, both PMs tend to decrease according to the α_{mag} coefficient as the temperature increases. In the case of the coercive force H_{cj}, it follows the characteristic of the β coefficient, and in Nd-PM and Fe-PM, the signs of the β coefficient are opposite to each other. Nd-PM means that the coercive force is lowered at high temperature, whereas Fe-PM means that the coercive force is lowered at low temperature. That is, the degree of coercive force with respect to the temperature of each PM acts oppositely. The *BH* characteristics and α_{mag} and β coefficients of each PM are shown in Fig. 2.8 and Table 2.2. This amount of change can be calculated as in (2.1).

$$\begin{aligned} B_r &= B_{r0}\{1+\alpha_{mag}(T_{mag}-20)\}. \\ H_{cj} &= H_{cj0}\{1+\beta(T_{mag}-20)\}. \end{aligned} \tag{2.3.2.1}$$

Here, B_{r0} and H_{cj0} are values based on room temperature, and T_{mag} is the temperature under actual operating conditions.

In the case of the environmental temperature range of the traction motor for a vehicle, the BEV is −40 to 160 ℃, and the HEV is −40 to 180 ℃. In the case of PMSM to which only Nd-PM

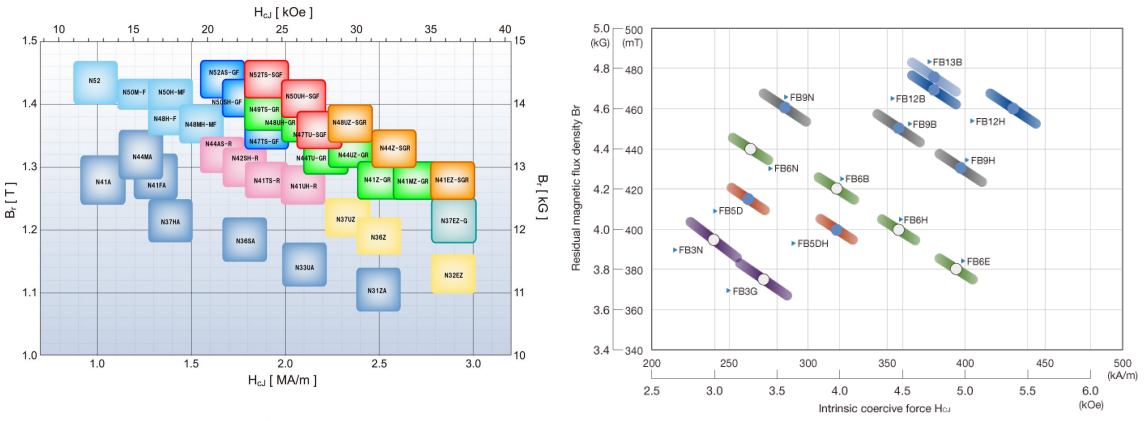

(a) (b)

Fig. 2.7 PM product line up (a) Nd-PM (Shinetsu Co.Ltd) (b) Fe-PM (TDK Co. Ltd)

Table 2.2 Temperature coefficient by each PM

Classification	Grade	α_{mag} (%/K)	β (%/K)
Nd-PM	N37UZ	−0.09	−0.46
Fe-PM	NMF-15J	−0.2	0.35

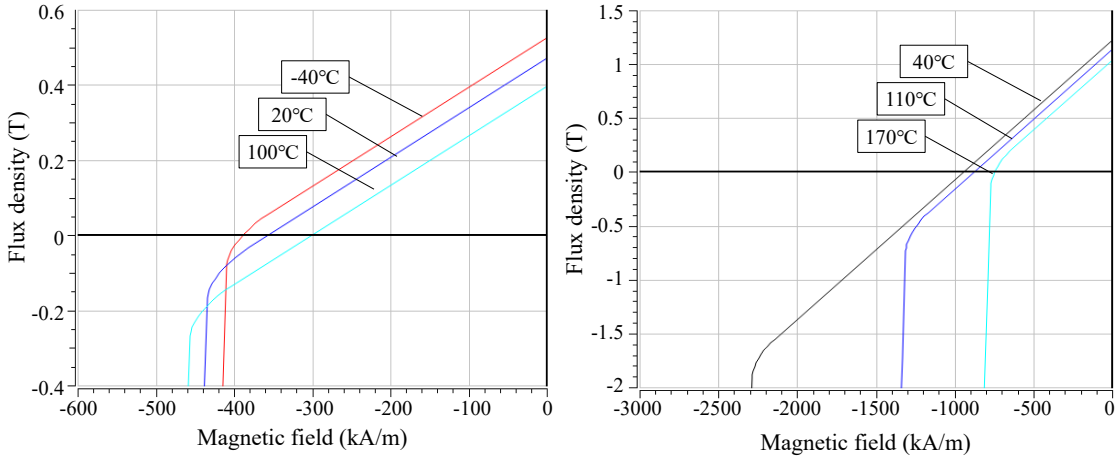

(a) (b)

Fig. 2.8 *BH* Characteristics (a) Nd-PM (Shinetsu N37UZ) (b) Fe-PM (Hitachi NMF-15J)

is applied, it is necessary to review the demagnetization durability only in the high-temperature region, but in the case of HPMM, it is necessary to review the demagnetization durability in both the low-temperature and high-temperature regions.

2.4 Main Characteristics Equations of PMSM

Except for applying a different type of PM to HPMM, its physical properties and structure belong to the category of PMSM. Therefore, in this chapter, the structure, characteristics, and main characteristic equations of PMSM will be dealt with. Fig. 2.9 and Fig. 2.10 show the rotor configuration of SPMSM and IPMSM, respectively. As can be seen in each figure, in SPMSM, a PM is attached to the rotor surface, and in IPMSM, a PM is inserted into the rotor.

Considering the magnetic flux direction by the PM, the central axis of the PM is defined as the *d*-axis, and the center between PMs separated by 90 degrees from the *d*-axis by an electric angle is defined as the *q*-axis [88].

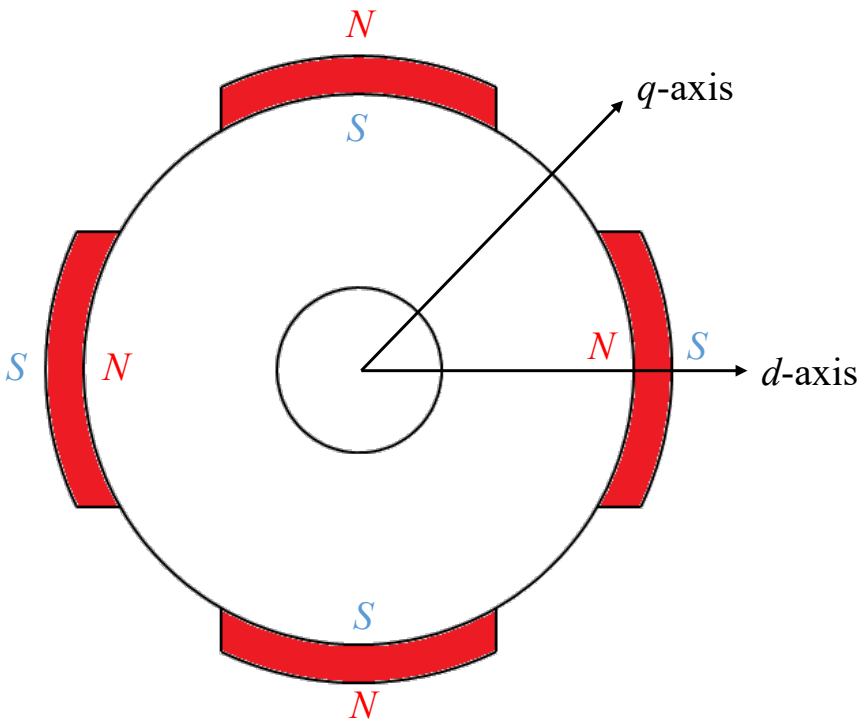

Fig. 2.9 Rotor configuration of SPMSM

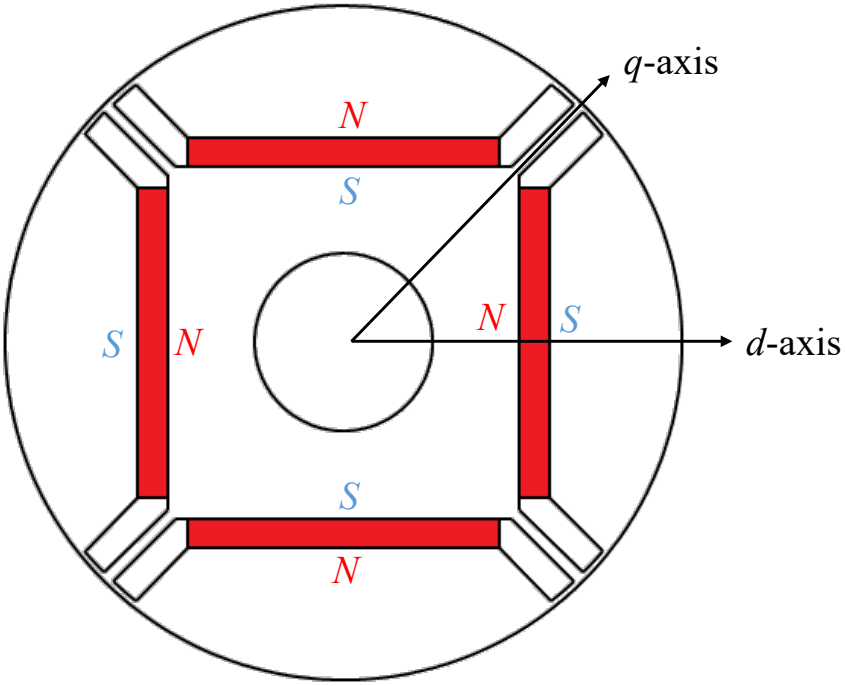

Fig. 2.10 Rotor configuration of IPMSM

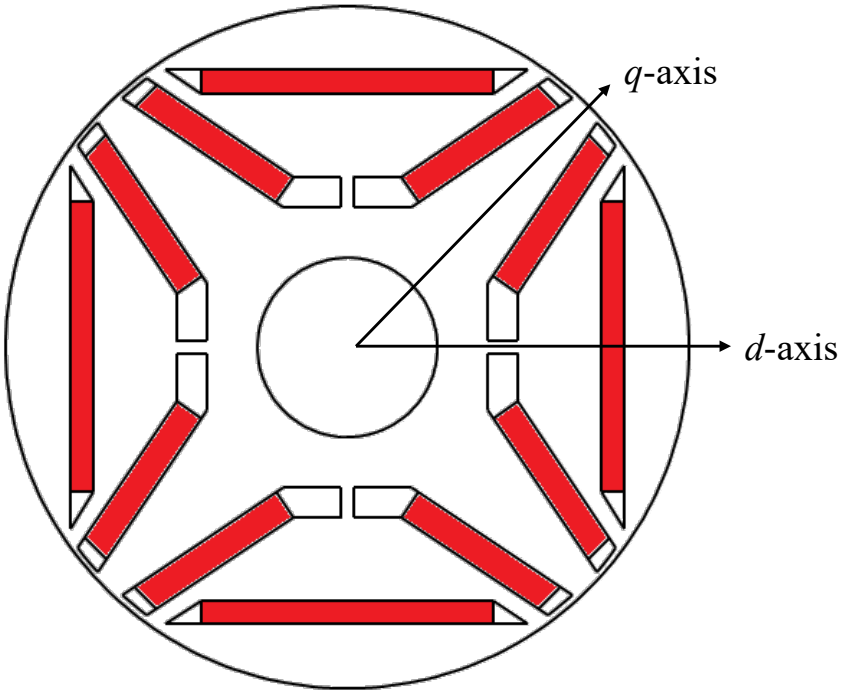

Fig. 2.11 Rotor configuration of delta type IPMSM

Considering the magnetic flux direction by the PM, the central axis of the PM is defined as the *d*-axis, and the center between PMs separated by 90 degrees from the *d*-axis by an electric angle is defined as the *q*-axis [88].

SPMSM has a PM attached to the rotor surface. Thereby, the length of the total air gap is constant regardless of the position of the rotor. Therefore, SPMSM only has an interaction between the magnetic flux of PM and the magnetic flux generated by the stator current, which means that only the PM torque of PMSM can be used. On the other hand, in IPMSM, the inductance difference occurs between the *d*-axis and the *q*-axis because the *d*-axis reluctance where the PM exists is larger than the *q*-axis reluctance. Therefore, IPMSM is advantageous for high torque density because it can use not only the PM torque but also the reluctance torque due to the difference in *d*- and *q*-axis inductance [2-4]. In addition, IPMSM does not require a non-magnetic structure (SUS, etc.) to prevent scattering of PMs at high speed, and has a large degree of freedom in the shape and arrangement of PMs [8-11]. It has the advantage that the possibility of demagnetization is small because it is not directly exposed to the heat and armature reaction generated by the stator windings.

The delta type IPMSM in Fig. 2.11 has a multi-layer structure of straight PMs on the rotor surface and V-shape inside the rotor, and the arrangement of the PMs is similar to the delta shape. Since the delta type IPMSM also inserts a PM in multiple layers, it is possible to increase the magnitude of the reluctance torque like the conventional IPMSM. This multi-layered structure can generate a larger reluctance torque because various design variables such as the position of PMs in each layer and the angle between PMs can be considered. That is, it is advantageous to improve the reluctance torque compared to the IPMSM inserted as a single layer. Therefore, most rotor topologies of traction motors for vehicles require high torque density, and wide variable speed operation using reluctance torque is also required, so a multi-layer structure is mostly adopted.

As explained in the previous section, since most of the physical properties of HPMM are identical to those of IPMSM except for applying different types of PMs, the mathematical model of IPMSM can be applied as it is. The output of the motor is limited by the maximum current I_{max} determined by the current rating of the inverter and the thermal rating of the motor, and the maximum output voltage V_{max} determined by the PWM method of the inverter and the maximum

DC link voltage that the inverter can supply. These voltage and current limits are expressed as:

$$V_{ds}^2+V_{qs}^2 \leq V_{max}^2 \tag{2.4.1}$$

$$i_{ds}^2+i_{qs}^2 \leq i_{max}^2 \tag{2.4.2}$$

Here, i_{ds} and i_{qs} are the dq-axis currents, and V_{ds} and V_{qs} are the d- and q-axis terminal voltages.

If the voltage equation of IPMSM is converted into a synchronous frame with a rotor rotating at synchronous speed as the reference coordinate, it is as follows.

$$V_{ds}^2=R_s i_{ds}+\frac{d\lambda_{ds}}{dt}-\omega_r\lambda_{qs} \tag{2.4.3}$$

$$V_{qs}^2=R_s i_{qs}+\frac{d\lambda_{qs}}{dt}+\omega_r\lambda_{ds} \tag{2.4.4}$$

where ω_r is the synchronous electrical angular velocity, V_{ds} and V_{qs} are the d- and q-axis terminal voltages, i_{ds} and i_{qs} are the d- and q- axis stator currents, R_s is the stator phase resistance, and λ_{ds} and λ_{qs} are the d- and q-axis stator flux linkages.

In addition, the d, q-axis stator flux linkage is expressed as follows.

$$\lambda_{ds} = L_{ds} i_{ds} + \lambda_f \ , \quad \lambda_{qs} = L_{qs} i_{qs} \tag{2.4.5}$$

Here, L_{ds} and L_{qs} are the d-axis inductances, and λ_f is the flux linkage by the PM.

Therefore, by (2.2.3), (2.2.4) and (2.2.5), the voltage equation of IPMSM is expressed as follows.

$$V_{ds}=R_s i_{ds}+L_{ds}\frac{di_{ds}}{dt}-\omega_r L_{qs} i_{qs} \tag{2.4.6}$$

$$V_{qs}=R_s i_{qs}+L_{qs}\frac{di_{qs}}{dt}+\omega_r(L_{ds} i_{ds}+\lambda_f) \tag{2.4.7}$$

Here, ignoring the voltage component proportional to the current differential that occurs when the *d*- and *q*-axis currents change rapidly, it can be expressed as follows.

$$V_{ds}=R_s i_{ds} - \omega_r L_{qs} i_{qs} \tag{2.4.8}$$

$$V_{qs}=R_s i_{qs}+\omega_r (L_{ds} i_{ds} + \lambda_f) \tag{2.4.9}$$

As shown in the above equation, assuming that the voltage drop due to the stator phase resistance is not large, the terminal voltage of the motor is proportional to ω_r.

The electrical input of IPMSM is as follows.

$$P_{in}=\frac{3}{2}(V_{ds} i_{ds} + V_{qs} i_{qs}) \tag{2.4.10}$$

The voltage components of (2.4.10) are expressed as (2.4.3) and (2.4.4) as follows.

$$P_{in}=\frac{3}{2}\left\{R_s\left(i_{ds}^2+i_{qs}^2\right)+\frac{d}{dt}(\lambda_{ds} i_{ds}+\lambda_{qs} i_{qs})+\omega_r(\lambda_{ds} i_{qs} - \lambda_{qs} i_{ds})\right\} \tag{2.4.11}$$

Electrical input P_{in} consists of the first term, copper loss, the second term, the rate of change of magnetic energy with respect to time, and the last term, mechanical output. Therefore, the mechanical output P_m is as follows.

$$P_m=\frac{3}{2}\omega_r(\lambda_{ds} i_{qs} - \lambda_{qs} i_{ds}) \tag{2.4.12}$$

The generated torque T_e is as follows when (2.4.5) is applied.

$$T_e=\frac{P_m}{\left(\frac{\omega_r}{P/2}\right)}=\frac{3}{2}\frac{P}{2}\left(\lambda_{ds} i_{qs} - \lambda_{qs} i_{ds}\right)=\frac{3}{2}\frac{P}{2}\left\{\lambda_f i_{qs} + \left(L_{ds} - L_{qs}\right) i_{ds} i_{qs}\right\} \tag{2.4.13}$$

The first term is the PM torque generated by the interaction between the magnetic flux by the PM and the stator *q*-axis current, which is the same as the principle of torque generation in SPMSM. The second term is the magnetoresistance torque generated due to the difference in inductance of the *d*- and *q*-axes, that is, the saliency. In the case of IPMSM, since the *d*-axis inductance is smaller than the *q*-axis inductance (L_{ds}<L_{qs}), the *d*-axis current must be less than 0 to act as the sum of the reluctance torque and the PM torque.

Based on the characteristic equation and physical characteristics of IPMSM, the characteristics of non-rare earth motors are compared as follows. A typical non-rare earth motor is a synchronous reluctance motor (SynRM). SynRM generates *torque b*y using the change in reluctance as the rotor of the salient pole structure rotates. Since SynRM has no PM, there is no magnetic flux linkage λ_f in the voltage equations (2.4.8) and (2.4.9) of IPMSM. Therefore, for the voltage equation of SynRM, V_{ds} is equal to (2.4.8), and V_{qs} is equal to:

$$V_{qs}=R_s i_{qs}+\omega_r L_{ds} i_{ds} \tag{2.4.14}$$

In addition, the mechanical output of SynRM is as follows.

$$P_m=\frac{3}{2}\frac{P}{2}\omega_r\left(L_{ds}-L_{qs}\right)i_{ds}i_{qs} \tag{2.4.13}$$

Under voltage limit V_{max} and current limit I_{max}, (2.4.1), (2.4.2), (2.4.8), (2.4.9), and (2.4.14) are plotted on the i_d-i_q plane, Fig. 2.12 can be expressed as.

Here, the reactive powers Q_{ipm} and Q_{syn} of IPMSM and SynRM are respectively as follows.

$$Q_{ipm}=\frac{3}{2}\frac{P}{2}\omega_r\left(L_{ds}i_{ds}^2+L_{qs}i_{qs}^2+\lambda_f i_{ds}\right) \tag{2.4.14}$$

$$Q_{syn}=\frac{3}{2}\frac{P}{2}\omega_r\left(L_{ds}i_{ds}^2+L_{qs}i_{qs}^2\right) \tag{2.4.15}$$

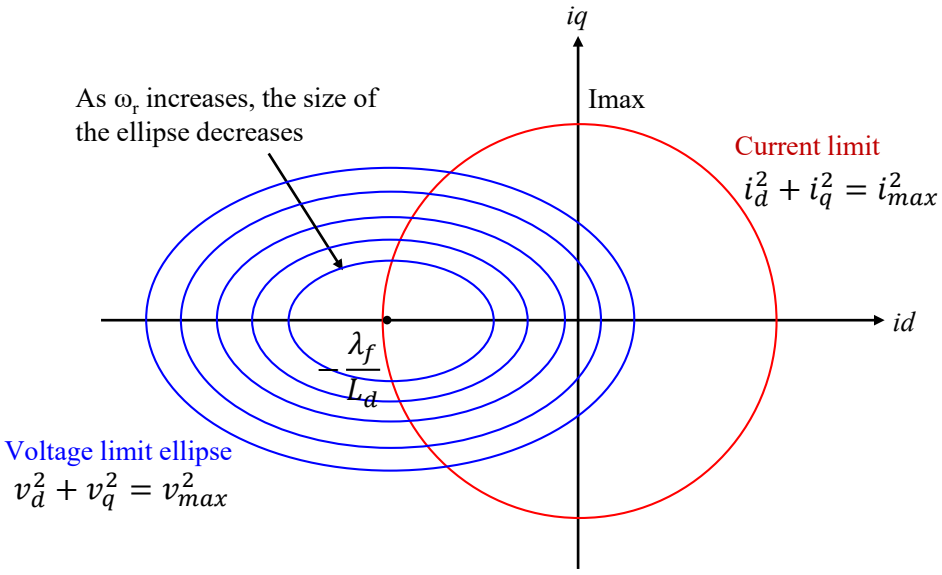

(a)

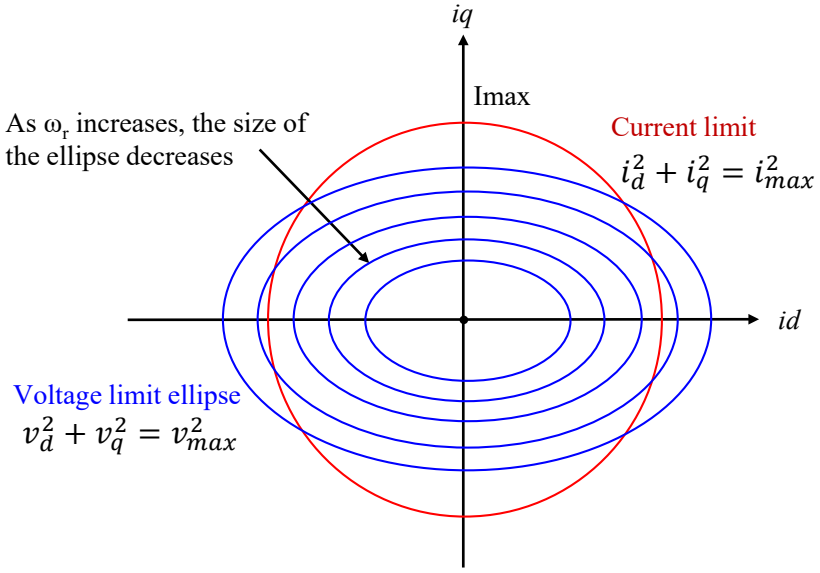

(b)

Fig. 2.12 Voltage and current limit on i_d-i_q plane (a) IPMSM (b) SynRM

Compared to IPMSM, SynRM has the advantage of being able to obtain a high saliency ratio according to manufacturability. In addition, since it does not use a PM, it is not necessary to consider the demagnetization problem, and it is possible to implement a low cost.

However, as in (2.4.14) and (2.4.15), IPMSM increases the i_{ds} in the negative direction in the high-speed operation region, thereby reducing the reactive power Q_{ipm}, so the power factor is good even in the high-speed operation region. However, since SynRM has no way to reduce reactive power Q_{syn}, the power factor characteristic is deteriorated. In other words, to drive a motor of the same output, SynRM requires a larger inverter capacity compared to IPMSM. Also, as shown in Fig. 2.12, the operating point of the motor operates at the intersection of the voltage limiting ellipse and the current limiting circle. As the speed ω_r increases, the voltage limit ellipse decreases. Since the center of the voltage limit ellipse is located at the origin on the i_d-i_q plane, SynRM operates in the flux weakening control region where i_{ds} and i_{qs} decrease simultaneously over a certain speed region. That is, the trajectory of the input current tends to decrease as the speed increases. If the voltage is constant but the input current decreases, it means that the electrical input energy must decrease as the speed increases, and at the same time, the mechanical output also decreases. On the other hand, since the voltage limiting source of IPMSM exists on the -i_d axis, the point is determined by -(λ_f/L_d) according to the mathematical derivation of the voltage equation. IPMSM can apply maximum input current up to a specific speed range, and it appears as a high mechanical output compared to SynRM. That is, as a traction motor for a vehicle having a wide driving range, it is superior in IPMSM torque, power density, and flux weakening controllability compared to SynRM.

Comparing other non-rare earth motors and IPMSMs based on this logic is as follows. First, like SynRM, IM does not have magnetic flux due to PMs. However, an additional current must be applied to the stator side to induce magnetic flux in the rotor. It is called excitation current. Since the existing stator current and the excitation current are combined and more current is applied to drive the motor, the coil cross-sectional area must be increased for cooling the motor. This appears as an increase in the stator size. In addition, IM always causes rotor copper loss due to the slip phenomenon in the rotor, which results in reduced efficiency.

Ferrite motors have magnetic flux due to PMs in the rotor. However, since the residual magnetic flux density of Fe-PM is 1/3 of that of Nd-PM, the output lowering characteristic appears

compared to the conventional IPMSM. In addition, since Fe-PM has a characteristic of easily losing magnetic flux at a low temperature, it is difficult to meet the demagnetization durability required in a traction motor for a vehicle.

The field winding type motor can generate magnetic flux in the rotor through an external power source. However, since a mechanical contact device called a brush is required between the external power source and the rotor, it is disadvantageous in terms of durability. In addition, it is necessary to take measures against damage to the coil wound on the rotor during high-speed rotation.

In summary, IPMSM, which has high starting torque and excellent efficiency and output characteristics, is advantageous as a vehicle traction motor compared to other motors. In particular, the reluctance torque can be maximized, and it has superior torque output characteristics compared to other PM motors in the full operation speed range. Therefore, in order to solve the risk of Nd-PM in the future, HPMM based on IPMSM and minimizing Nd-PM usage can be a realistic alternative to non-rare earth motors.

Chapter 3. BEV Traction Hybrid PM Motor with improved reluctance torque

In this chapter, in order to reduce the amount of Nd-PM used in traction motors for electric vehicles, a novel HPMM that simultaneously applies Fe-PM is proposed. Conventional HPMM can be divided into P-HPMM and S-HPMM. P-HPMM is advantageous for PM torque improvement because it can obtain high PM flux linkage, but there is a problem in that Fe-PM is demagnetized due to the strong magnetic flux of Nd-PM. S-HPMM is the way to fundamentally solve these problems. However, it is difficult to improve PM flux linkage compared to P-HPMM. Therefore, in this chapter, a novel rotor topology that can effectively generate reluctance torque by improving S-HPMM is proposed. The target motor is the 2018 NISSAN LEAF traction motor. The proposed motor has the same torque density as the target motor, while reducing Nd-PM usage by 38%.

3.1 Nissan Leaf EV Traction Motor Benchmark Study as Target Motor

The target motor is the traction motor of NISSAN LEAFTM EV commercialized in 2018. Our research team purchased an actual vehicle, disassembled and analyzed the specifications of the powertrain module. Fig. 3.1 shows the 2018 Nissan LEAF vehicle and powertrain module, and Table 3.1 is the vehicle specification.

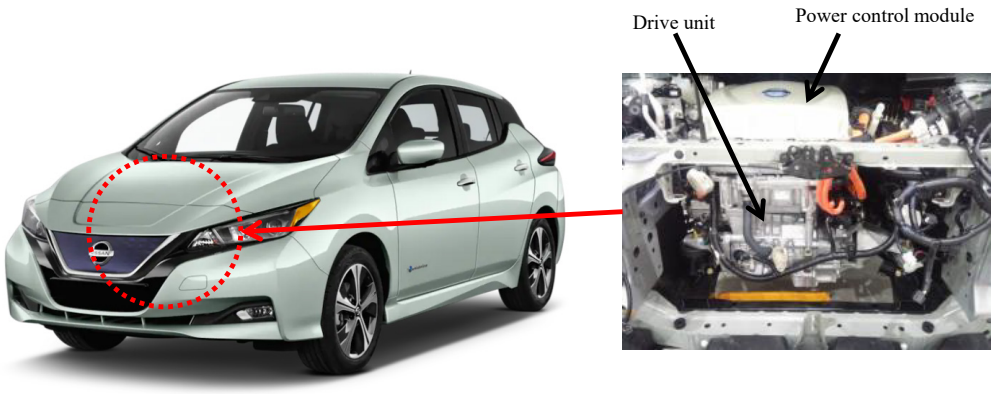

Fig. 3.1 Nissan LEAF powertrain

Table. 3.1 Specifications of Nissan Leaf EV

Power	110kW
Axle ratio	8.1938
Battery capacity	40kWh
0-100kph	7.9s
Driving range	243km
Top speed	144kph

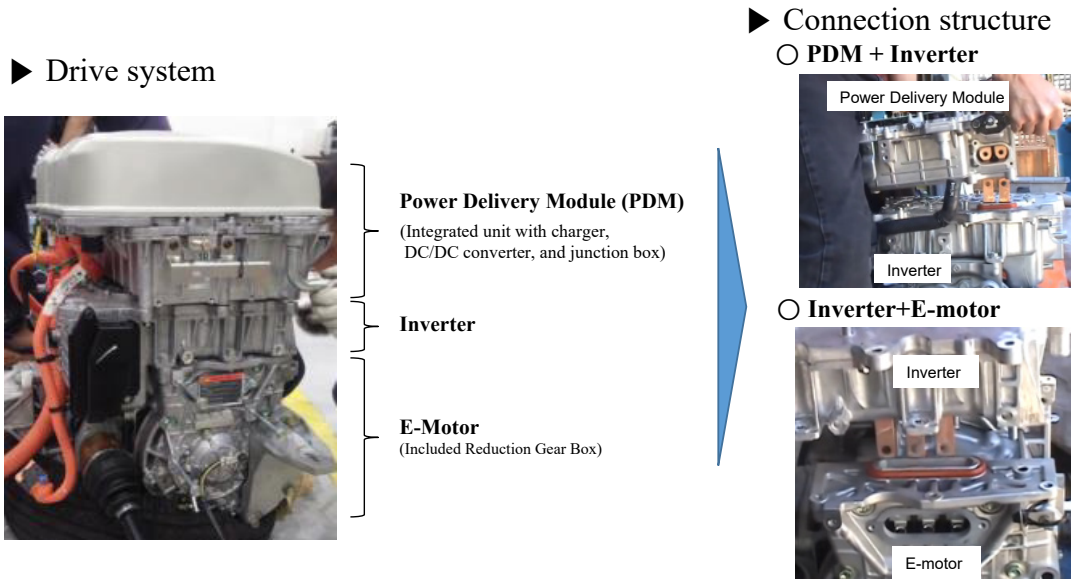

Fig. 3.2 Drive system of Nissan LEAF

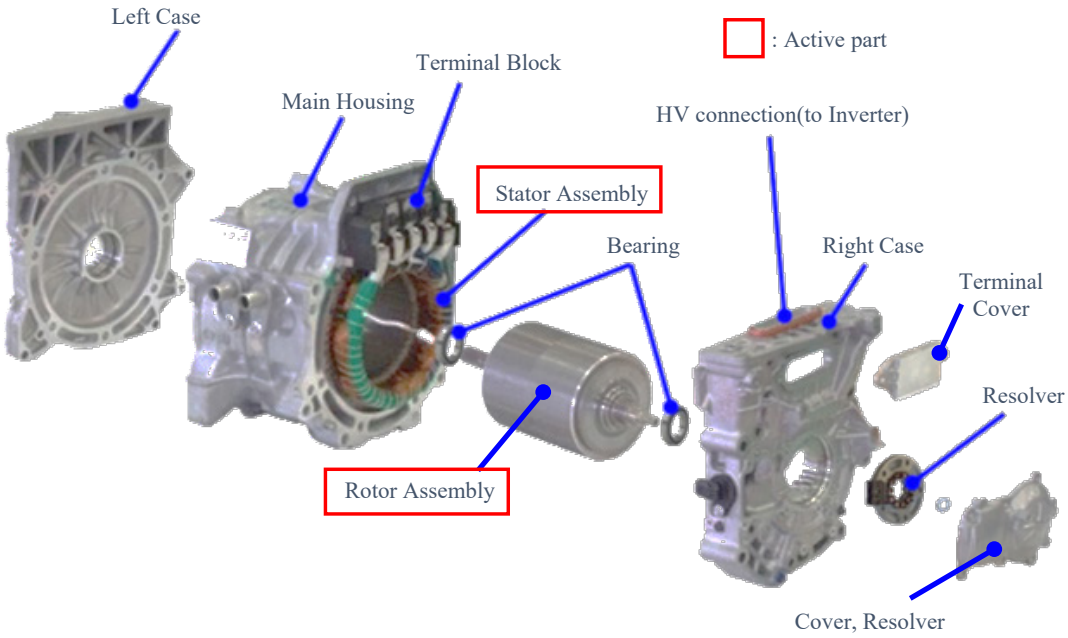

Fig. 3.3 Exploded view of target motor

Fig. 3.2 shows the drive system of the Nissan LEAF. The drive system has an integrated structure in which the inverter, DC/DC converter, charger, and traction motor are vertically assembled as shown in Fig. 3.2. Therefore, it is judged that the space and weight are remarkably reduced. In addition, it is connected in a cable-less manner between the power delivery module (PDM) and the inverter, and the motor and inverter are the same. Power loss can be reduced due to cable-less method, and it is possible to reduce cost at the same time. However, it is disadvantageous compared to the cable connection method in terms of assembly manufacturability and tolerance management.

3.1.1 Motor Disassembly Results and Main Specifications

Fig. 3.3 is the exploded view of e-motor. The e-motor can be divided into a passive part and an active part. Passive parts include housing and case, cooling channels, bearings and resolvers, and active parts include stator assembly and rotor assembly. The main roles of the passive part are cooling, connection with the inverter, and position sensing, and the active part is a part that

generates mechanical output based on electromagnetic phenomena. In this paper, the main benchmarking and analysis target the active part.

Fig. 3.4 shows the stator assembly and the cut in the outer diameter direction. The specifications of the coil and winding are as follows. The number of stranded wires per slot is 108. Since 12 stranded wires make up 1 turn, the number of turns per slot is 9 turns. The diameter per wire is 1.2mm including coating, and the winding method is the distributed winding. The end turn height is 30mm and 40mm, respectively. The specifications of the stator core are as follows. The outer diameter is 200mm and the inner diameter is 131mm. The lamination is 140mm, and the thickness of the core sheet is 0.3mm. The total weight of this stator assembly is 19kg, and the overall specifications are shown in Table 3.2. In addition, the 2D modeling of the stator core for electromagnetic field analysis is shown in Fig 3.5.

Fig. 3.6 shows the rotor assembly and the incision in the outer diameter direction. The rotor assembly reflects a two-stage linear skew of approximately 3.75 degrees. The lamination of the rotor core is 140 mm, the outer diameter is 130 mm, the inner diameter is 45 mm. The thickness of the core sheet is 0.3t, the same as the stator. The topology of the rotor is an 8-pole delta type structure. A bar-type PM is inserted at the front end and a V-type PM is inserted inside the rotor core. The size of the bar type PM is 4mm thick, 28mm wide, and 25mm high. The size of the PM inserted in the V-type is 2.5mm thick, 22mm wide, and 25mm high.

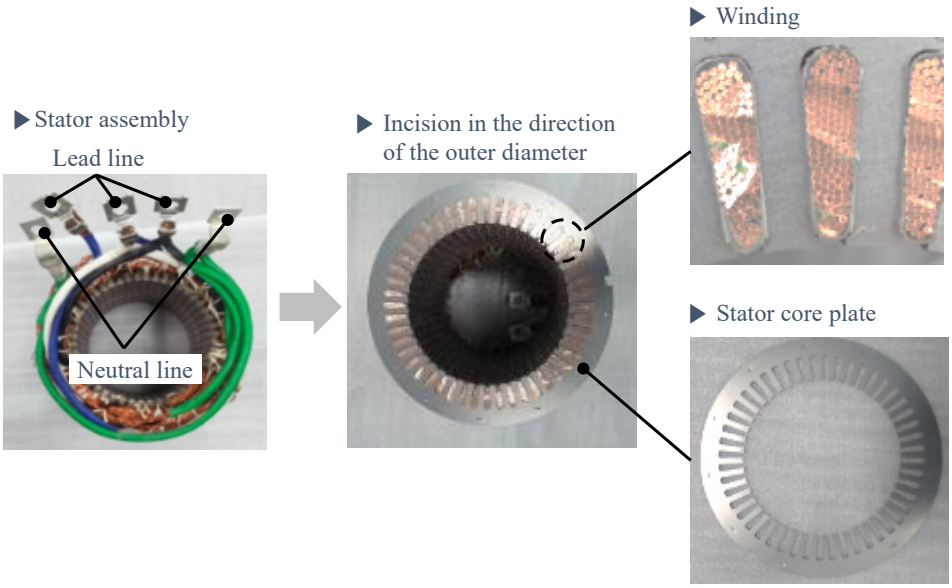

Fig. 3.4 Stator assembly of target motor

Table. 3.2 Specifications of the stator assembly of the target motor

Outer diameter	200 mm
Inner diameter	131 mm
Stack length	140 mm
End-turn length (lead side/opposite side)	40 / 30 mm
Winding type	Distributed
Thickness of core plate	0.3 t
Diameter of stranded wire	1.2 mm
No. of slot	48
No. of turns per slot	9 turns
Series turns	12 turns
Weight	19 kg

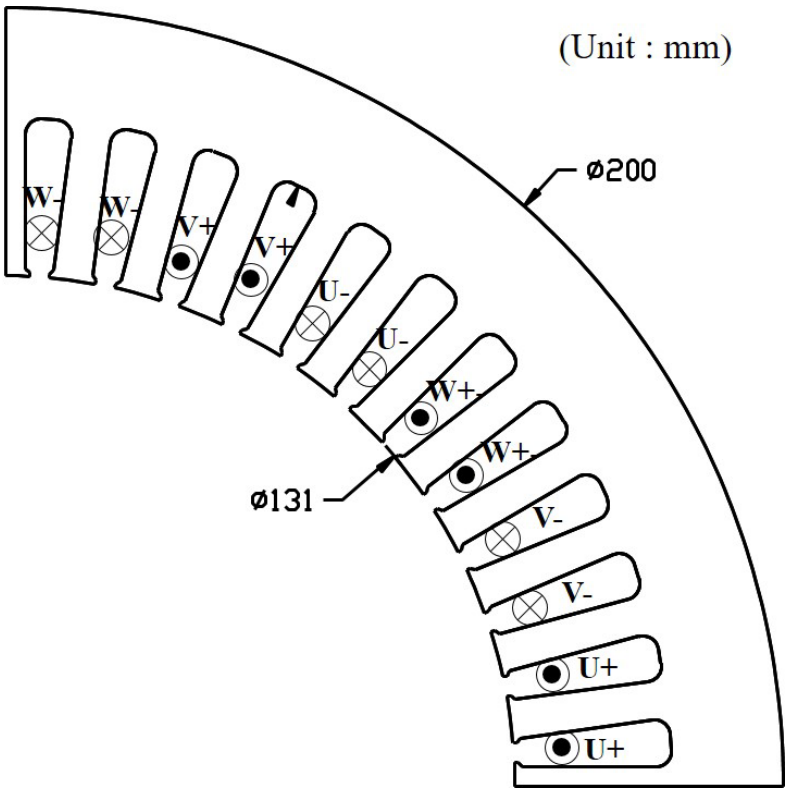

Fig. 3.5 2D model of stator core of target motor

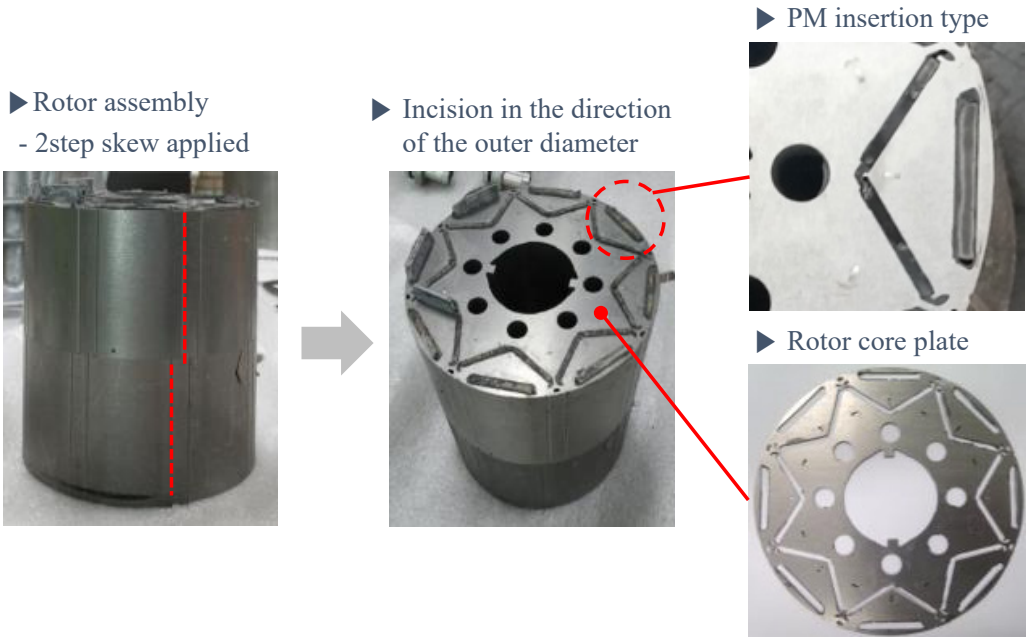

Fig. 3.6 Roator assembly of target motor

Table. 3.2 Specifications of the rotor assembly of the target motor

Outer diameter	130 mm
Inner diameter	45 mm
Stack length	140 mm
No. of poles	8
Skew	2-step, 3.75°
Thickness of core plate	0.3 t
PM size (Bar type)	T4×W28×L25
PM size (V type)	T2.5×W22×L25
Stacking method	Inter-lock
PM weight	1.88kg
Total weight	19 kg

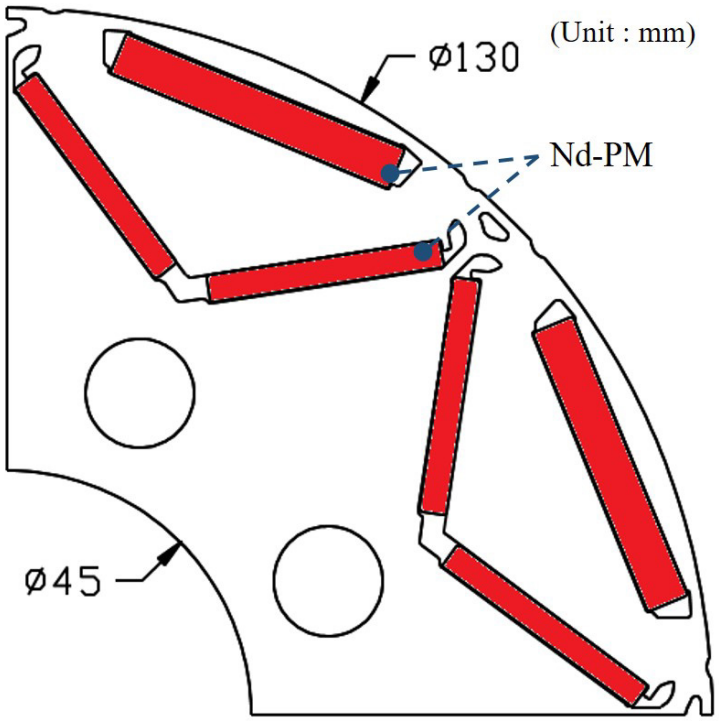

Fig. 3.7 2D model of rotor core of target motor (Unit : mm)

The total weight is 19 kg, and the PM weight is 1.88 kg. The overall specifications are shown in Table 3.3, and the 2D model of the rotor core is shown in Fig. 3.7.

3.1.2 Comparison between Back-EMF Measurements and 2D model FEA Results to improve Analysis Accuracy

After assembling the stator assembly and rotor assembly of the target motor by manufacturing a simple housing for measuring Back-EMF, the test equipment was configured as shown in Fig. 3.8(a). Fig. 3.8(b) shows the back EMF measurement result at 1,000 rpm. The measured back EMF value is 39.2 Vrms.

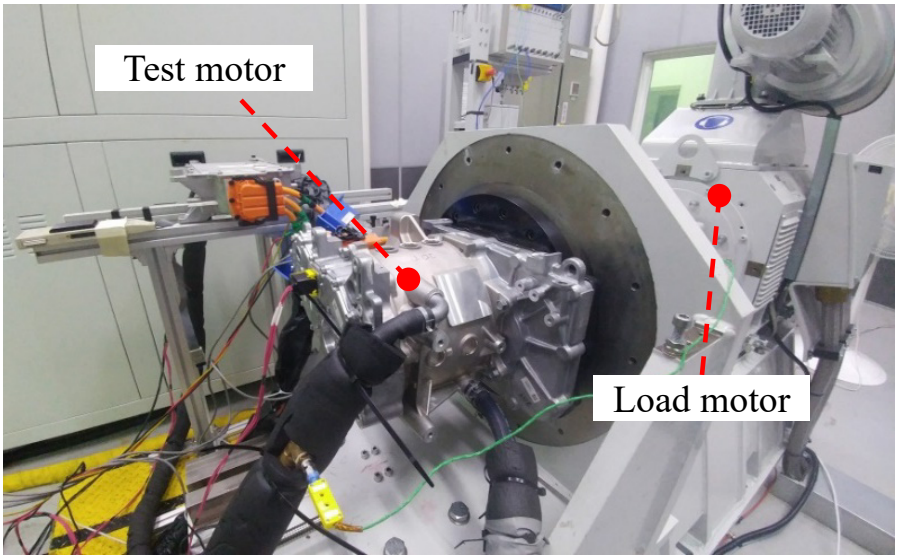

(a)

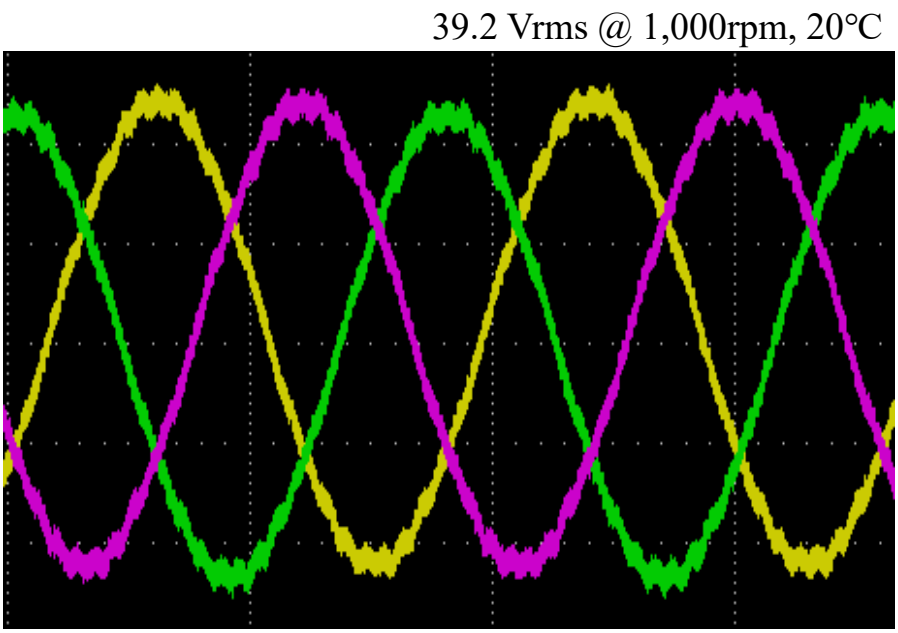

(b)

Fig. 3.8 Back-EMF measurement (a) test facility (b) measurement results

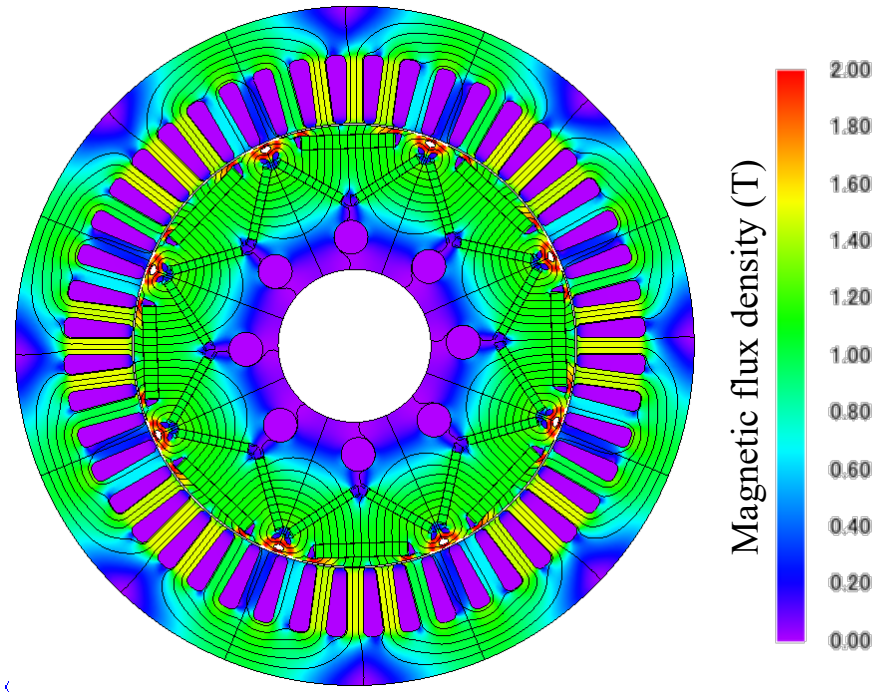

(a)

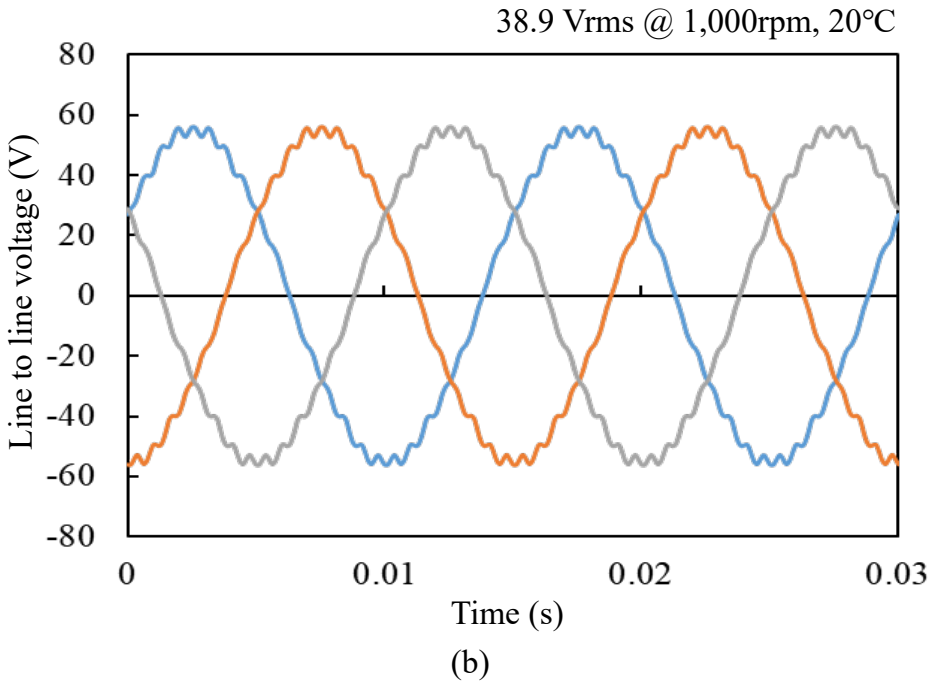

(b)

Fig. 3.9 No-load analysis results (a) flux density distribution (b) Back-EMF

Fig. 3.9 (a) is the flux density distribution at no load of the 2D model of Fig. 3.5 and Fig. 3.7. At this time, the grade of PM was N37UZ (Shinetsu Co. Ltd.), and 27PNX1350F (posco Co. Ltd.) was applied for the electrical steel sheet. Fig. 3.8 (b) is the back-EMF waveform. In order to be similar to the actual measurement result of Fig. 3.8 (b), the stacking factor was partially adjusted in the 2D analysis model. The back electromotive force analysis result is 38.9Vrms at 1,000rpm. The error rate compared to the measured value of 39.2Vrms is 0.7%.

Under the same analysis conditions, the maximum torque is 334.1 Nm at PM temperature of 100 ℃ and an input current of 456 Arms. Fig. 3.10 shows the torque waveform at the maximum torque point. This result is 4.2 % higher than the official catalog value of 320 Nm [89]. Therefore, in this thesis, 334.1 Nm is set as the target torque. Table 3.3 shows the comparison results for back-EMF and peak torque. The HPMM models to be presented in the next chapter were also reviewed under the same analysis conditions as the target motor.

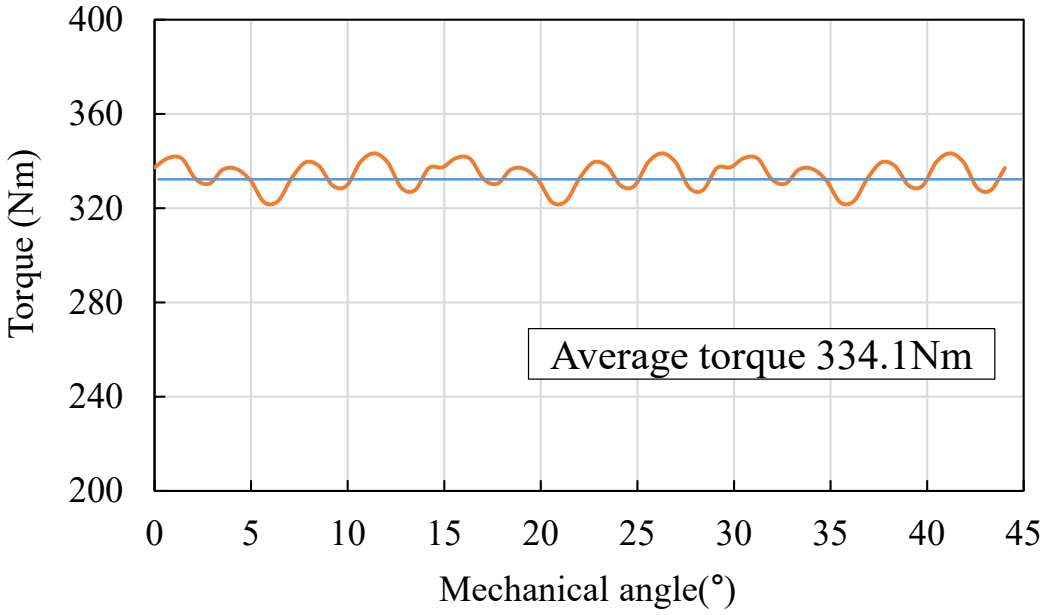

Fig. 3.10 Torque analysis results of target motor (Input current 456Arms, PM temperature 100℃, Control angle 45°)

Table. 3.3 Comparisons of Back-EMF and peak torque

Classification	Back-EMF @1,000rpm	Peak torque
2D-FEA result	39.2 Vrms	334.1Nm (target torque)
Measurement and Catalog value	38.9 Vrms	320 Nm
Error ratio	0.7 %	4.2 %

3.2 Conventional Parallel Type Hybrid PM Motor Performance Characteristics and Problems

This chapter explains the design variables, performance characteristics, PM cost, flux density distribution and problems of the conventional P-HPMM under the same stator as the target motor, and suggests alternatives to improve them.

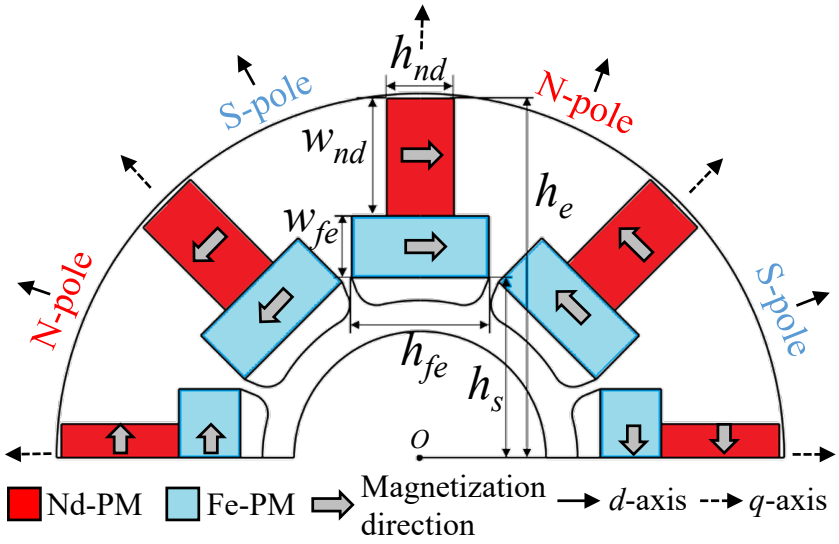

Fig. 3.11 Basic structure and design variable of conventional P-HPMM

3.2.1 Define Design Variables

Fig. 3.11 shows the basic structure, design variables of the conventional P-HPMM. As shown in Fig. 3.11. the structure of arranging each PM on the q-axis is pro-posed in [71], and although there is a difference in the number of divided PM, the magnetic equivalent circuit is the same as in Fig. 2.6(a). Since such a parallel configuration concentrate the magnetic flux of each PM in the *d*-axis direction, there is an advantage of improving the PM torque of the IPMSM.

In Fig. 4(a), h_s and h_e are the starting and ending points where PMs are placed. h_{nd} and h_{fe} are the thicknesses of Nd-PM and Fe-PM, respectively, and w_{nd} and w_{fe} are the widths of each PM. The structure of the stator is the same as that of the target motor, and NMF-15J (Hitachi metals Co., Ltd.) are applied to Fe-PM. The maximum average torque for each design variable was reviewed as follows.

First, h_s and h_e are fixed at 32.1 mm and 64.1 mm, respectively, and w_{fe} is also fixed at 24.6 mm. The width ratio k_w and thickness ratio k_h of each PM is defined as follows.

$$k_w=\frac{w_{nd}}{w_{fe}}, \quad k_h=\frac{h_{nd}}{h_{fe}} \tag{3.2.1.1}$$

Table 2 shows the design variable range for each PM dimension. where k_w ranges from 0.24 to 0.49 and k_h ranges from 1.67 to 2.56. Also, the total PM cost C_t is calculated as:

$$C_t = v_{nd}\rho_{nd}a_{nd}+v_{fe}\rho_{fe}a_{fe} \tag{3.2.1.2}$$

Where v_{nd} and v_{fe} are the Nd-PM and Fe-PM volumes, ρ_{nd} and ρ_{fe} are the density of each PM (Nd-PM: 7,620 kg/m^3, Fe-PM: 5,100 kg/m^3), and a_{nd} and a_{fe} are the price per weight of each PM ($/kg). In this thesis, the price of Nd-PM was selected to be 10 times that of Fe-PM, which means $a_{nd}=10a_{fe}$.

3.2.2 Review of Distribution of Maximum Average Torque and PM cost

Fig. 3.12 shows the maximum average torque distribution for k_w and k_h of the conventional P-HPMM. As shown in Fig. 3.12, as k_w and k_h increase, the maximum average torque also tends to

Table. 3.3 Range of P-HPMM design variables

Design variables	Unit	Min.	Max.
W_{nd}	mm	14	23
W_{fe}	mm	9	17
h_{nd}	mm	6	12
h_{fe}	mm	24.6(Constant)	
k_w	-	1.67	2.56
k_h	-	0.24	0.49

increase. This means that as the amount of Nd-PM used increases, the maximum average torque also increases. In addition, the gray plane means the target torque, and the upper region of the corresponding plane is a region that satisfies the target torque, and the lower region is a region that does not meet the target torque.

Here, the intersection line between the target torque plane and the maximum average torque plane is indicated by a dashed line on the PM cost distribution for k_w and k_h in Fig. 3.13.

In Fig. 3.13, PM cost is normalized based on the total PM cost of the target motor, and the minimum PM cost point on the dash line is (k_w, k_h)=(2.38, 0.41), where PM cost is 1.09 p.u.. In other words, compared to the target motor, the PM cost of the conventional P-HPMM structure is 9 % higher, and the cost reduction effect as an HPMM did not appear.

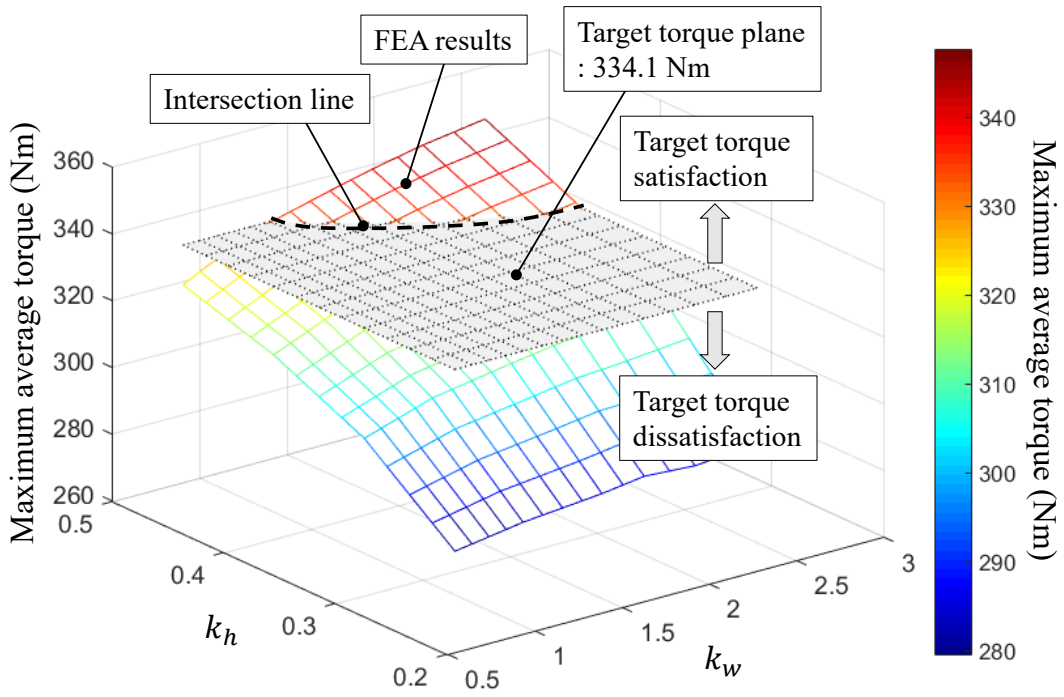

Fig. 3.12 Maximum average torque distribution for k_h, k_w of the conventional P-HP MM

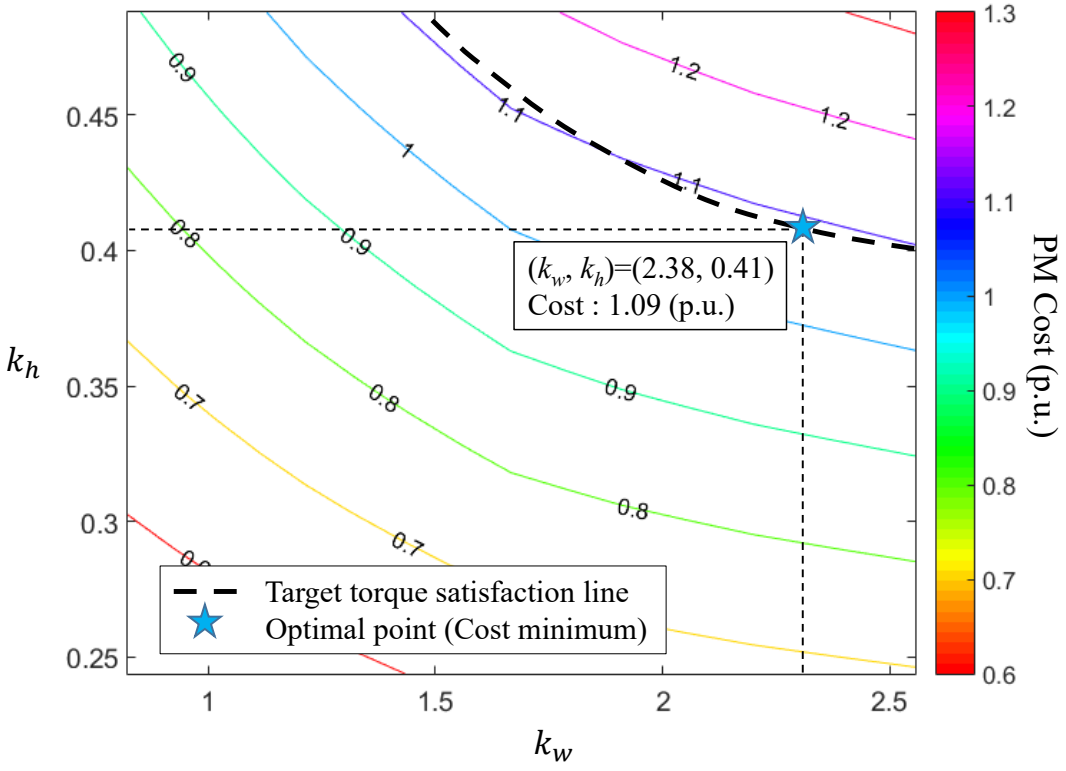

Fig. 3.13 PM cost distribution for k_w and k_h of the conventional P-HPMM.

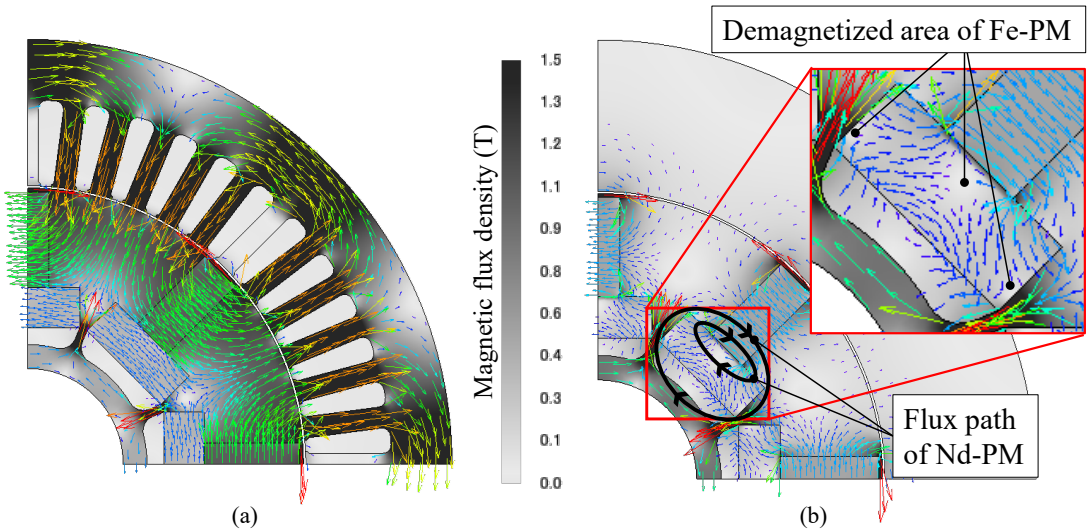

Fig. 3.14 Flux density distribution of the conventional P-HPMM. (a) with stator (b) without stator

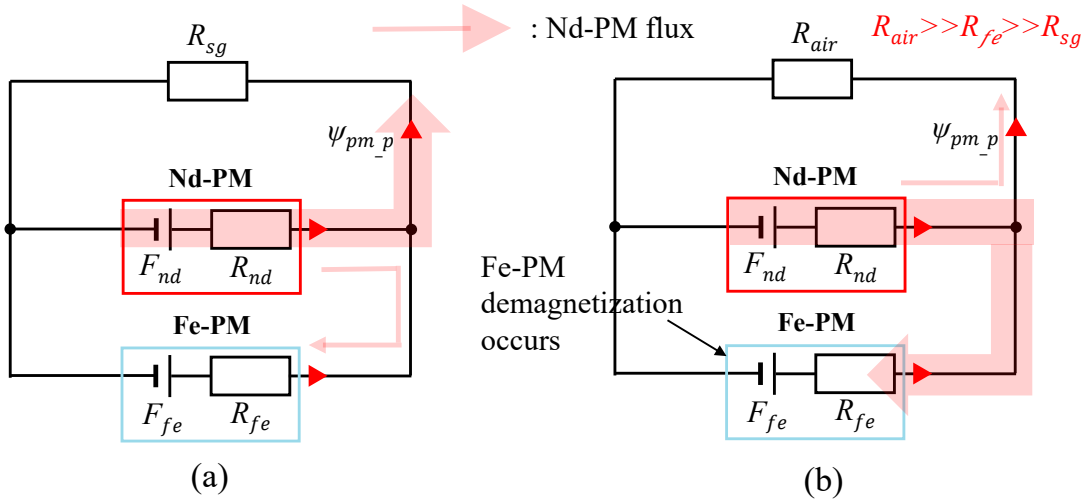

Fig. 3.15 Change of Nd-PM flux (a) with stator (b) without stator

3.2.2 Problems Considering Motor Manufacturing Process

Fig. 3.14 shows the no-load magnetic flux density distribution according to the presence or absence of a stator in the conventional P-HPMM at minimum cost point. As shown in Fig. 3.14(a), in the presence of a stator, the magnetic flux of each PM is concentrated in the d-axis to generate PM flux linkage though the stator. However, as shown in Fig. 3.14(b), in the absence of a stator, the magnetic flux at the lower end of Nd-PM penetrates Fe-PM, causing demagnetization of Fe-PM. The reason for this is because of the parallel configuration in Fig. 2.6(a). When the stator does not exist, R_{sg} is changed to air with high reluctance. As a result, the magnetic flux of Nd-PM passes through Fe-PM, which has a relatively small reluctance, and converges. On the side of Fe-PM with low coercive force, the magnetic flux of Nd-PM acts as a strong reverse magnetic field, resulting in local demagnetization.

This characteristic can be expressed as the amount of change in the main magnetic flux of Nd-PM on the *d*-axis magnetic equivalent circuit depending on the presence or absence of a stator, as shown in Figure 3.15. HPMM with such parallel structure characteristics inevitably causes demagnetization by Nd-PM.

Fig. 16 shows the mass production process of the traction motor. When assembling a rotor, in general, a non-magnetized PM is inserted into the rotor core through an automated facility, and then the entire magnetization is performed through a magnetizing yoke. As a result, productivity can be improved by reducing production time and minimizing manufacturing errors.

However, before assembly with the stator and housing, the magnetized rotor is in a stand-alone state. Considering this manufacturing process, it is difficult to apply P-HPMM to a traction motors in practice.

In order to solve the fundamental problem of the parallel type, a structure in which the magnetic fluxes of each PM link with each other, that is, a series circuit structure on a d-axis magnetic equivalent circuit is applied.

3.3 Conventional Series Type Hybrid PM Motor Performance Characteristics and Problems

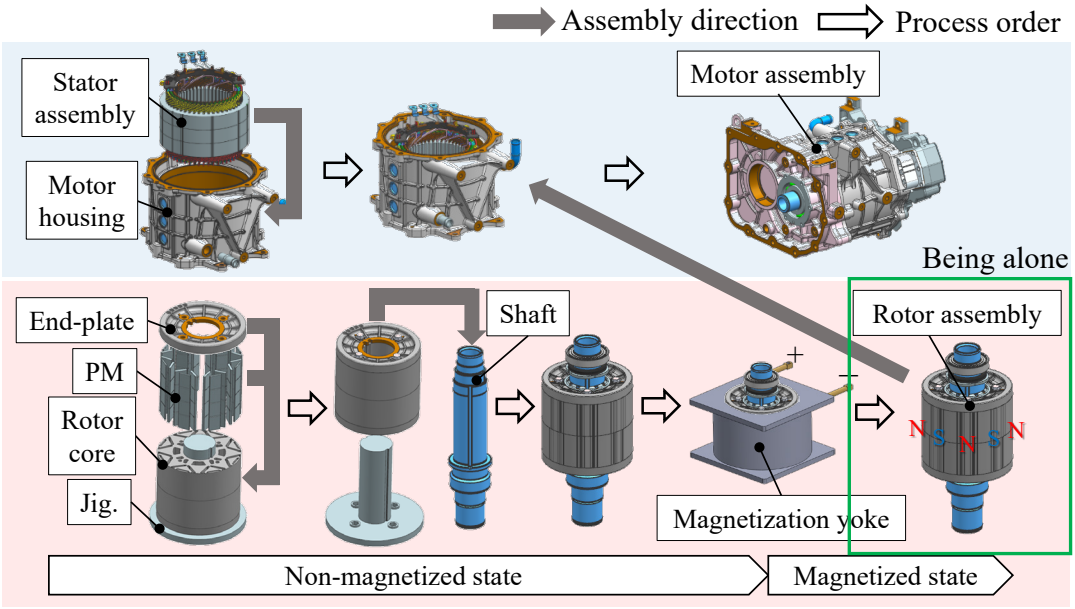

Fig. 3.16 Mass production process of traction motor

This chapter describes the design variables, performance characteristics, PM cost and problems of the conventional S-HPMM under the same stator as the target motor, and suggests alternatives to improve it.

3.2.1 Define Design Variables

The structure that fundamentally solves these problems is S-HPMM. The P-HPMM has a structure in which the magnetic flux of each PM is concentrated in the d-axis direction, whereas the S-HPMM has a structure in which the magnetic flux of each PM is interlinked.

Fig. 3.15 shows the basic structure, design variables of the conventional S-HPMM. As shown in Fig. 3.15, in the conventional S-HPMM, Nd-PM is placed on the d-axis, and Fe-PM is placed on the q-axis. Such a structure was proposed in the literature [70], and the d-axis magnetic equivalent circuit is shown in Fig. 2.6(b).

The maximum average torque for each design variable of the S-HPMM was reviewed as follows. In Fig. 9(a), h_s and h_e are 32.1mm and 64.1mm, respectively, which is the same as the previously reviewed P-HPMM. w_{fe} is fixed at 32mm. Table 3.4 shows the design variable range for each PM dimension of S-HPMM. The width ratio k_w and thickness ratio k_h of each PM is as defined in (3.2.1.1). where k_w ranges from 0.63 to 0.72 and k_h ranges from 0.38 to 1.2.

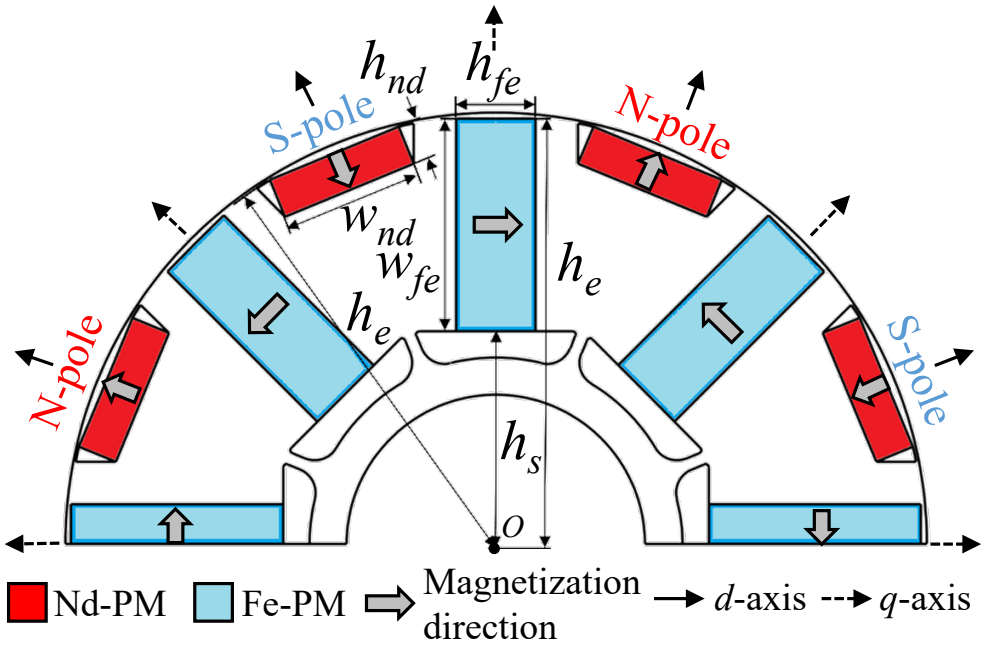

Fig. 3.17 Basic structure and design variable of conventional S-HPMM

Table. 3.4 Range of S-HPMM design variables

Design variables	Unit	Min.	Max.
W_{nd}	mm	20	23
W_{fe}	mm	32 (Constant)	
h_{nd}	mm	6	12
h_{fe}	mm	10	16
k_w	-	0.63	0.72
k_h	-	0.38	1.2

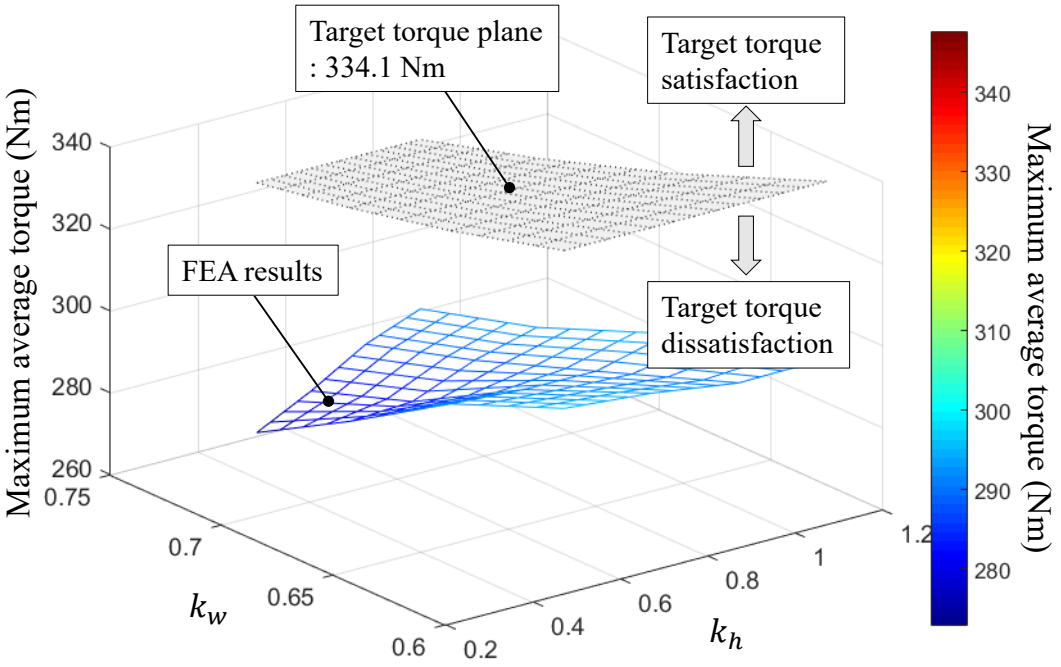

Fig. 3.18 Maximum average torque distribution for k_h, k_w of the conventional S-HP MM

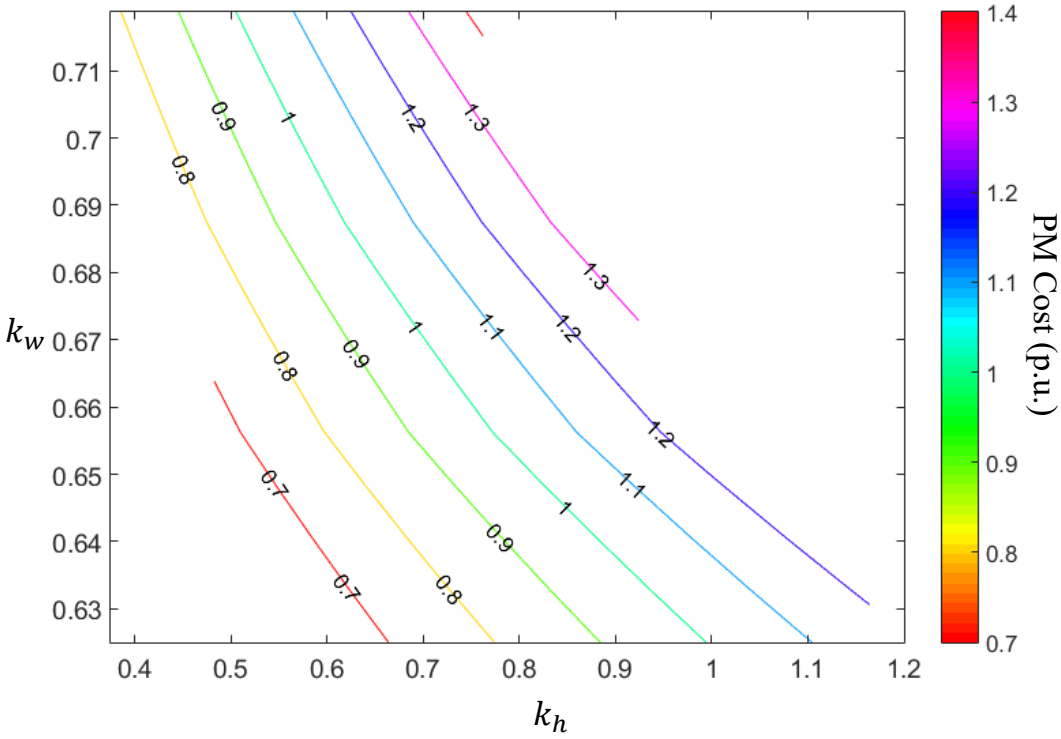

Fig. 3.19 PM cost distribution for k_w and k_h of the conventional S-HPMM.

Fig. 3.18 and 3.19 show the maximum average torque and PM cost distribution for k_w and k_h of the conventional S-HPMM. As shown in Fig. 3.19, the conventional S-HPMM was reviewed in a PM cost range similar to that of the conventional P-HPMM. However, as shown in Fig. 3.18, the target torque is not met. The increase in the maximum average torque according to the increase in k_w and k_h is limited compared to the P-HPMM. However, even if the PM usage is reduced, the decrease in the maximum average torque is small compared to the P-HPMM. This means that the reluctance torque is smoothly generated compared to the P-HPMM. Considering these characteristics of S-HPMM, Section 3.4 presents a novel S-HPMM with improved reluctance torque.

3.4 Proposal of improved Series Type Hybrid PM Motor

In this chapter, an S-HPMM-based model with dramatically improved reluctance is proposed. First, a simple mathematical proof is presented for the reason why the PM flux of S-HPMM is lower than that of P-HPMM, and therefore the necessity of increasing the L_q component is explained. In addition, the design concept and parameters of the proposed model, design procedure, torque and demagnetization characteristics will be described.

3.4.1 Comparison of PM Flux Linkage of each Hybrid PM Motor

The characteristic that the PM flux linkage of P-HPMM is greater than that of S-HPMM can be estimated based on *d*-axis magnetic equivalent circuit. In Fig. 2.6(a) PM flux linkage of P-HPMM can be expressed as follows using Milman's theorem.

$$\psi_{pm\_p}=\frac{\frac{F_{nd}}{R_{nd}}+\frac{F_{fe}}{R_{fe}}+\frac{0}{R_{sg}}}{\frac{1}{R_{nd}}+\frac{1}{R_{fe}}+\frac{1}{R_{sg}}}\cdot\frac{1}{R_{sg}}=\frac{F_{nd}R_{fe}+F_{fe}R_{nd}}{R_{fe}R_{sg}+R_{sg}R_{nd}+R_{nd}R_{fe}} \tag{3.4.1.1}$$

In Fig. 2.6(b), PM flux linkage of S-HPMM can be expressed as follows using Ohm's law and Kirchhoff's law.

$$\psi_{pm\_s}=\frac{F_{nd}+F_{fe}}{R_{nd}+R_{fe}+R_{sg}} \tag{3.4.1.2}$$

Assuming $\psi_{pm\_p}>\psi_{pm\_s}$, it can be expressed as an inequality as follows.

$$\frac{F_{nd}R_{fe}+F_{fe}R_{nd}}{R_{fe}R_{sg}+R_{sg}R_{nd}+R_{nd}R_{fe}}>\frac{F_{nd}+F_{fe}}{R_{nd}+R_{fe}+R_{sg}} \tag{3.4.1.3}$$

By introducing the ratio m between the reluctance of each PM, the range of m can be expressed as follows.

$$m=\frac{R_{fe}}{R_{nd}} \quad \begin{cases} m=1 & R_{nd}=R_{fe} \\ 0<m<1 & R_{nd}>R_{fe} \\ m>1 & R_{nd}<R_{fe} \end{cases} \tag{3.4.1.4}$$

In (3.4.1.4), it is defined as $R_{fe}=mR_{nd}$, and substituting it into (3.4.1.3), it is as follows.

$$\frac{mF_{nd}R_{nd}+F_{fe}R_{nd}}{mR_{nd}R_{sg}+R_{sg}R_{nd}+mR_{nd}R_{nd}}>\frac{F_{nd}+F_{fe}}{R_{nd}+mR_{nd}+R_{sg}} \tag{3.4.1.4}$$

If (3.4.1.4) is arranged for R_{nd}, it is as follows.

$$R_{nd}>\frac{mF_{nd}+F_{fe}}{F_{nd}+m^2F_{fe}}\cdot R_{sg} \tag{3.4.1.5}$$

When m=1 in (3.4.1.5), the following result can be obtained.

$$R_{nd}>R_{sg} \tag{3.4.1.6}$$

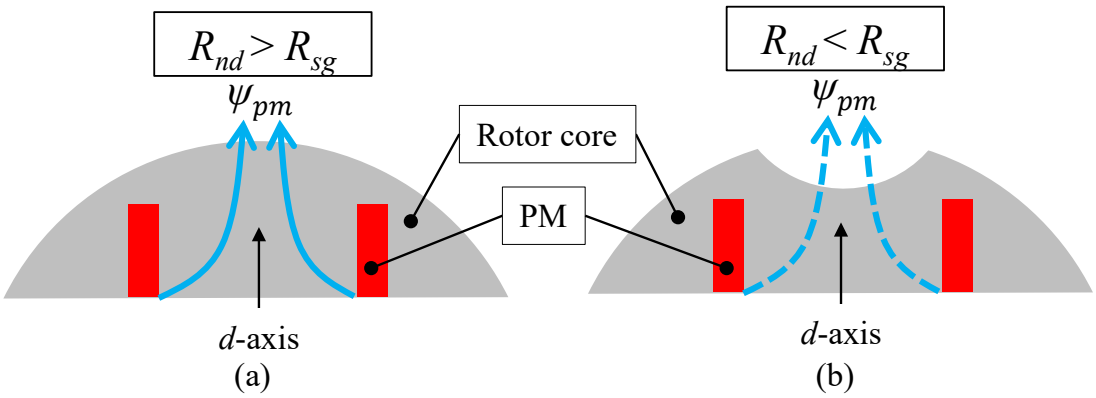

Fig. 3.20 Example of rotor shape according relationship to the inequality of R_{nd} and R_{sg}

That is, if the condition of (3.4.1.6) is satisfied, $\psi_{pm\_p} > \psi_{pm\_s}$ holds. The physical meaning of (3.4.1.6) is that if the reluctance of each PM is the same, the reluctance of the air-gap and the core should be smaller than the reluctance of the PM, regardless of the magnitude of the MMF of each PM.

Fig. 3.20 shows an example of the rotor core shape according to the inequality relationship between R_{nd} and R_{sg}. In the *d*-axis flux path, when the magnetic saturation is not high and the rotor core has a cylindrical structure, $R_{nd} > R_{sg}$ is satisfied.

However, when the magnetic saturation is high on the d-axis flux path or when the reluctance is artificially increased in the *d*-axis air gap region, $R_{nd} < R_{sg}$ may be obtained. Considering that most of the IPMSM designs adopt the cylindrical structure of the rotor core on the *d*-axis magnetic path and are studied in the direction of reducing magnetic saturation, it can be generally regarded as $R_{nd} > R_{sg}$.

Based on this logic, even when the coefficient part of Rsg in (3.4.1.5) is also greater than 1, it can be considered that it is consistent with the general motor design condition. This can be expressed as (3.4.1.7).

$$\frac{mF_{nd}+F_{fe}}{F_{nd}+m^2F_{fe}}>1 \tag{3.4.1.7}$$

If (3.4.1.7) is arranged as a term for MMF, it is expressed as (3.4.1.8).

$$F_{nd}>\frac{m^2-1}{m-1}F_{fe} \tag{3.4.1.7}$$

Except for m=1 in (3.4.1.7), it means that $F_{nd} > F_{fe}$ always holds for $0<m<1$, $m>1$. The physical implication is that when each PM of different reluctance and magneto-motive force is applied on a cylindrical rotor structure, the parallel configuration can achieve higher PM flux linkage compared to the series configuration, and $\psi_{pm\_p}>\psi_{pm\_s}$ is true. Therefore, the advantages and disadvantages of each HPMM can be summarized in Table 3.5.

Table. 3.5 Advantages and disadvantages of each HPMM

Classification	P-HPMM	S-HPMM
Advantages	High PM flux linkage	No problem of demagnetization of Fe-PM by Nd-PM
Disadvantages	Demagnetization of Fe-PM by Nd-PM	Low PM flux linkage

3.4.2 Necessity of increasing L_q, Design Concept and Variables

In IPMSM, the electromagnetic torque can be calculated according to the vector diagram derived from the *d*-*q* rotor frame using the Park transform as shown in Fig. 3.21(a). The electromagnetic torque of IPMSM consists of PM torque and reluctance torque and is expressed as (2.4.13). For (12), the torque characteristics are plotted, as shown in Fig. 3.21(b).

Under the same PM usage, the PM flux linkage of S-HPMM is lower than that of P-HPMM. Low PM flux linkage means high *d*-axis reluctance, and L_d is also lower than P-HPMM. If the *q*-axis flux path is structurally secured in the S-HPMM and the L_q component is increased, the reluctance torque can be increased due to the increase of the saliency ratio (L_d–L_q). That is, the S-HPMM has a lower PM flux linkage compared to the P-HPMM, but has a high *d*-axis reluctance, so it is advantageous in terms of generating reluctance torque.

Fig. 3.22 shows the S-HPMM-based model and main design variables proposed in this thesis. Nd-PM is divided into three and is placed similarly to U-shape on the *d*-axis. In addition, Fe-PM is divided into two and is placed similarly to the A-shape on the *q*-axis. As a result, the magnetic fluxes of each PM on the *d*-axis magnetic equivalent circuit are in series configuration with each other, and the L_d component can be lowered. At the same time, it is possible to increase the L_q component by securing more *q*-axis flux paths compared to the conventional S-HPMM. Therefore,

the saliency ratio (L_d–L_q) is increased, and the proposed model can improve the reluctance torque. In addition, since the proposed model is a series configuration, it is possible to solve the problem of demagnetization of Fe-PM by Nd-PM of conventional P-HPMM.

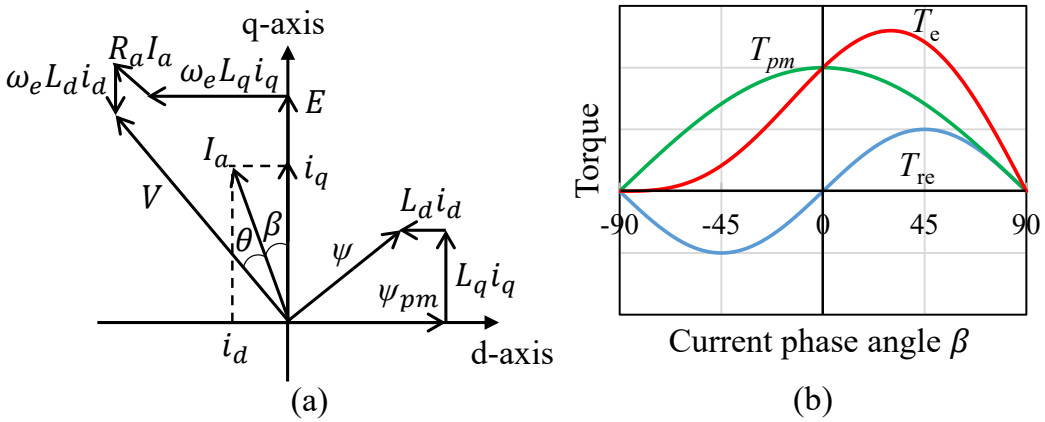

Fig. 3.21 Torque characteristic (a) Vector diagram in *d-q* reference frame (b) Torque characteristic. T_e: Total torque, T_{pm}: PM torque, T_{re}: reluctance torque.

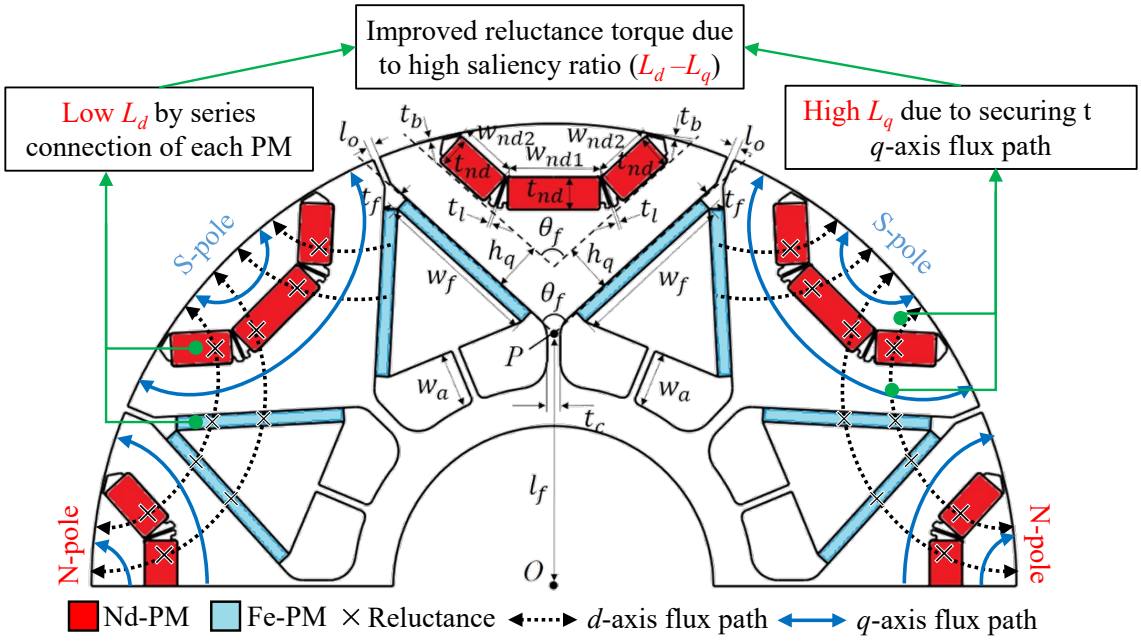

Fig. 3.22 Proposed model and design variables.

3.4.3 Design Process

Traction motors for electric vehicles operate at variable speeds over a wide speed range. It is necessary to secure an appropriate safety factor to maintain the stiffness of the rotor core in the high-speed operation range. Therefore, the related design variables t_c, t_b and t_l are considered first. The target value is to meet the safety factor of 1.32 or higher, and it is the same as the target motor. The selected values are 1.86, 0.35, and 0.3 mm, respectively, and the mechanical stress analysis results are presented in Fig. 3.33 and Fig. 3.34.

The next value to set is l_f, which is the starting point of PM insertion. When l_f is large, the amount of PM that can be used is small, so the torque is small. Therefore, if the target torque is not met, the value is reduced and reviewed. Currently, the value suggested is 35.8mm, which is similar to the 32.1mm of the conventional P-HPMM and S-HPMM presented in this paper. The next value to set is w_f, the width of Fe-PM. w_f is structurally chosen with the largest value. This is because, if the PM torque is improved by generating as much Fe-PM magnetic flux as possible, the amount of Nd-PM used can be relatively reduced. Therefore, the structurally largest value of 23.5 mm was selected.

The next values to set are Fe-PM slot opening lo and the air layer w_a at the bottom of Fe-PM. Leakage flux is generated at the upper and lower parts of Fe-PM. When l_o is applied, the leakage flux is reduced and the PM torque is improved. These results are shown in Fig. 3.25. If l_o is increased, the q-axis flux path becomes narrower. This can result in lower reluctance torque. Based on this tendency, l_o was chosen as 1 mm. w_a is related to the reduction of the leakage flux at the lower part of Fe-PM and the weight reduction of the rotor. When this value is increased, the mechanical stress tends to increase. $\underline{w_a}$ was selected to be 8 mm within the allowable range of safety factors of t_c, t_b, and t_l.

The next values to determine are the thickness t_f and t_{nd} of each PM. The thickness of each PM is related to the demagnetization ratio and L_d. As the thickness of each PM increases, the demagnetization ratio and L_d become lower. The variable sensitive to demagnetization ratio is the thickness t_{nd} of Nd-PM. The minimum t_{nd} for 0% demagnetization ratio at 160 ℃ was selected as 4.6mm. Fig. 3.27 shows the results of demagnetization analysis by PM temperature. In addition, the advantage of the model proposed in this paper is to improve the reluctance torque by enlarging

the q-axis flux path. The reluctance torque is related to the saliency ratio (L_d–L_q). At this time, L_d was selected at a level similar to the target motor. Previously, t_{nd} was selected as 4.6 mm in consideration of the demagnetization ratio, and t_f was selected as 2 mm in consideration of L_d of the target motor. The analysis results of L_d and L_q are shown in Fig. 3.31.

Next, select h_q, which is the q-axis flux path, and w_{nd2}, which is the width of Nd-PM. At this time, w_{nd1} is temporarily fixed. When h_q is increased under these conditions, w_{nd2} naturally decreases. As h_q increases, the q-axis flux path is secured, and the reluctance torque increases, but the PM torque decreases due to the decrease of w_{nd2}. Through the adjustment between these two variables, the optimum point of the total torque including the reluctance torque and PM torque can be found. At this time, h_q and w_{nd2} were selected to be 7 mm and 8.5 mm, respectively.

The last value to be determined is the width W_{nd1} of Nd-PM and the angle θ_f of Fe-PM. If each variable is gradually increased, PM torque and reluctance torque will increase simultaneously. As w_{nd1} increases, the magnetic flux of Nd-PM increases, resulting in an increase in PM torque. In addition, when θ_f increases, the q-axis magnetic flux is smoothly generated, and the L_q component increases and the reluctance torque is improved. This trend is shown in Fig. 3.24 and W_{nd1} and θ_f were selected as 13 mm and 96°, respectively.

13 variables were selected through the design process as shown in Fig. 3.23, and the dimensions for each design variable are shown in Table 3.6.

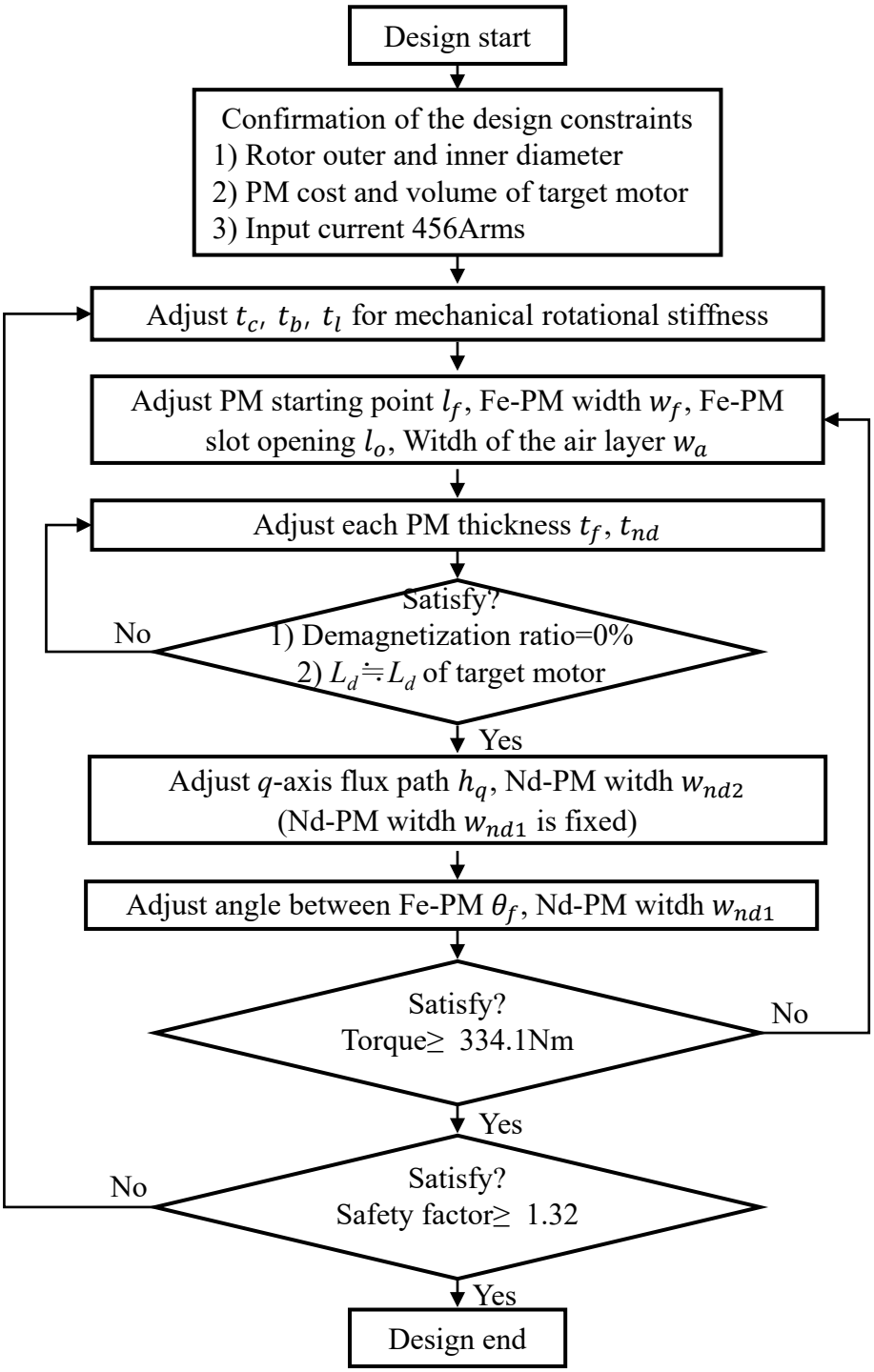

Fig. 3.23 Design process of the proposed model.

Table. 3.6 Main dimension of the designed motor

Design variables	Unit	Dimension
t_c, t_b, t_l	mm	1.86, 0.35, 0.3
lf	mm	35.8
θ_f	deg	96
t_f, w_f, w_a	mm	2, 23.5, 8
h_q	mm	7
w_{nd1}, w_{nd2}, t_{nd}	mm	13, 8.5, 4.6
l_o	mm	1

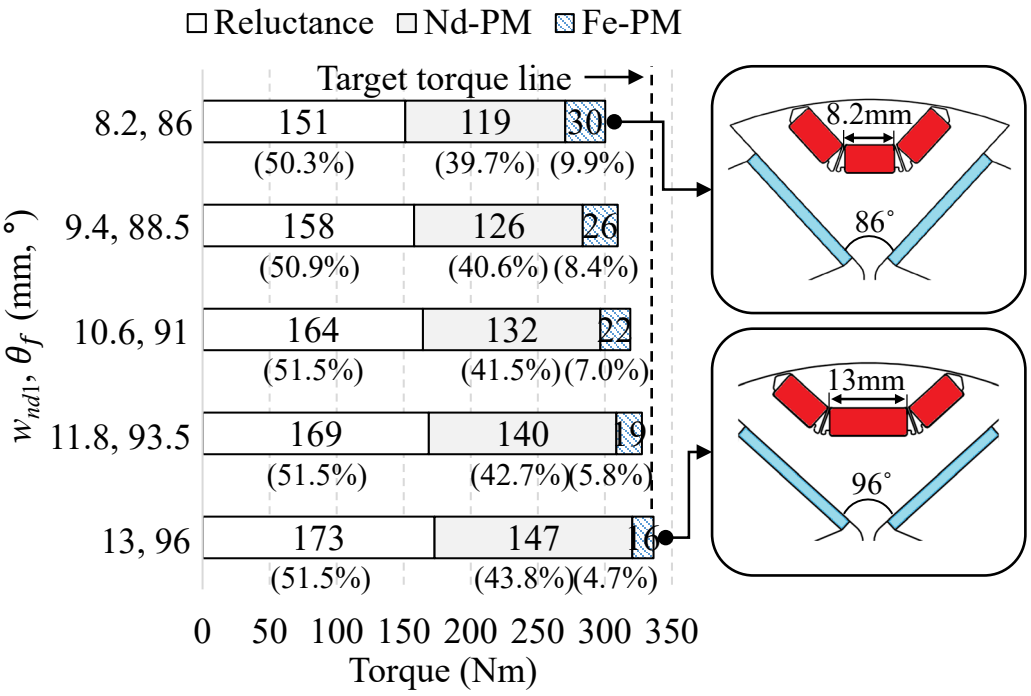

Fig. 3.24 Torque characteristics for change in design variables w_{nd1}, θ_f.

3.4.4 Torque Characteristics according to Changes in Design Variables

Fig. 3.24 shows the torque characteristics according to the design variable w_{nd1}, θ_f change. Other variables are the same as in Table 3.6. When w_{nd1} and θ_f are 8.2 mm and 86 °, respectively, the total torque is 300 Nm, which is 90 % of the target torque. In addition, the amount of Nd-PM used is 52.4 % of that of the target motor. When w_{nd1} and θ_f are expanded to 13 mm and 96 °, respectively, the total torque is 336.2 Nm, which satisfies the target torque. The amount of Nd-PM used is 62.2 %.

As w_{nd1} and θ_f increase, the reluctance torque and the PM torque by Nd-PM increase, while PM torque by Fe-PM tends to decrease. The increase in the reluctance torque is due to the effect that the q-axis flux path is more secured and the L_q component is increased as the corresponding variable increases. The PM torque by Nd-PM is du e to the effect of the increase of the corresponding magnetic flux as the surface area of Nd-PM on the d-axis flux path increases. On the other hand, Fe-PM is placed more inward from the rotor core surface. Accordingly, as the magnetic path of the flux generated in Fe-PM becomes longer from the rotor core surface, the related generated torque is reduced.

The tendency of torque according to changes in w_{nd1} and θ_f indicates that the reluctance torque improves as the q-axis magnetic flux path is secured in S-HPMM. It also shows that the magnetic

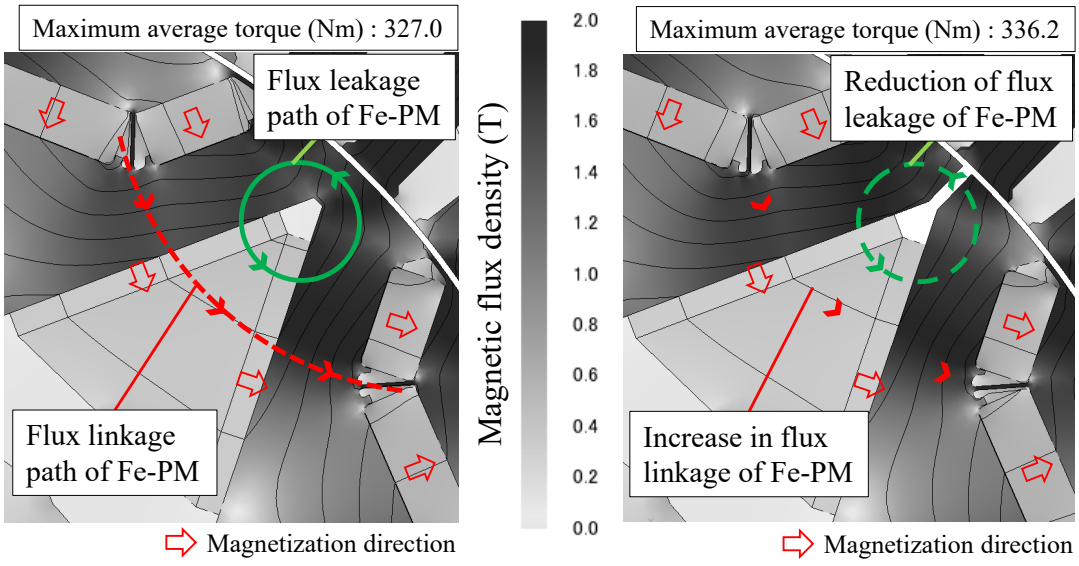

Fig. 3.25 Torque characteristics for change in design variables l_o.

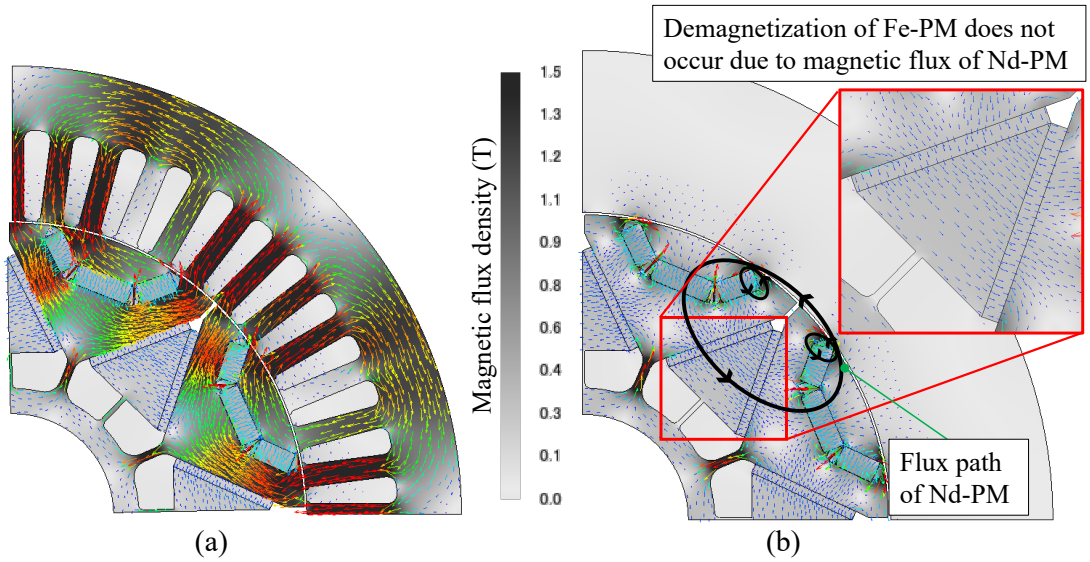

Fig. 3.26 Flux density distribution of the designed motor (a) maximum average torque point with stator (b) no-load condition without stator.

flux generated by Fe-PM contributes to improving the overall torque and reducing the Nd-PM usage.

Fig. 3.25 shows the torque characteristics according to the design variable l_o. In the proposed model, Fe-PM is placed in the q-axis in a shape similar to the spoke type. As a result, a large amount of leakage magnetic flux may be generated at the upper and lower ends of the Fe-PM. Therefore, when l_o is applied as in Fig. 3.25, it is possible to reduce the leakage flux at the upper end of Fe-PM. In the proposed model, in the absence of l_o, the total torque is 327 Nm. When l_o was applied by 1 mm, the total torque was 336.2 Nm, which improved the total torque by 2.7 %. This result also indicates that the magnetic flux of Fe-PM contributes to the total torque.

3.4.5 Flux Density Distribution

Fig. 3.26(a) shows the magnetic flux density distribution at the maximum torque point. It shows that most of the total flux linkage is generated through the q-axis flux path of the rotor. Fig. 3.26(b) shows the magnetic flux density distribution when there is no stator. As mentioned above, in the conventional P-HPMM, the strong magnetic flux of Nd-PM acts as a reverse magnetic field on the Fe-PM side, causing local demagnetization of Fe-PM. However, as shown in Fig. 3.26(b), in S-HPMM, the magnetic flux of each PM is interlinked, so the demagnetization of Fe-PM by the

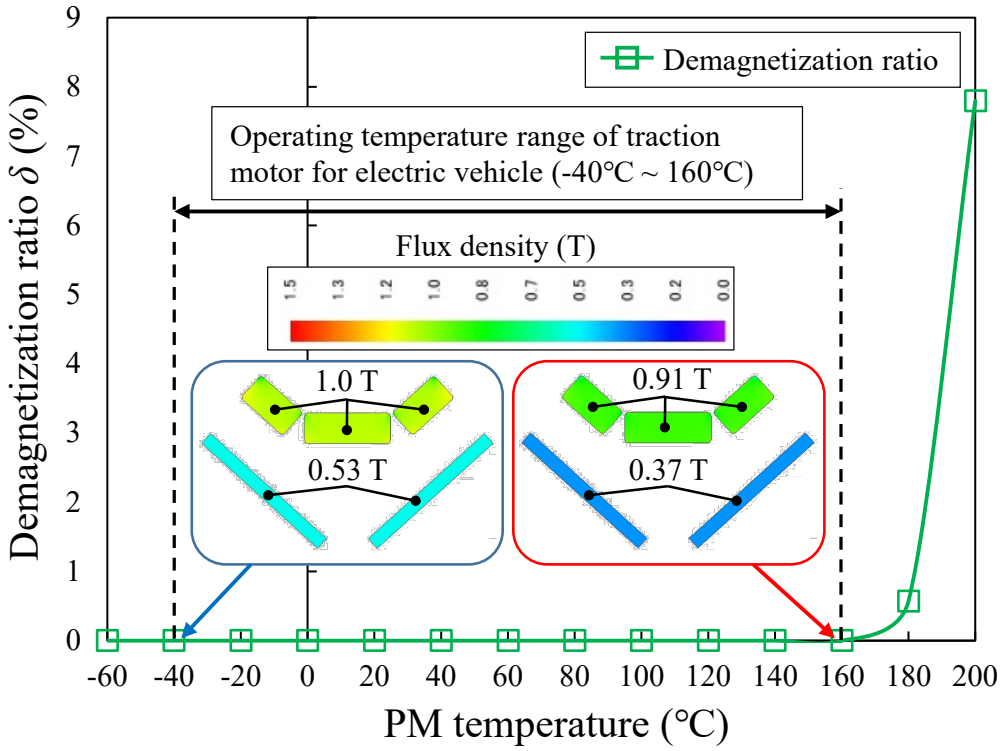

Fig. 3.27 Demagnetization ratio δ by PM temperature after application of demagneti zing current (456Arms, *d*-axis current only).

magnetic flux of Nd-PM does not occur. Therefore, when considering the mass production process of the traction motor as shown in Fig. 3.16, it can be said that S-HPMM is suitable for industrial use compared to P-HPMM.

3.4.6 Review of Irreversible Demagnetization Properties

The operating temperature range of traction motors for electric vehicles is known to be from −40 to 160 ℃. It should be reflected in the design so that there is no performance degradation due to demagnetization of PM as well as maintenance of the insulation performance of the motor within this operating temperature. In the traction motor, flux weakening control is applied for high-speed driving. In order to increase the motor speed within the limited input voltage range, the *d*-axis current is gradually increased to reduce the air-gap magnetic flux density.

This control means physically applying a high reverse magnetic field from the stator to the PM

of the rotor. Therefore, in this paper, assuming the worst condition, the maximum current of 456 Arms is applied only to the *d*-axis, and the demagnetization ratio δ is defined as follows.

$$\delta = \frac{E_1 - E_2}{E_1} \times 100\ (\%) \tag{3.4.6.1}$$

Where E_1 and E_2 are the RMS values of the back-EMF before and after the demagnetization current is applied, respectively.

Fig. 3.27 shows the demagnetization ratio by PM temperature. In Nd-PM, the coercive force decreases as the temperature increases, and the coercive force increases as the tem-perature decreases. However, in Fe-PM, the change of coercive force according to PM temperature change acts opposite to that of Nd-PM. That is, Nd-PM tends to be demagnetized in a high-temperature region, whereas Fe-PM is easily demagnetized in a low-temperature region. Therefore, when both PM are applied to the traction motor, it is required to analyze the demagnetization characteristics in both low and high temperature regions. As shown in Fig. 3.27, the demagnetization ratio δ of the designed motor is 0 % at the PM temperature of −40 and 160 ℃. The figure in the graph shows the magnetic flux density distribution of each PM after the application of demagnetizing current.

It does not exceed the knee point of each PM in most areas, and local demagnetization characteristics do not appear either.

3.5 Comparison with Target Motor

3.5.1 Shape, Weight and PM Cost

Fig. 3.28 shows a comparison between the target motor and the designed motor for rotor core shape. In the target motor, Nd-PM is placed in a delta type, and one hole per pole is applied inside the rotor core to reduce weight. In the designed motor, Nd-PM is placed as U-type and Fe-PM as A-type, and a lot of empty space is applied to the lower part of Fe-PM compared to the target motor to reduce the leakage flux of Fe-PM.

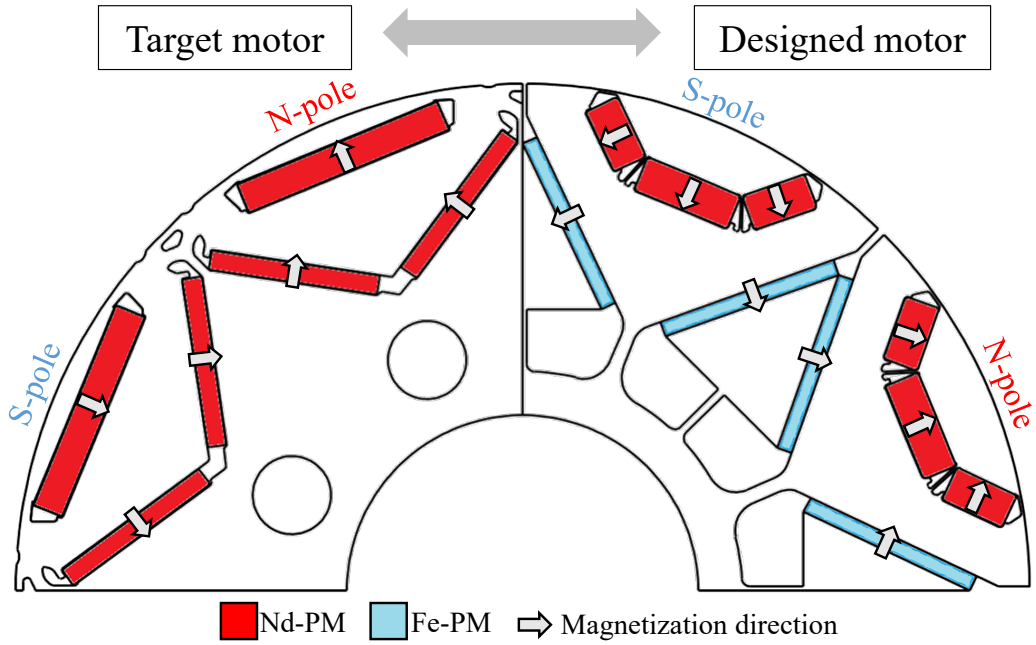

Fig. 3.28 Comparison of rotor core shape.

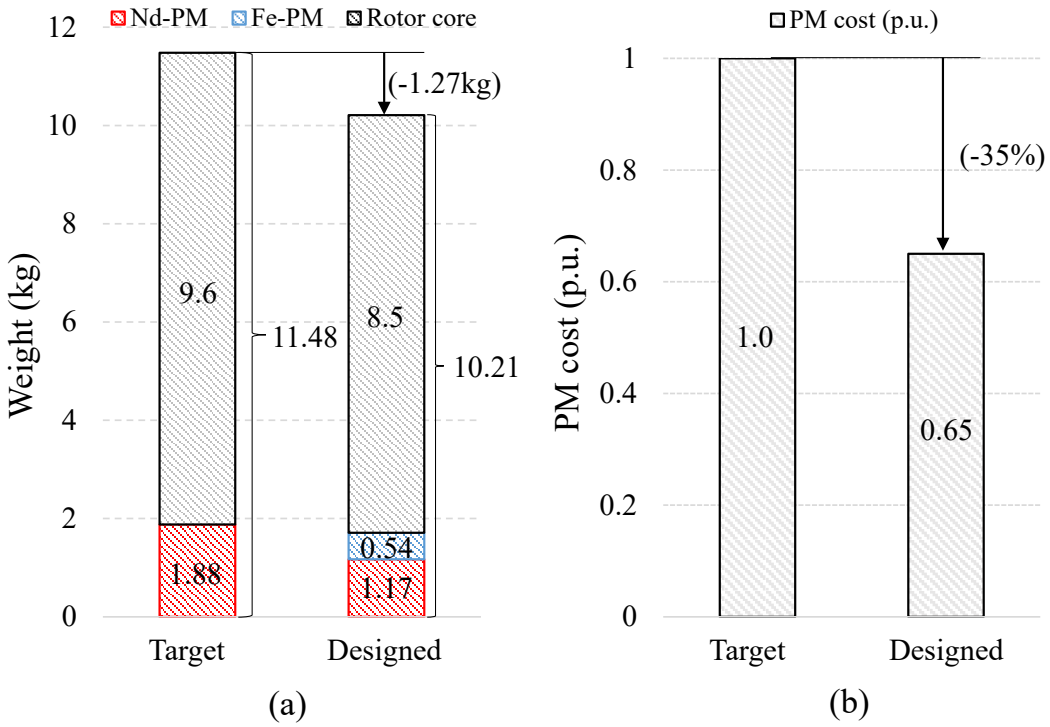

Fig. 3.29 Comparison of (a) Weight (b) PM cost.

Therefore, as shown in Fig. 3.29(a), the weight of the rotor core of the target motor is 9.6 kg, while the designed motor is 8.5 kg, which is 1.1 kg lower. In the case of Nd-PM usage, the target motor is 1.88kg, and the designed motor is 1.17 kg, which is 62.2 % of the target motor. In the case of Fe-PM usage, 0.54 kg was applied to the designed motor. When the rotor core and PM weights are combined, the target motor is 11.48 kg, and the designed motor is 10.21 kg, which is 1.27kg reduced. In addition, the PM cost of the designed motor was re-duced by 35 % compared to the target motor as shown in Fig. 3.29(b).

3.5.2 Coil Flux Linkage

Fig. 3.30 shows the fundamental wave amplitude val-ue of the coil flux linkage for each PM temperature under no-load condition. Overall, the target motor appears higher than the designed motor. This result means that the PM torque of the target motor becomes higher than that of the designed motor. At room tem-perature of 20 ℃, the target motor is 76.0 mWb, and the designed motor is 72.9 mWb, which is 4.2 % lower. Based on the operating temperature of 100 ℃, the target motor is 71.7 mWb, and the designed motor is 67.9 mWb, which is 4.0 % lower. The difference (Tar-get−designed) in amplitude between each motor in-creases until the PM temperature is 60 ℃, and then decreases thereafter. The reason the difference in amplitude value increases is that the temperature coefficient of the remanence Br of each PM is different. The temperature coefficient of Nd-PM is −0.1 %/℃, whereas that of Fe-PM is −0.2 %/℃. As the temperature increases, the decrease in the remanence becomes larger for Fe-PM than for Nd-PM. Accordingly, the difference in amplitude between the target motor and the designed motor increases as the temperature increases.

However, the reason the difference in amplitude value decreases after the PM temperature of 60 ℃ is the effect of the leakage flux. As the temperature of PM increases, the amount of flux linkage reaching the stator coil due to the lowered remanence decreases, and the amount of leakage flux converging through bridges and ribs near the PM increases relatively. This means that the change in the leakage flux due to the PM temperature rise is larger in the target motor than in the design motor, and the relevant dimensions that generate the leakage flux in the target motor are thicker.

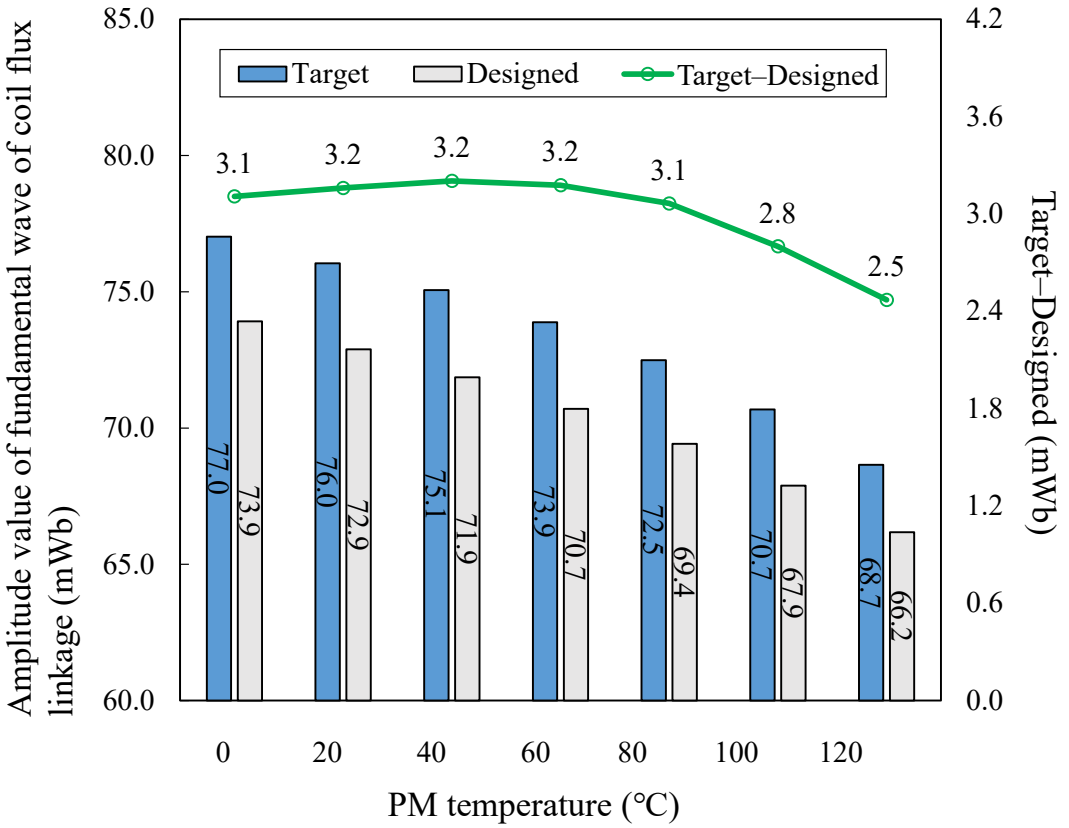

Fig. 3.30 Comparison of fundamental wave amplitude values of coil flux linkage by PM temperature under no-load condition.

Relevant dimensions to reduce PM's leakage flux have a trade-off relationship with maintaining rotor core stiffness when the rotor rotates at high speed. Therefore, as suggested in the design process in Fig. 3.23, not only the electromagnetic field analysis but also the structural analysis and the review are required. The relevant structural analysis results are presented in Section 3.5.5.

3.5.3 Inductance

Fig. 3.31(a) and (b) show the *d*- and *q*-axis inductance and saliency ratio (L_d/L_q) for each current phase angle. As shown in Fig. 31(a), the L_d of the target motor is lower than that of the designed motor.

However, since the *q*-axis flux path of the designed motor is more secured, the difference in the L_q component tends to gradually increase as the current phase angle increases.

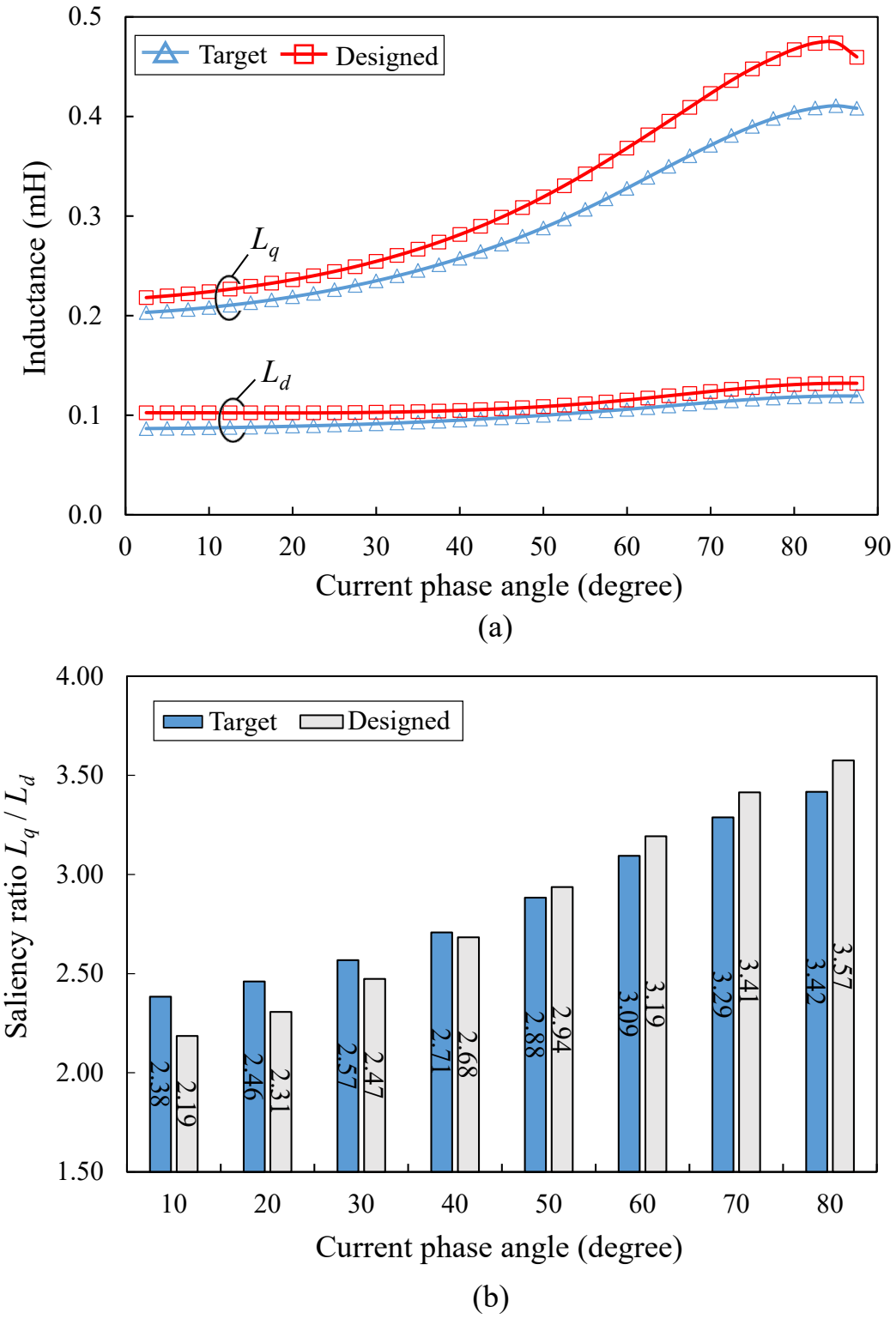

Fig. 3.31 Comparison of inductance (a) L_d and L_q (b) Saliency ratio (L_d/L_q).

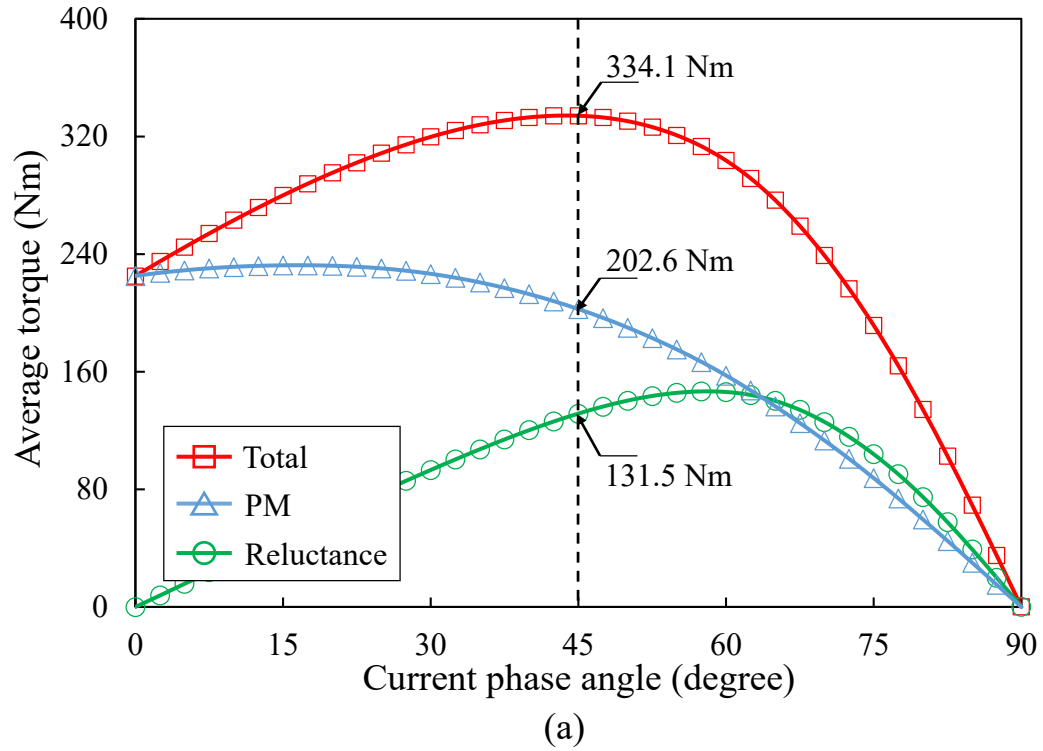

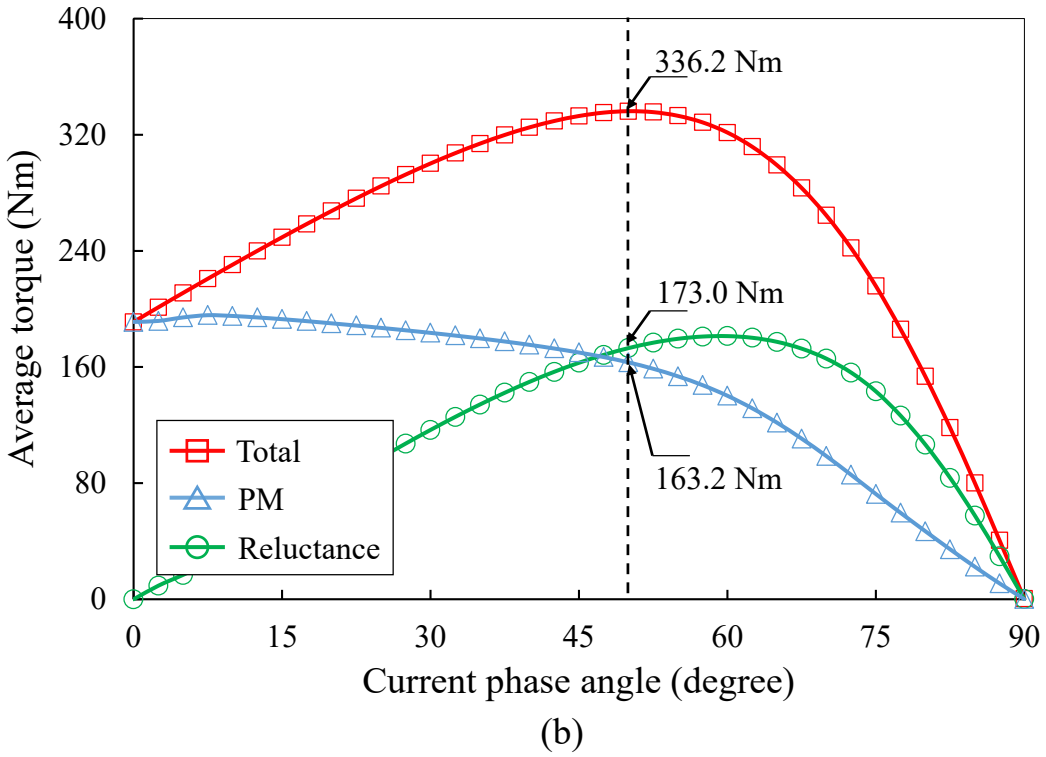

Fig. 3.32 Comparison of torque characteristics (a) target torque (b) designed motor.

As shown in Fig. 3.31(b), the saliency ratio is that the target motor is large before the current phase angle of 40 °, and the designed motor is large after that. Therefore, if the maximum average torque phase angle of each motor is generated at 40 ° or more, it can be expected that the reluctance torque of the designed motor is larger than that of the target motor.

3.5.4 Average Torque by Current Phase Angle

Fig. 3.32 shows total average torque, PM torque, and reluctance torque for each current phase angle. The total torque of the target motor is 334.1 Nm, and the designed motor is 336.2 Nm, which is similar to each other. At the maximum average torque point, the target motor's PM torque is 202.6 Nm and the reluctance torque is 131.5 Nm. The designed motor has a PM torque of 163.2 Nm and a reluctance torque of 173.0 Nm. For the target motor, the ratio of PM torque and reluctance torque is 6.1 versus 3.9 at the maximum average torque. On the other hand, the designed motor is 4.9 versus 5.1, and has a high proportion of relu-tance torque.

3.5.5 Stress Distribution at Maximum Speed Rotation

Table 3.7 shows the material properties of each part for structural analysis. The contour plots of Mises stress for the rotor of target motor and designed motor at 10,500 rpm are shown in Fig. 3.33 and Fig. 3.34 The maximum stress of the target motor is 319 MPa, and the safety factor is 1.32. The designed motor is 286 MPa, and the safety factor of 1.49. Therefore, compared to the target motor, the designed motor shows superior characteristics in terms of rigidity during high-speed rotation of the rotor. In addition, the maximum stress by speed of each model is shown in Fig. 3.35.

Table. 3.7 Material properties for structural analysis

Item	Unit	Core	Nd-PM	Fe-PM
Density	kg/m^3	7,650	7,620	5,100
Young’s modulus	GPa	180	160	190
Poisson’s ratio	-	0.3	0.24	0.35
Yield point	MPa	420	-	-

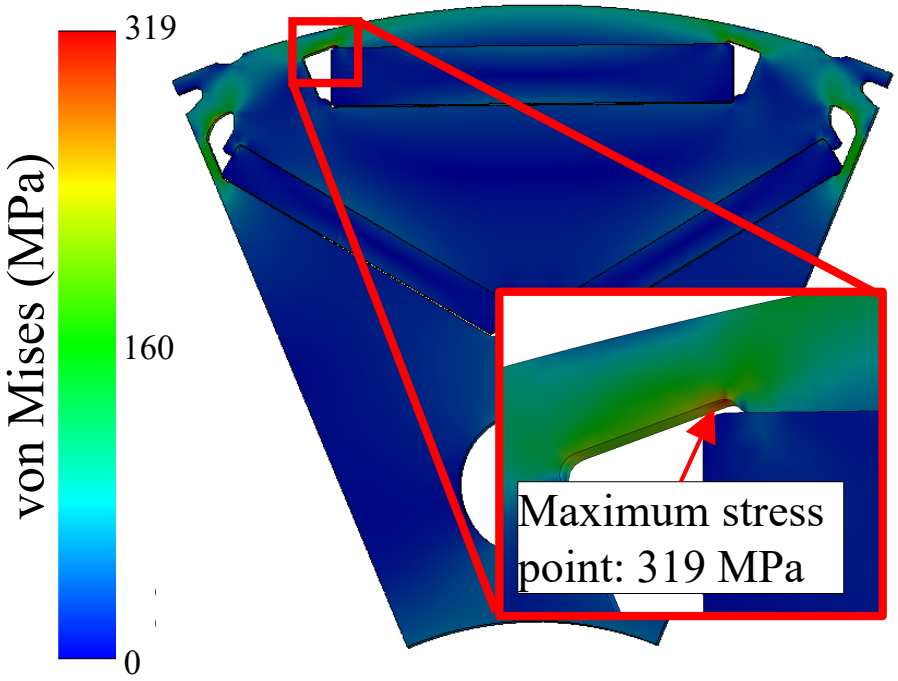

Fig. 3.33 Mises stress for target motor at maximum rotation speed 10,500rpm .

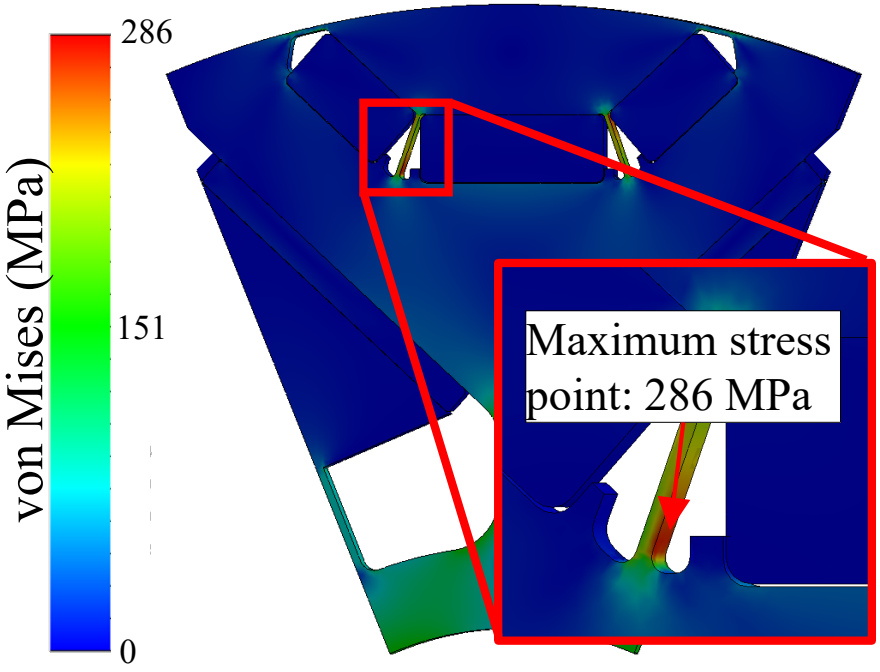

Fig. 3.34 Mises stress for designed motor at maximum rotation speed 10,500rpm .

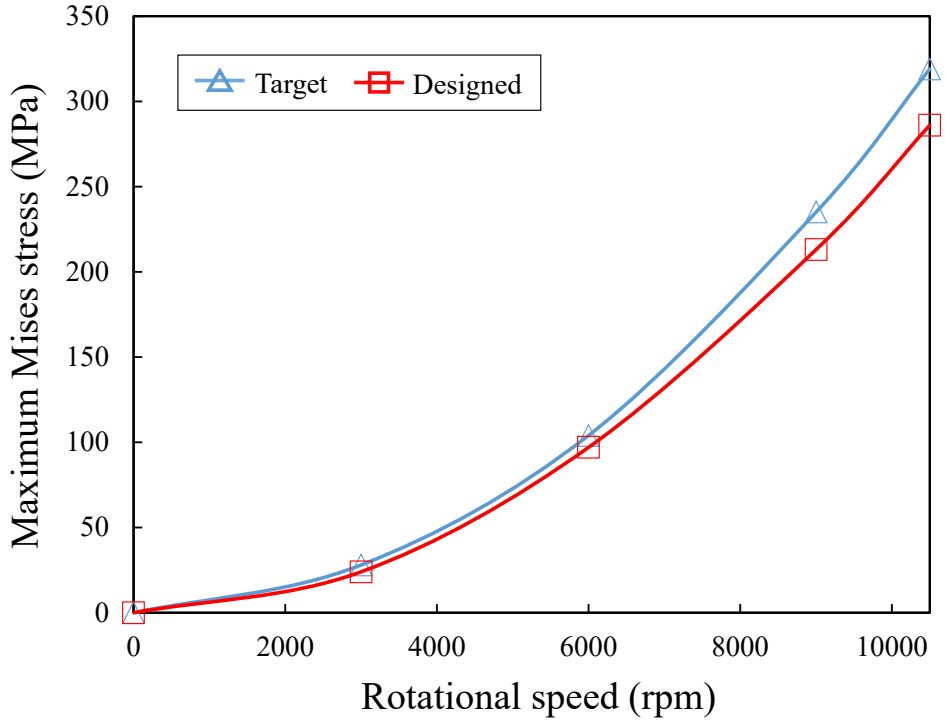

Fig. 3.35 Maximum Mises stress by rotation speed.

3.6 Summary for Chapter 3

Conventional HPMM can be divided into P-HPMM and S-HPMM according to the *d*-axis magnetic equivalent circuit. The conventional P-HPMM can obtain high PM flux linkage, but there is a problem in that Fe-PM is demagnetized by the strong magnetic flux of Nd-PM. The way to solve this problem is to adopt S-HPMM. However, in the conventional S-HPMM, it is difficult to improve the torque density due to the low PM flux linkage. Therefore, a novel S-HPMM with improved reluctance torque is proposed in this paper to solve these problems. The proposed motor realized the same torque density as the target motor, and at the same time reduced Nd-PM usage by 38% and PM cost by 35%. In addition, through the rotor topology and design procedure proposed in this paper, it can be expected to reduce the Nd-PM usage and PM cost of other general IPMSMs. The FEA results for target and designed motor based S-HPMM are summarized in Table 3.8.

Table. 3.8 Comparison results of target and designed motor

Item		Unit	Target	Designed
Weight	Rotor core	kg	9.6	8.5
	Nd-PM	kg	1.88	1.17
	Fe-PM	kg	-	0.54
	Total	kg	11.48	10.21
PM Cost		p.u.	1	0.65
Coil flux linkage		mWb	76.0	72.9
Maximum torque		Nm	334.1	336.2
PM torque		Nm	202.6	173.0
Reluctance torque		Nm	131.5	163.2
Safety factor		-	1.32	1.49

Chapter 4. Dy-free Hybrid PM Motor for HEV traction

Nd-PM can achieve a coercivity of up to 21 kOe without dysprosium due to the development of manufacturing technology. However, due to the high-temperature operation characteristics of vehicle traction motors, Nd-PM over 25kOe is mainly applied. In this chapter, 21kOe Nd-PM and 5.5 Fe-PM are simultaneously applied, and a hybrid PM motor (HPMM) suitable for environmental temperature conditions of HEV traction motors is proposed. As mentioned in Chapter 1, HPMM is divided into serial configuration and parallel configuration according to the arrangement of each PM. This chapter compares the pros and cons of each configuration and presents rotor structures that can improve demagnetization durability and torque characteristics. After comparing the performance characteristics of each rotor structure through 2D-FEM, finally, an HPMM suitable for vehicle traction motors is proposed. Also, the proposed HPMM shows the same torque and power density as the traction motor of TOYOTA PRIUS 4th generation hybrid electric vehicle (HEV), the target motor. At the same time, the proposed HPMM reduced the usage of Nd-PM by 47 % and the total PM cost by 10% compared to the target motor.

4.1 Development Trend of Dy-free Nd sintered PM and Necessity of Application to Traction Motor

Permanent magnet materials have made significant technological advances since the 1970s with the release of Nd-Fe-B using so-called rare earth materials. As shown in Fig. 4.1, by realizing high energy density of permanent magnet materials, it is actively applied to traction motors for automobiles that require mechanical output or high torque density.

PMs are characterized by having a large area hysteresis loop. PMs are commonly known as HARD ferromagnetic materials, as opposed to SOFT ferromagnetic materials such as steel and iron, which have a small loop area to minimize hysteresis losses [90]. Fig. 4.2 shows the hysteresis BH characteristics of each magnetic material. As shown in Fig. 4.2, the core physical concept that distinguishes the characteristics of each magnetic material is the coercive force. Coercive force refers to the strength of a magnetic field that can make the magnetization of a magnetic material to 0 even if the external magnetic field is removed, when a material becomes magnetic under the influence of an external magnetic field. Since most soft magnetic materials have low coercive

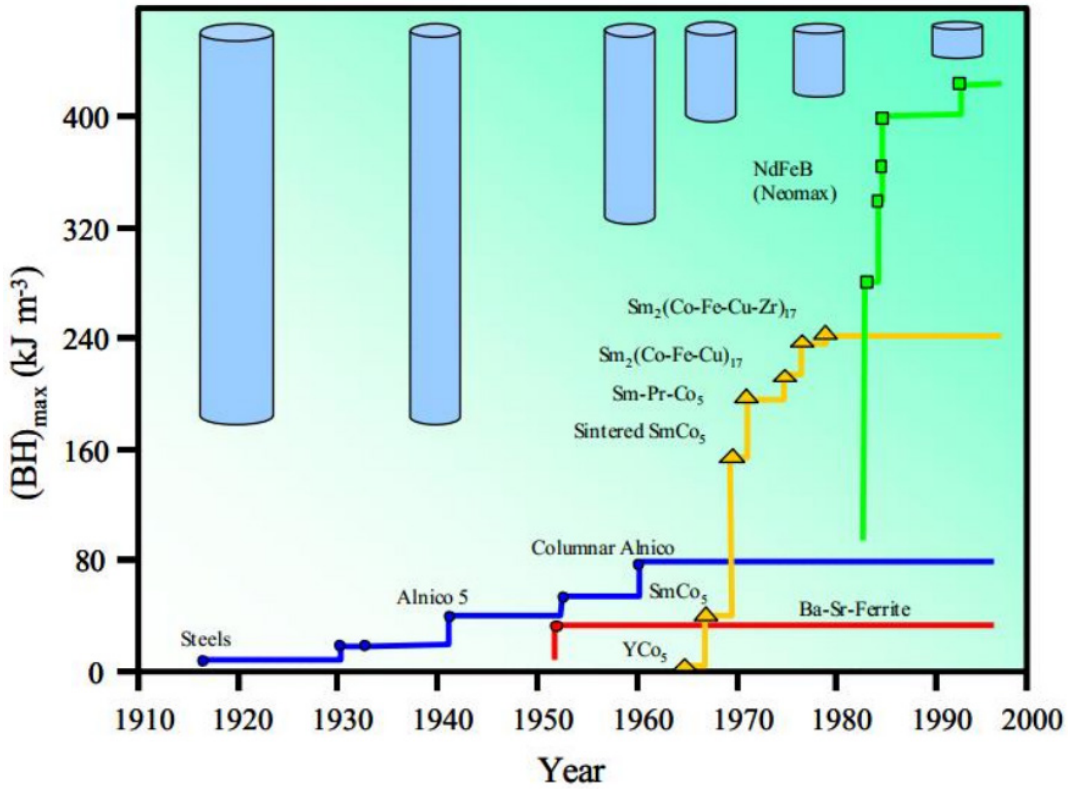

Fig. 4.1 Development trend of PM materials [36].

force, the orientation of the magnetic domain is easily changed in the same way as the vector direction of the external magnetic field. Conversely, a magnet, which is a hard magnetic material, does not easily change the orientation angle of the magnetic domain when the external magnetic field is low compared to the intrinsic coercive force.

Fig. 2.7 shows the product line for each PM manufacturer. The vertical axis represents the coercive force Hc, and the horizontal axis represents the residual magnetic flux density Br. As the coercive force increases, the residual magnetic flux density tends to decrease. This is because the specific element related to the coercive force is due to the physical property opposite to the direction of the vector of magnetization. Typically, dysprosium (Dy) and terbium (Tb), which are heavy rare earth elements, are contained to enhance the coercive force of Nd-PM. The higher the coercive force of Nd-PM, the larger the element is contained. These heavy rare earths are very expensive and are mined in large quantities in certain countries. In other words, there is a very large risk in terms of the supply chain. Fig. 4.3 shows the price trends of Nd, a light rare earth, and Dy, a heavy rare earth. In particular, the price of Dy, a heavy rare earth metal, rose sharply in 2011. As a result, industrial damage has occurred, and the industry is strongly demanding Dy-free

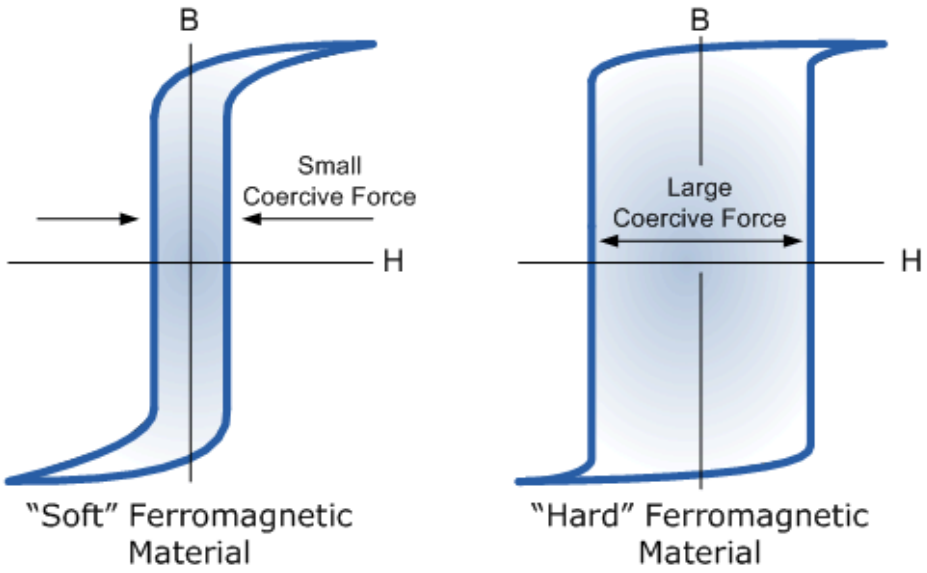

Fig. 4.2 Hysteresis *B-H* loop comparison of each ferromagnetic material [90].

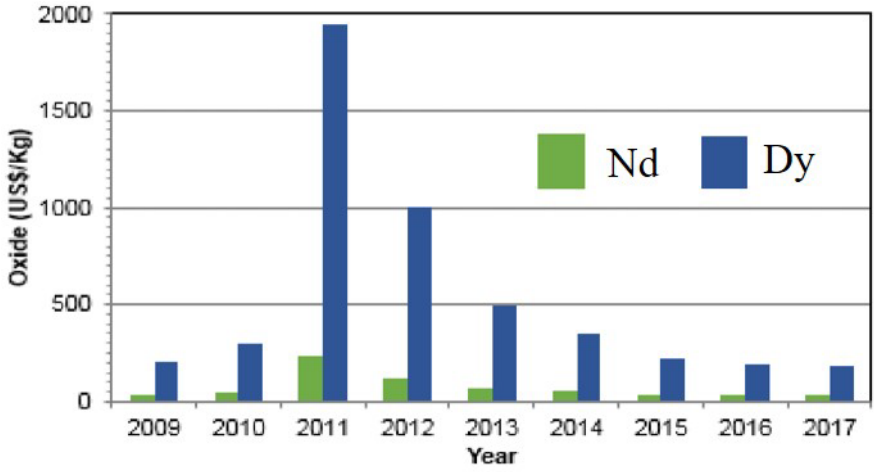

Fig. 4.3 Rare earth price track [44].

that does not use the corresponding raw material.

There are manufacturing process techniques such as fine powdering and grain boundary diffusion processes to improve coercivity without Dy. Through the improvement of the manufacturing process, Nd-PM can be Dy-free up to 21 kOe coercivity, but since vehicle traction motors need to secure demagnetization durability in high-temperature conditions, Nd-PM with a coercivity of 25 kOe or more is mainly applied [78, 80]. The development trend of such Nd-PM can be expressed as Fig. 4.4.

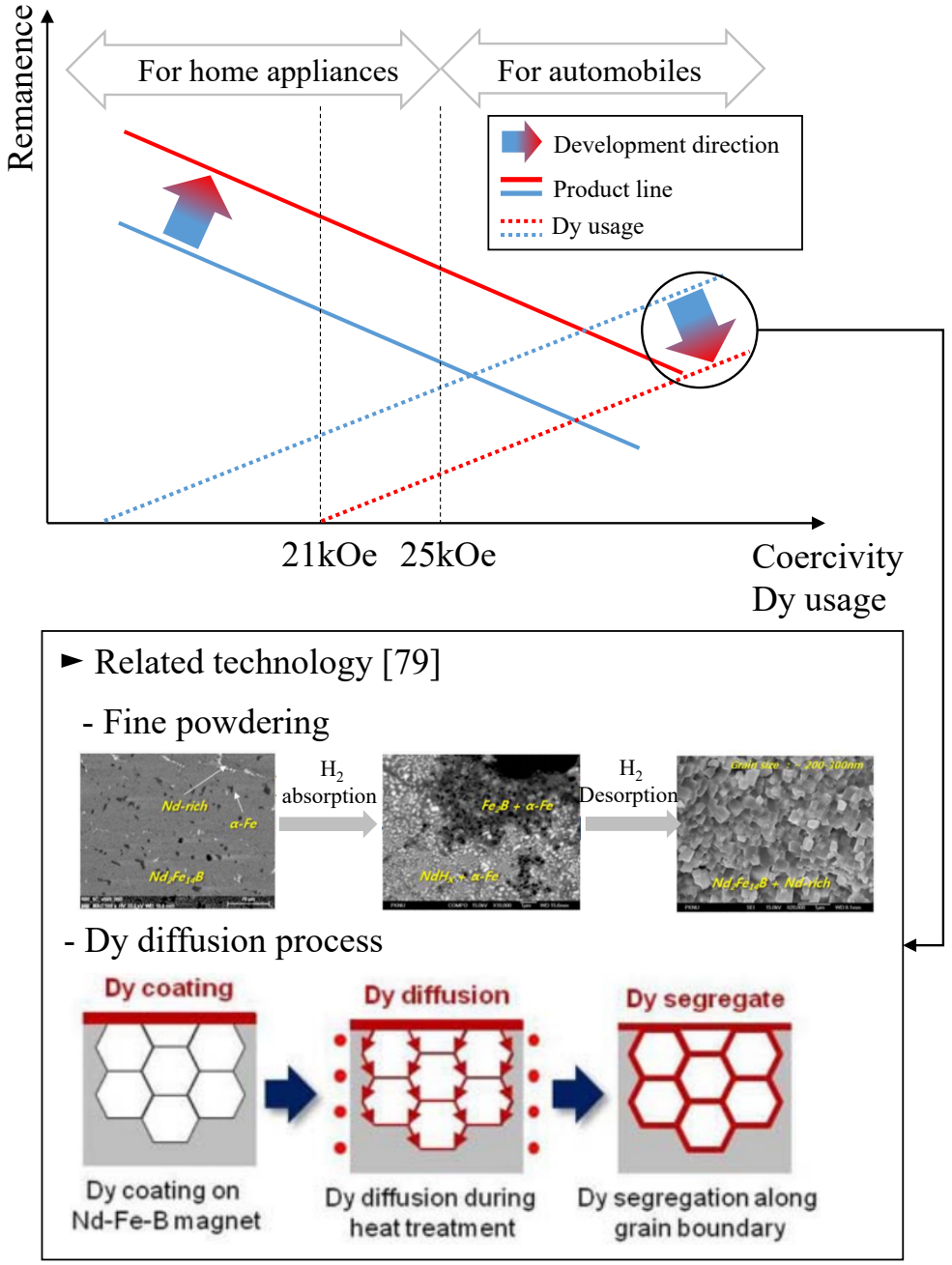

Fig. 4.4 Nd-PM development trend

As a traction motor without Dy, there are studies in terms of permanent magnet assisted synchronous motor (PMa-SynRM) with Fe-PM, induction motor (IM), separately excited synchronous motor (SESM) and switched reluctance motor (SRM). The shape and topology for the relevant cross-sectional area are shown in Fig. 4.5. However, IM, Fe-PM motor, and SRM do not realize the same torque density as the conventional IPMSM in terms of weight and volume[49, 54,

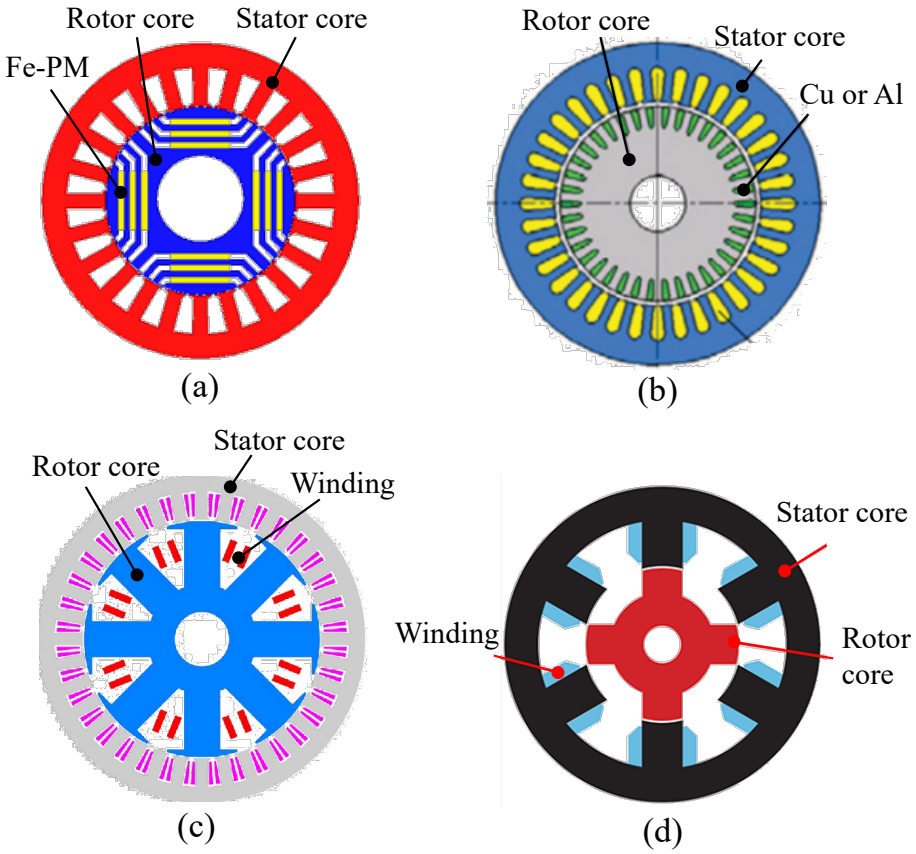

Fig. 4.5 Examples of Dy-free traction motor (a) PMa-SynRM (b) IM (c) SESM (d) SRM.

64]. SESM requires a non-contact power transfer device to be attached to the rotor shaft to generate the rotor's field flux, resulting in an overall increase in axial length compared to conventional IPMSM[46]. Therefore, traction motors without Nd-PM are limited in achieving the same torque density compared to IPMSM.

Therefore, most of the traction motors of electric or hybrid vehicles currently on the market adopt PMSM containing Dy. As shown in Fig. 2.1, as the demand for eco-friendly vehicles increases, the supply risk of eco-friendly vehicle parts including Dy is expected to increase. Therefore, it is required to devise a way to overcome this.

In this chapter, we propose a Dy-free HPMM by extending the HPMM concept presented in Chapter 2. The target motor is a Toyota Prius 4th generation traction motor. As Dy-free Nd-PM of the proposed HPMM, Nd-PM of 21 kOe is applied. The proposed model implements the same torque and power density as the target motor, and achieves PM cost reduction and Dy-free.

4.2 TOYOTA PRIUS 4th MG2 Benchmark Study as Target Motor

4.2.1 Motor Disassembly Results and Main Specifications

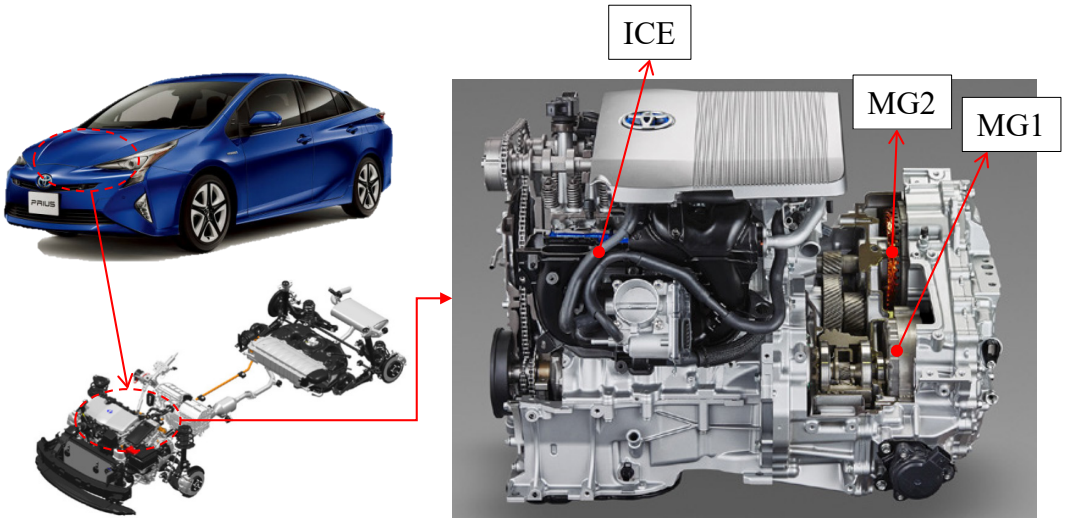

Fig. 4.6 TOYOTA PRIUS 4th Gen. powertrain

Table. 4.1 Specifications of TOYOTA PRIUS 4th Gen. HEV

Classification			Specification
Vehicle specification		Kerb weight	1,375 – 1,400 kg
		0-100kph	10.6sec
		Maximum speed	185kph
		CO2 emissions	70g/km
		Fuel efficiency	21.9km/ℓ
Powertrain performance	ICE	Output	72kW@5,200rpm
		Torque	140Nm@~3,600rpm
	MG1	Output	42kW (estimated)
		Torque	Not known
	MG2	Output	53kW
		Torque	163Nm

The target motor is the MG2 of Toyota PRIUS 4th generation HEV commercialized in 2016. The target car model is a series-parallel hybrid system and adopts a two-motor structure consisting of MG1 and MG2. MG1 is mainly driven by generating, and MG2 is driven mainly by motoring. Our research team purchased an actual vehicle, disassembled and analyzed the specifications of the powertrain module. Fig. 4.6 shows the 2016 TOYOTA PRIUS 4th Generation vehicle and powertrain module, and Table 4.1 is the vehicle specification.

Fig. 4.7 shows exploded view of TOYOTA PRIUS 4th Gen. electrical driven system. The structure of this system has a case cover at the front end and the end, and consists of a gear set and housing, MG1 and MG2 from the left. The MG1 mainly acts as a generator. That is, when brake pedaling, vehicle energy due to deceleration is recovered. And it plays a role in charging the battery by receiving mechanical rotational energy from the internal combustion engine according to the battery charge level. The MG2 mainly acts as a motor. When the vehicle is driven, the power of the engine is supported so that the internal combustion engine can be operated at an optimum efficiency point. Alternatively, when driving at low speed, pure EV driving is possible. The target motor in this chapter is MG2. Fig. 4.8 shows the actual stator assembly of the target motor. It is characterized by having a high fill factor by inserting a rectangular conductor into the stator core. Such a stator structure is usually called a hairpin stator. Eight conductors are inserted into the stator slots of the target motor. After 8 conductors are inserted, the jumper wire and lead wire of a specific shape are connected by welding. Therefore, as shown in Fig. 4.8, the end turn can be divided into an insertion part into which a rectangular conductor is inserted and a welding part connecting each conductor by welding. Each conductor in the weld zone loses the insulating effect as the conductor coating is melted by the high welding temperature. Therefore, an additional gray epoxy coating is applied as shown in the figure. Table 4.2 shows the stator specifications of the target motor. The outer and inner diameters of the stator core are 215 mm and 141.9 mm, respectively. The lamination length is 59.8 mm. The winding connection method is distributed winding. The number of slots is 48, and 8 conductors are connected in series per slot. The cross-sectional dimensions of each conductor are 3.56 mm wide and 2.16 mm long. This size includes the coating. The number of serial turns is 64 turns. The line-to-line resistance is 106 m ohms, and the total weight is 11.45 kg.

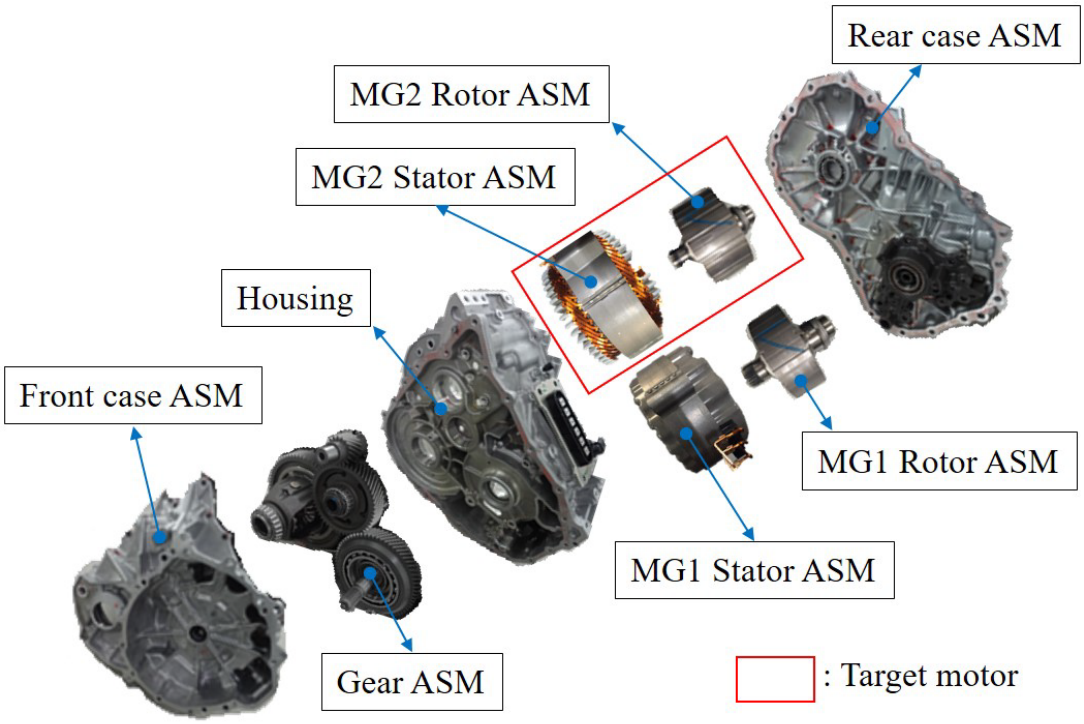

Fig. 4.7 Exploded view of TOYOTA PRIUS 4th Gen. electrical driven system.

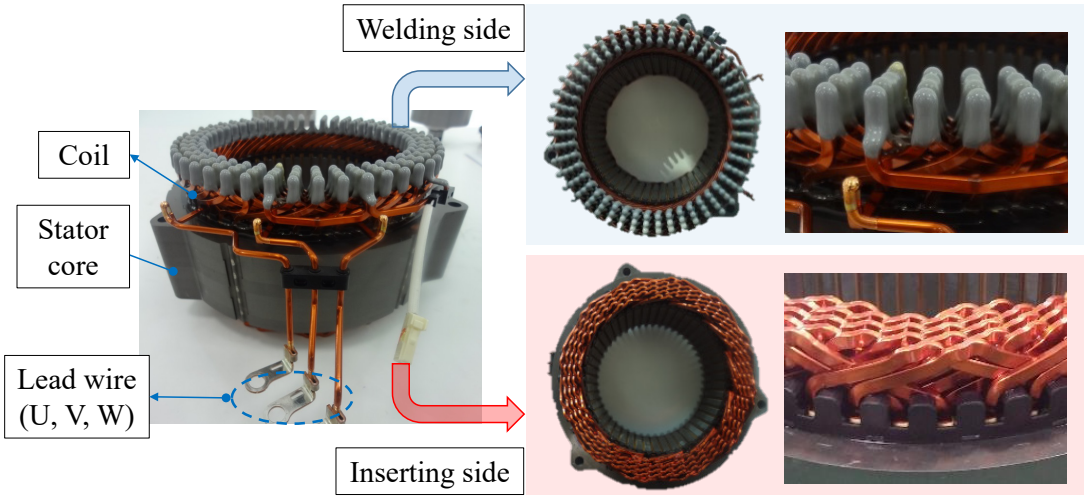

Fig. 4.8 Stator assembly of Target motor

Table. 4.2 Specifications of the stator assembly of the target motor

Outer diameter	215 mm
Inner diameter	141.9 mm
Stack length	59.8 mm
End-turn length (lead side/opposite side)	36 / 22.2 mm
Winding type	Distributed
Thickness of core plate	0.25 t
Rectangular wire (with coating)	2.16×3.56 mm
No. of slot	48
No. of layer per slot	8 layer
Series turns	64 turns
Line to line resistance	106 mΩ
Weight	11.45 kg

Fig. 4.9 is a simplified diagram of the wiring for one phase. The wiring pattern shows the concentric winding. The coil is wound around the pole span, and 8 turns are wound.

Fig. 4.10 shows the three-dimensional shape for the connection and each segment of the rectangular conductor composing the connection. According to the function of the rectangular conductor, it can be divided into standard wire, jumper wire, and special wire. The standard wire means the conductor inserted into the stator slot, and the line connecting these conductors is a jumper wire. After the standard wire and jumper wire are connected, connect the lead wire to enable electrical input. Also, connect the neutral wire to form a Y-connection between each phase.

Fig. 4.11 shows the cross-sectional shape of the target motor stator and its 2D shape. The slot opening is 3.7mm, the slot width is 4.61mm, and the yoke width is 15.75mm. Other detailed specifications are shown in Table 4.2.

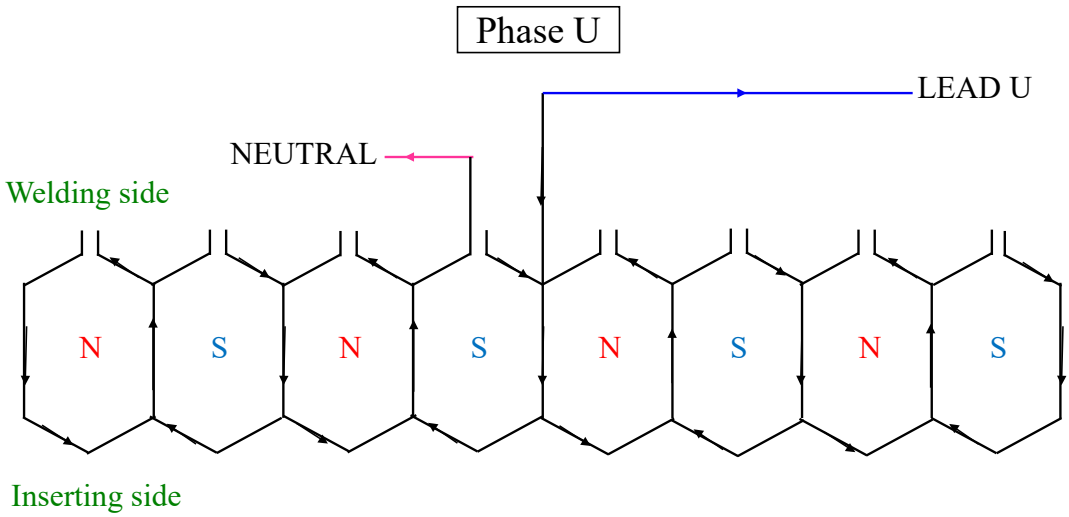

Fig. 4.9 Wiring diagram of stator ASM

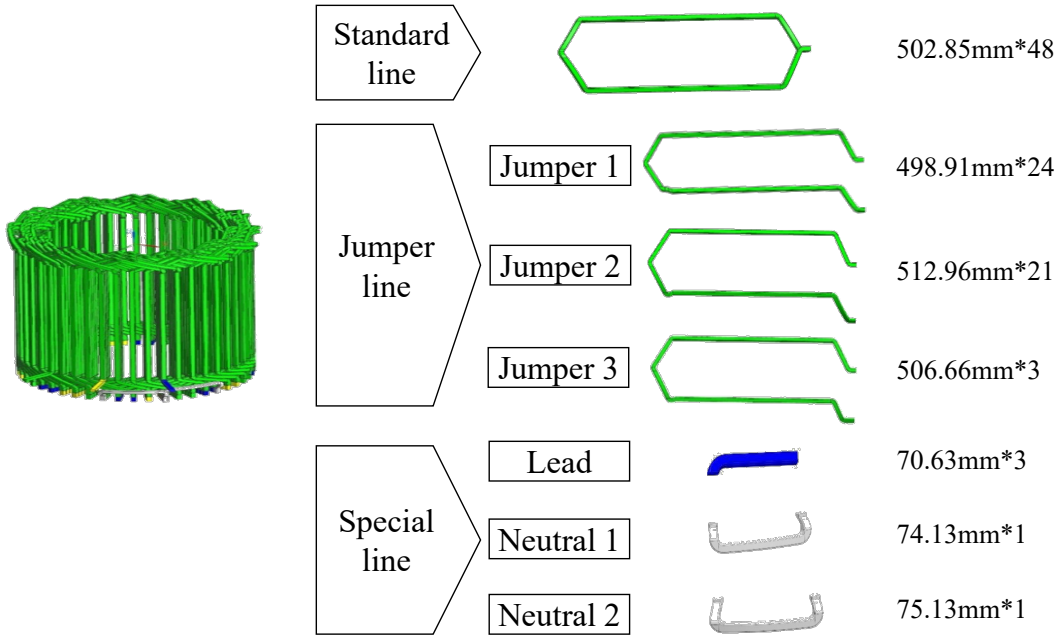

Fig. 4.10 Detailed parts and specifications related to wiring

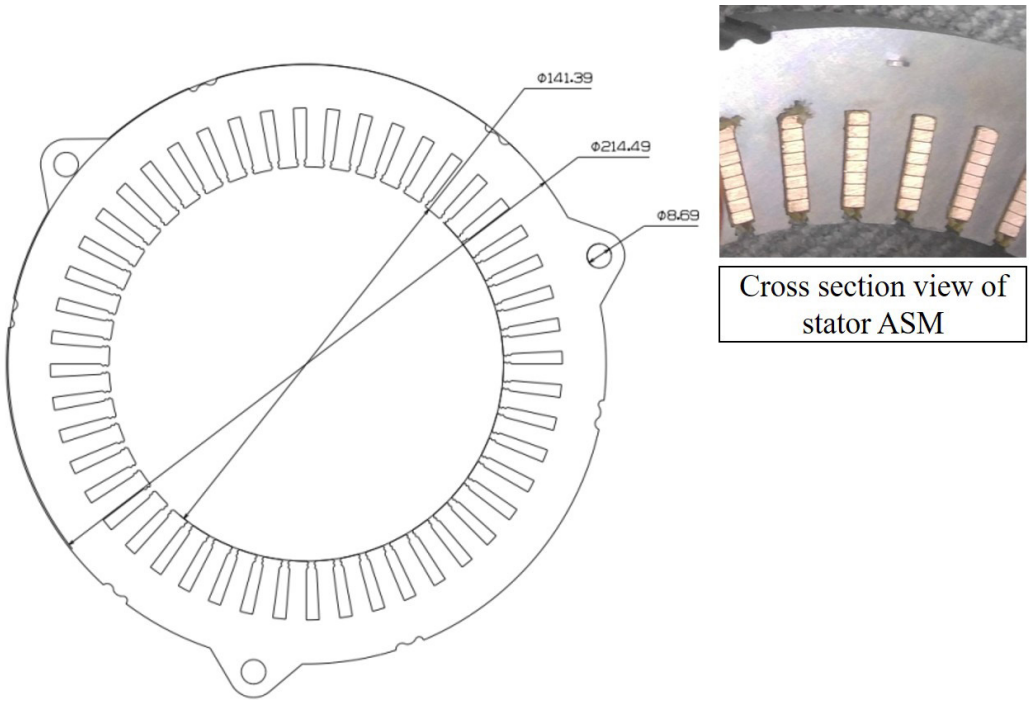

Fig. 4.11 2D model of stator core of target motor

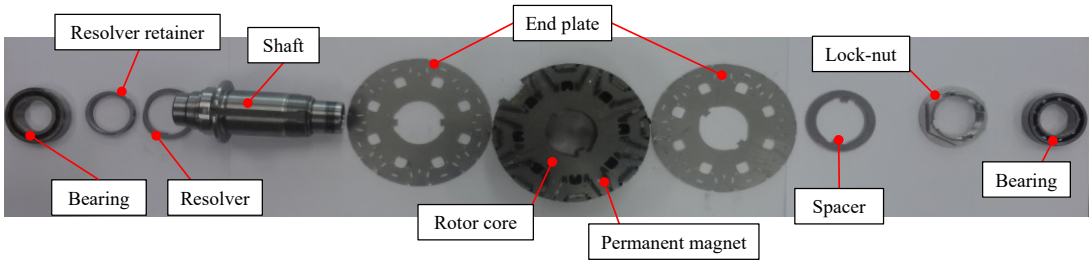

Fig. 4.12 Disassembly view of rotor

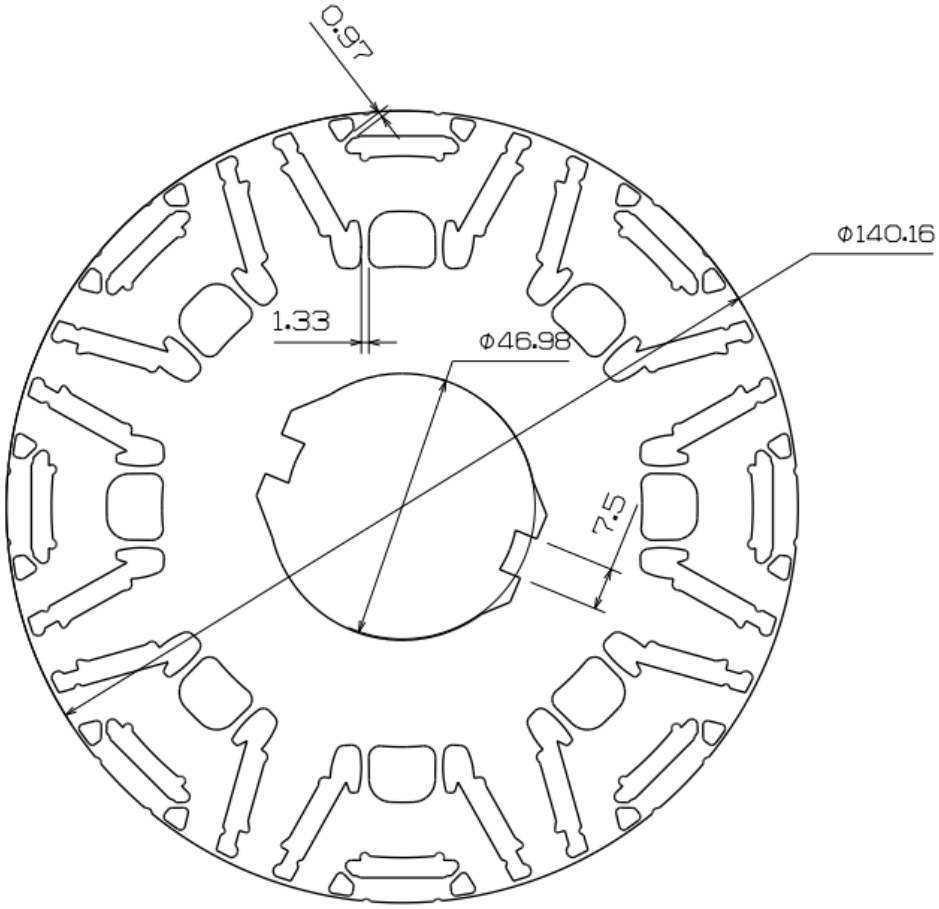

Fig. 4.13 2D model of rotor core of target motor

Fig. 4.12 is an exploded view of the rotor of the target motor. Among them, the 2D cross-sectional shape of the rotor core where the electromagnetic phenomenon occurs is shown in Fig. 4.13. Table 4.3 shows the main dimensions and detailed specifications. The number of poles of the target motor is 8, and the magnet is embedded in two layers to increase the reluctance torque. Each magnet is inserted two per rotor core slot. That is, 6 pieces of magnets are inserted per pole, thereby reducing the magnet cost and eddy current loss. Epoxy resin is filled between the magnet and the rotor core slot. As a result, the magnet is held firmly inside the rotor core slot. The total usage of the magnet is 0.564 kg.

Table. 4.3 Specifications of the rotor assembly of the target motor

Outer diameter	140.44 mm
Inner diameter	48 mm
Stack length	60 mm
No. of poles	8
Skew	N/A
Thickness of core plate	0.25 t
Air-gap	0.73mm
PM size (V type)	T3.5×W7.47×L59.1
Stacking method	Inter-lock
PM weight	0.564kg
Total weight	6.18 kg

4.2.2 Results of analysis of Nd-PM constituent elements and magnetic properties

Fig. 4.14 to Fig. 4.17 are data analyzed on the magnetic properties, particle size, and constituent elements of MG2's magnet commissioned by an external professional company. Fig. 4.14 (a) shows the actual shape of the specimen. Fig. 4.14 (b) shows the magnetic properties according to the measurement position of the specimen. The coercive force of MG2 was measured from 1,749 kA/m to 1,753 kA/m depending on the measurement location. When unit conversion is performed, it is 22kOe to 23kOe, and when the error of measuring equipment is taken into consideration, it is actually estimated to be 24 to 25kOe. With the same logic, the residual magnetic flux density is estimated to be about 1.38 to 1.4. Fig. 4.15 shows the results of measuring the BH characteristics of the specimen.

(a)

NO.	Br (T)	Hcb (kA/m)	Hcj (kA/m)	(BH)max (kJ/m^3)	Hk (kA/m)	Hk/Hcj	测量设备	人员设备
MG2-中心-20℃	1.368	1032.0	1749	354.5	1514	0.87	强脉冲	张骞
MG2-中心-120℃	1.217	685.6	738	276.6	672	0.91	MPS	
MG2-中心-140℃	1.177	555.8	596	255.8	539	0.90		
MG2-中心-160℃	1.135	442.4	472	233.0	421	0.89		
MG2-边缘-20℃	1.372	1033.0	1753	355.7	1522	0.87	强脉冲	张骞
MG2-边缘-120℃	1.211	681.0	762	274.2	666	0.87	MPS	
MG2-边缘-140℃	1.173	556.9	619	254.8	531	0.86		
MG2-边缘-160℃	1.125	443.7	490	228.7	412	0.84		

(b)

Fig. 4.14 MG2 magnet (a) The shape of the specimen requested for measurement (b) Mag netic properties according to the measurement location

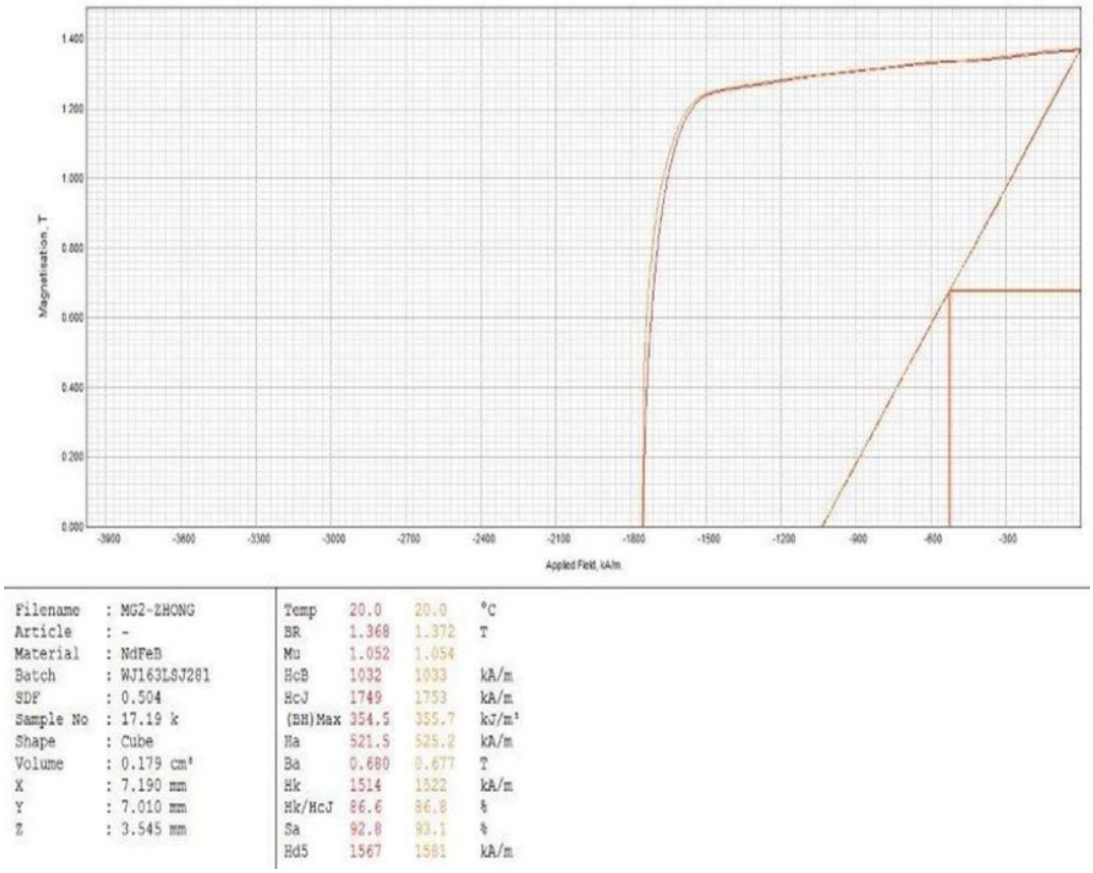

Fig. 4.15 *BH* Characteristics of MG2 magnet

Fig. 4.16 shows the particle size of the specimen at 1,000 magnifications. The number of particles on the measurement image is 541, and the average particle size is estimated to be 5.33 micrometers.

Fig. 4.17 shows the main constituent elements of the specimen. The elements related to the coercive force of Nd-PM are Dy and Tb. The measured specimen contains Dy and 1.24% to 1.44%. And, Tb is not contained. When Dy is removed, the magnet's coercive force is lowered. As a result, the demagnetization durability of the magnet deteriorates. As mentioned earlier, Dy is a high-risk material in the supply chain. Therefore, it is necessary to study a rotor topology that is based on Dy-free Nd-PM, has excellent demagnetization durability, and can realize the same torque density and power density.

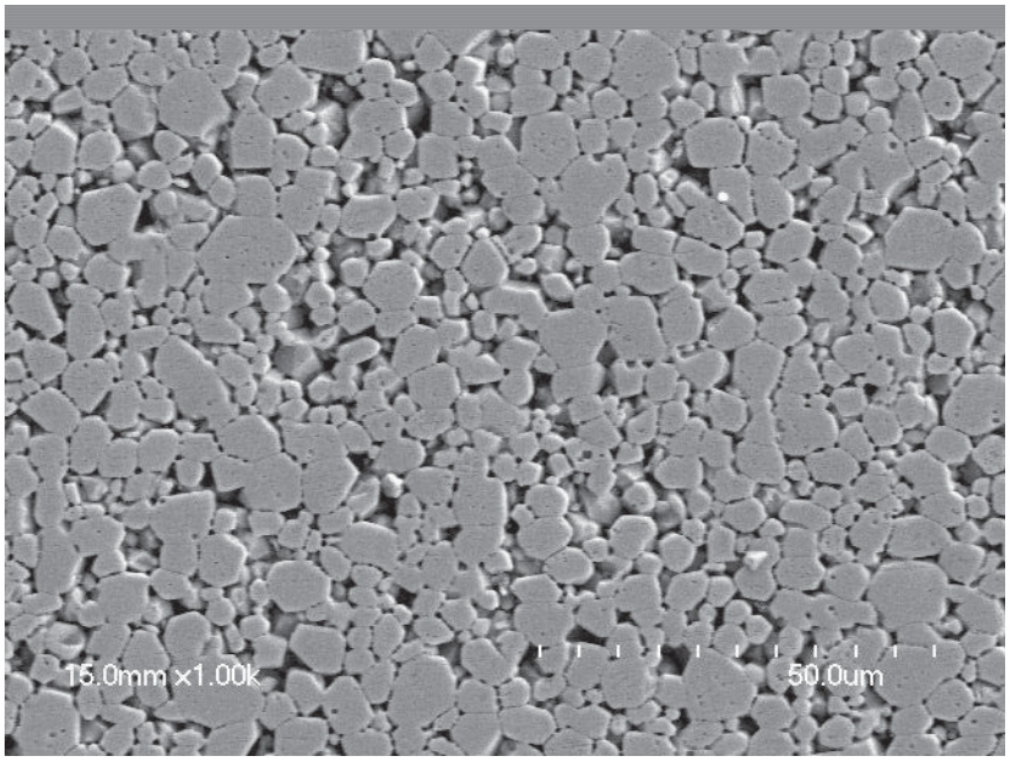

1000×磁体金相照片

Fig. 4.16 Particle size of the specimen at 1000 magnification

检测数据（%）															
产品尺寸	牌号	B	Al	Co	Ti	Cu	Ga	Zr	Nb	RE	Pr	Nd	Dy	Ho	Tb
59.2-7.25-3.45MG2 中心	-	0.951	0.29	1.98	\	0.10	0.09	0.04	\	29.49	6.17	22.08	1.24	\	\
59.2-7.25-3.45MG2 边角	-	0.953	0.29	1.96	\	0.10	0.10	0.04	\	29.45	6.16	21.85	1.44	\	\
		Gd	Si	C	S	O	N								
59.2-7.25-3.45MG2 中心	-	\	0.06	0.0908	0.0013	0.0553	0.0676								
59.2-7.25-3.45MG2 边角	-	\	0.05	--	--	--	--								

Fig. 4.17 The main constituents of the specimen

4.2.3 Comparison between Back-EMF Measurements and 2D model FEA Results to improve Analysis Accuracy

After assembling the stator assembly and rotor assembly of the target motor by manufacturing a simple housing for measuring Back-EMF, the test equipment was configured as shown in Fig. 4.18(a). Fig. 4.18(b) shows the back EMF measurement result at 743 rpm. The measured back EMF value is 29.7 Vrms.

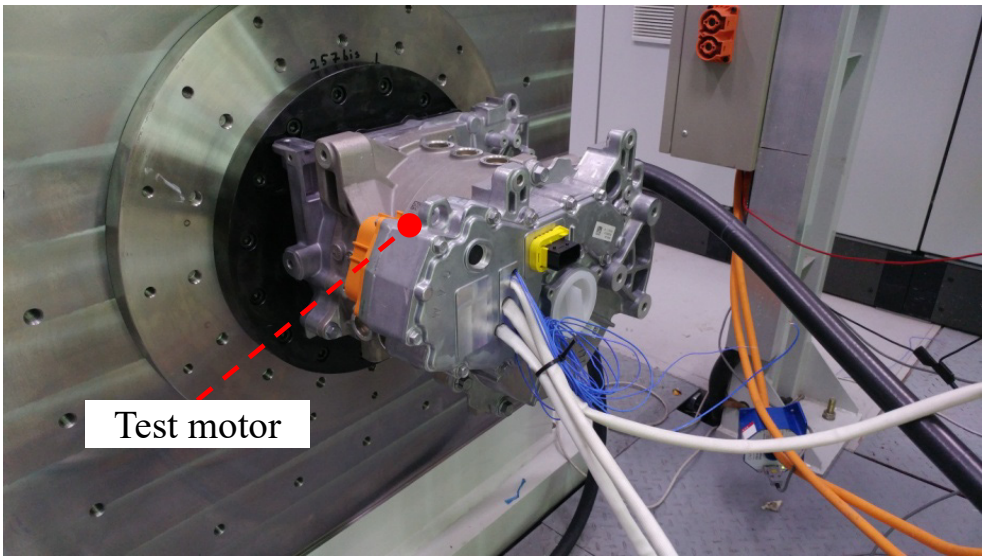

(a)

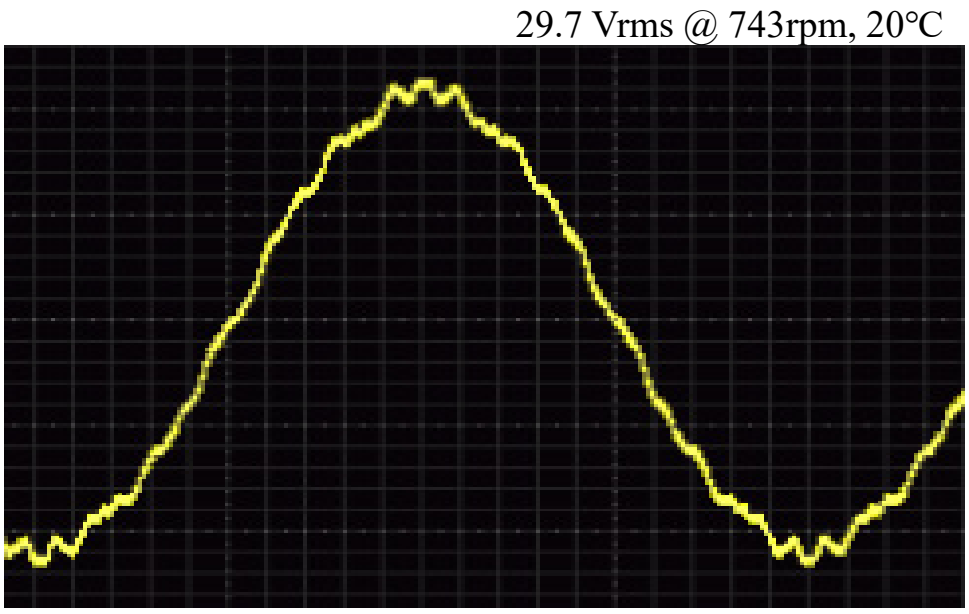

Fig. 4.18 Back-EMF measurement (a) test facility (b) measurement results

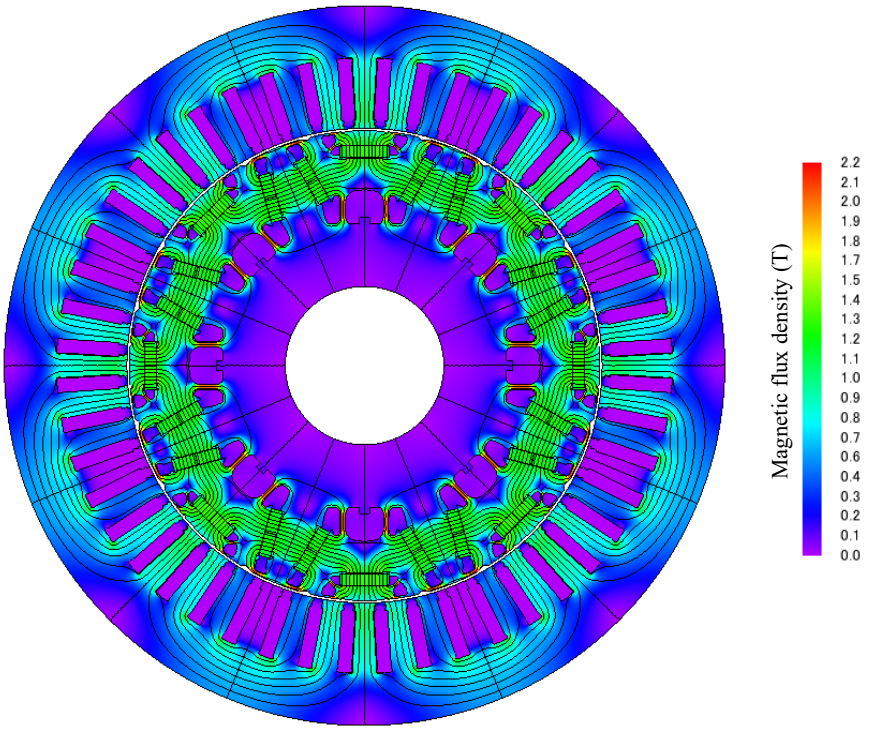

(a)

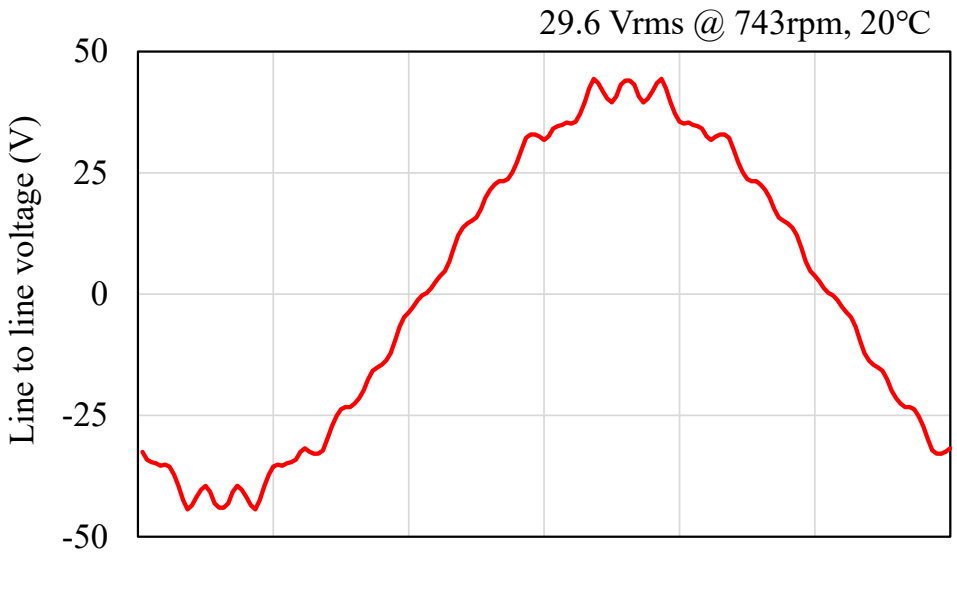

(b)

Fig. 4.19 No-load analysis results (a) flux density distribution (b) Back-EMF

Fig. 4.19 (a) is the flux density distribution at no load of the 2D model of Fig. 4.11 and Fig. 4.13. At this time, 27PNX1350F (posco Co. Ltd.) was applied for the electrical steel sheet. Fig. 4.18 (b) is the back-EMF waveform. And for the residual magnetic flux density of the magnet, 1.37 T was applied at room temperature. In order to be similar to the actual measurement result of Fig. 4.18 (b), the stacking factor was partially adjusted in the 2D analysis model. The back electromotive force analysis result is 29.6Vrms at 743 rpm. The error rate compared to the measured value of 29.7Vrms is 0.3%.

Under the same analysis conditions, the maximum torque is 181 Nm at PM temperature of 100 ℃ and an input current of 180 Arms. The maximum torque of MG2 is known to be 163Nm, but the input current value for generating 163Nm is unknown [91]. Therefore, in this paper, the target torque value was set to 181Nm based on 180Arms. This means that the torque density per unit current is 1 Nm/Arms. Fig. 4.20 shows the torque waveform at the maximum torque point. Table 4.4 shows the comparison results for back-EMF and peak torque. The proposed HPMM models to be presented in the next chapter were also reviewed under the same analysis conditions as the target motor.

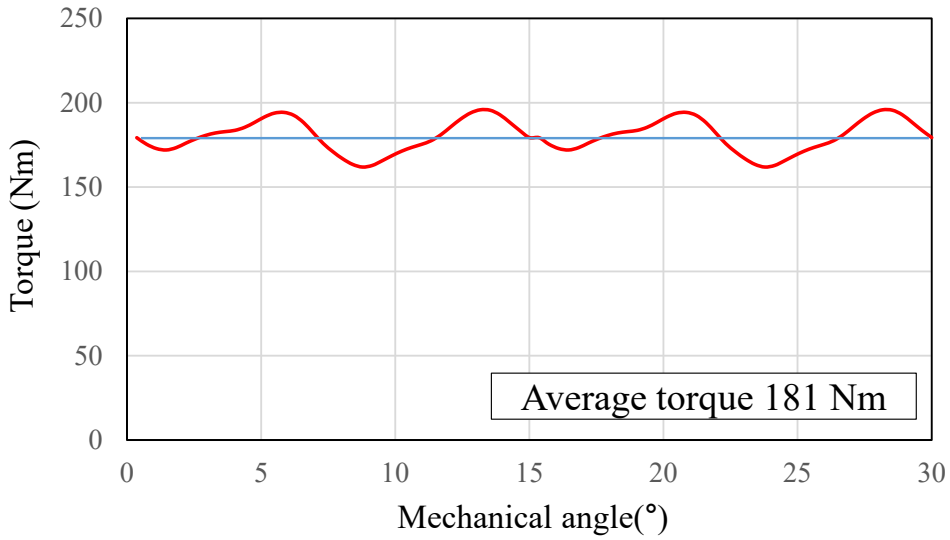

Fig. 4.20 Torque analysis results of target motor (Input current 456Arms, PM temperature 100℃, control angle 45°)

Table. 4.4 Comparisons of Back-EMF and peak torque

Classification	Back-EMF @1,000rpm	Peak torque
2D-FEA result	29.7 Vrms	181 Nm (target torque)
Measurement and Catalog value	29.6 Vrms	Not known
Error ratio	0.2 %	

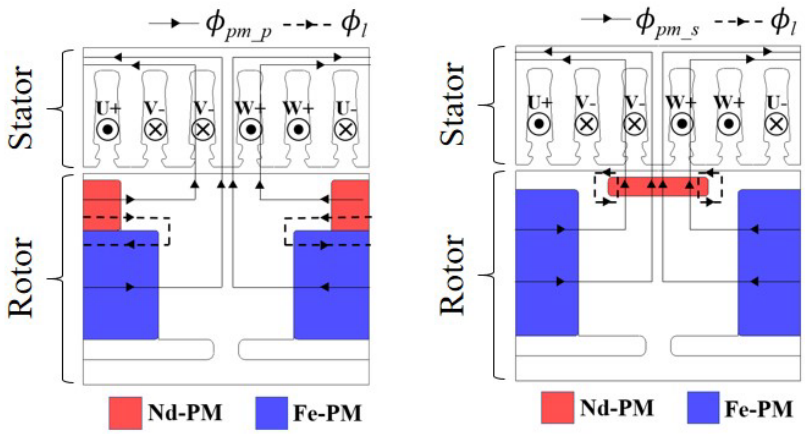

Fig. 4.21 Magnetic flux path of basic models (a) P-HPMM (b) S-HPMM.

4.3 Proposal of Dy-free Hybrid PM Motor of Parallel and Series Type

As mentioned earlier, Nd-PM can achieve a coercivity of up to 21 kOe without dysprosium due to the development of manufacturing technology. However, due to the high-temperature operation characteristics of vehicle traction motors, Nd-PM over 25kOe is mainly applied. In this chapter, 21kOe Nd-PM and 5.5kOe Fe-PM are simultaneously applied, and a HPMM suitable for environmental temperature conditions of vehicle traction motors is proposed. HPMM is divided into serial configuration and parallel configuration according to the arrangement of each PM. This paper compares the pros and cons of each configuration and presents rotor structures that can

improve demagnetization durability and torque characteristics. After comparing the performance characteristics of each rotor structure through 2D-FEM, finally, an HPMM suitable for vehicle traction motors is proposed. Also, the proposed HPMM shows the same torque and power density as the traction motor of TOYOTA PRIUS 4th-generation HEV, the target motor. At the same time, the proposed HPMM reduced the usage of Nd-PM by 47 % and the total PM cost by 10% compared to the target motor.

4.3.1 Design Concept and Proposed Model of Parallel and Series hybrid PM motor

As shown in Fig. 4.21(a) and (b), the basic model of HPMM can be divided into S-HPMM and P-HPMM according to the arrangement of each magnet. The magnetic equivalent circuit is shown in Fig. 2.6. Also, the mathematical model of PM flux linkage of each topology and its comparison results are mentioned in Section 3.1.4.

As explained in Chapter 3, the P-HPMM can achieve higher PM flux linkage than the S-HPMM, which is advantageous for improving the PM torque component. However, since the traction motor operates at high speed through flux-weakening control, the reverse magnetic field of the d-axis is excited from the stator. The P-HPMM is disadvantageous in terms of demagnetization durability because a high d-axis reverse magnetic field is applied in a direction in which the reluctance of PM is small due to the characteristics of the parallel circuit. Also, if the thickness of Fe-PM is small, demagnetization of Fe-PM is generated by the leakage flux of Nd-PM. By contrast, the S-HPMM has an advantage over the P-HPMM in terms of demagnetization durability because each PM flux linkage is interlinked. However, due to the high d-axis reluctance, the PM

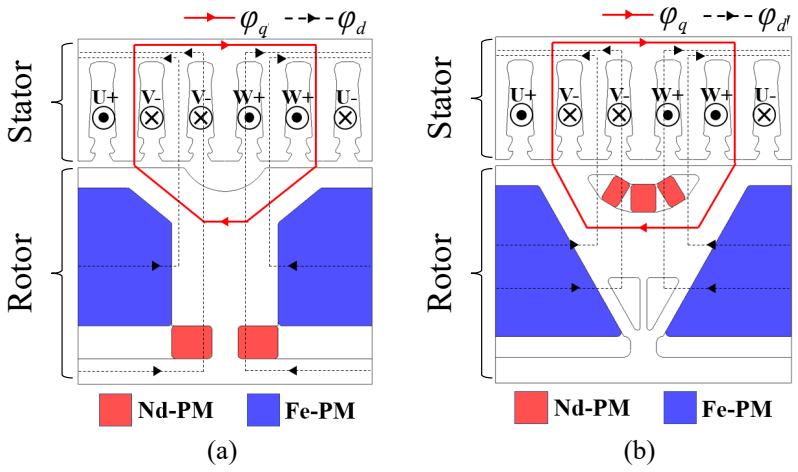

Fig. 4.22 Proposed design concepts (a) P-HPMM (b) S-HPMM.

torque component is lower than that of the P-HPMM, which is disadvantageous in terms of torque density. Therefore, in this chapter, we propose a new design concept for the P-HPMM and S-HPMM as shown in Fig. 4.22(a) and (b).

In the proposed P-HPMM, in order to improve demagnetization durability, Nd-PM is placed on the inner diameter side of the rotor and a flux barrier is applied on the surface of the rotor core in the d-axis direction. Also, since the T_{pm} decreases due to the increase in *d*-axis reluctance, it increases the T_{re} by expanding the *q*-axis flux path. In other words, the L_d decreases, but the L_q increases, so the saliency ratio (L_d−L_q) increases. The proposed S-HPMM applies trapezoidal Fe-PM and U shape Nd-PM to improve the T_{re} by expanding the *q*-axis flux path and increasing the *d*-axis reluctance. In addition, a flux barrier is applied to the lower part of the rotor core to reduce the leakage flux of Fe-PM.

To verify the effectiveness of the proposed models, 4 models are presented as shown in Fig. 4.23. Fig. 4.23(a) and (b) are the P-HPMM with Nd-PM applied to the inside of the rotor and the proposed P-HPMM. Fig. 4.23(c) and (d) are the S-HPMM with the bar type Fe-PM and the proposed S-HPMM. The stator structure of all 4 models is the same as that of the target motor, and have the same usage of Fe-PM and Nd-PM. Also, the thickness of Nd-PM is 6.5mm, which is the same for all. The material of the rotor core is applied high-tensile electrical steel sheet with a yield strength of 700 MPa to maintain rotational stiffness at the maximum speed.

4.3.2 Comparison of main specifications

The target motor is the traction motor of TOYOTA PRIUS 4th-generation HEV commercialized in 2015. Table 4.5 is the detailed specifications of the target motor and the proposed HPMM. The number of stator slots of the target motor is 48, and it is a distributed winding. The rotor has an 8-pole structure. Each model has the same stator structure and overall volume. As each magnet material for analysis, Nd-PM is N42SH-R (21kOe, ShinEtsu Co., Ltd.), and Fe-PM is NMF-15J (5.5kOe, Hitachi metals Co., Ltd.).

The Nd-PM usage of the proposed HPMMs is 53% of the target motor. Assuming that the cost of Fe-PM is 1/10 of that of Nd-PM, the total PM cost of the proposed HPMMs is 90% of the target motor. Under the same operating conditions, the performance of each models was predicted through FEA tools. JMAG-Designer and Solidworks.

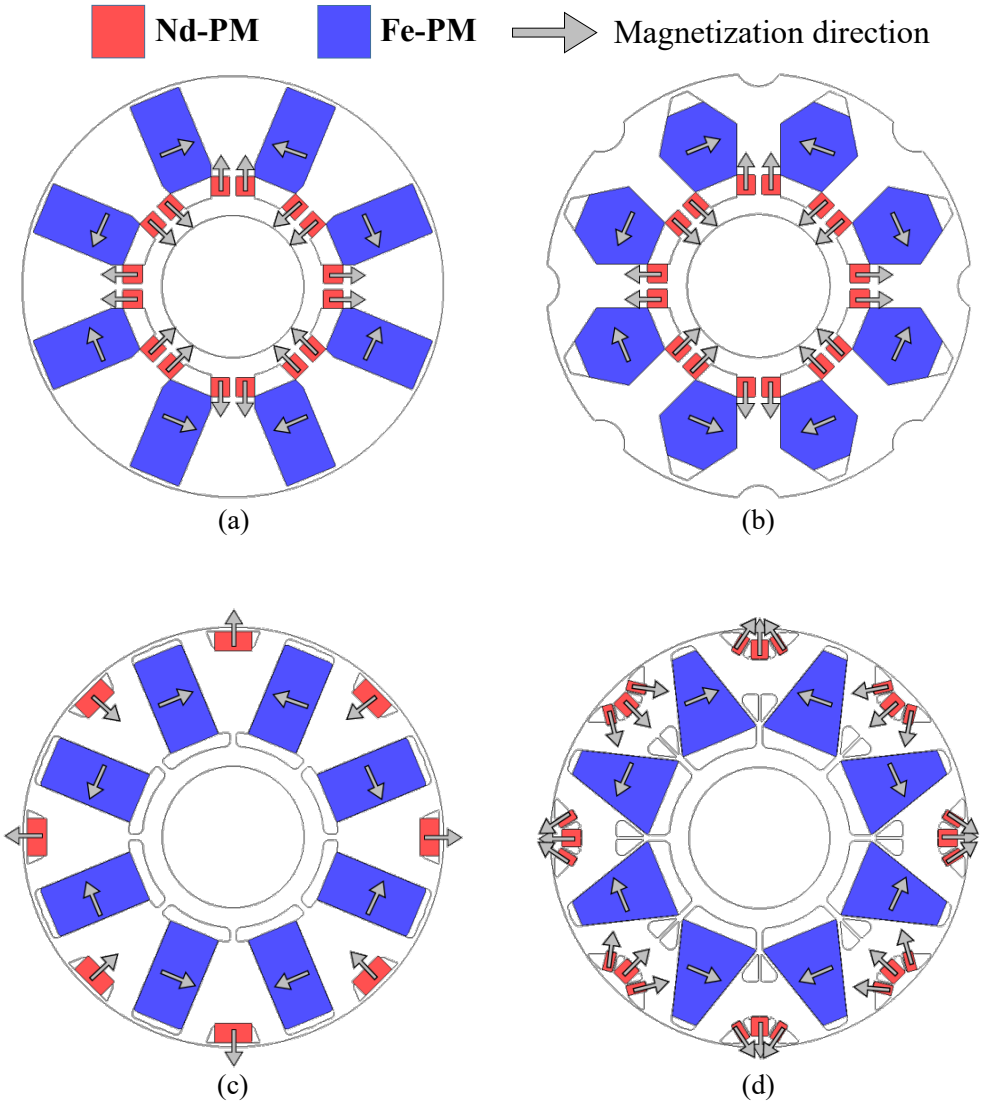

Fig. 4.23 Proposed models (a) P-HPMM-Model-A (b) P-HPMM-Model-B (c) S-HP MM-Model-A (d) S-HPMM-Model-B.

Table. 4.5 Specification of each IPMSMs

Item		Unit	Target IPMSM	Proposed HPMM
DC-link voltage		Vdc	600	600
Maximum current		Arms	180	180
Stator outer diameter		mm	215	215
Stator inner diameter		mm	141.82	141.82
Air-gap length		mm	0.725	0.725
Rotor outer diameter		mm	140.37	140.37
Rotor inner diameter		mm	47.3	47.3
Stack length		mm	60	60
Number of pole / slot		-	8 / 48	8 / 48
Series turns per phase		-	64	64
Electrical steel sheet	Stator	-	35A210	35A210
	Rotor	-	35A210	35PNT650Y
Magnet grade	Fe-PM	-	1.37 T	N42SH-R
	Nd-PM	-	-	NMF-15J
Volume of Nd-PM		mm^3	72,336 (100%)	38,585 (53%)
Volume of Fe-PM		mm^3	-	265,024
Total PM cost[d]		%	100	90

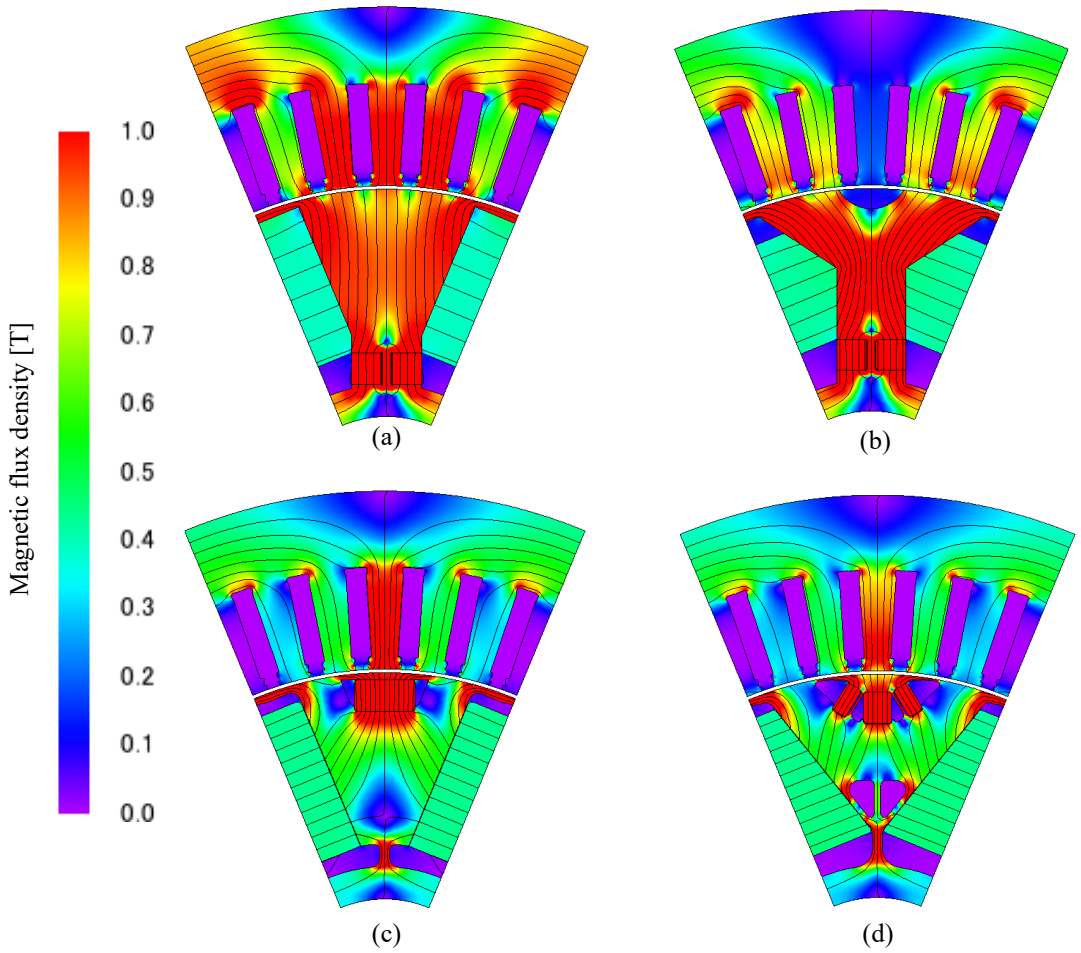

Fig. 4.24 Flux density distribution under no-load condition (a) P-HPMM-Model-A (b) P-HPMM-Model-B (c) S-HPMM-Model-A (d) S-HPMM-Model-B.

4.4 Comparison of performance characteristics between each proposed model

4.4.1 Magnetic Flux Density Distribution under No Load and Load Condition

Fig. 4.24 shows the flux density distribution for each model under no-load condition. P-HPMM has a higher magnetic flux density in the rotor core than S-SHPMM because the flux linkage of each magnet is concentrated in the *d*-axis direction. On the other hand, in S-HPMM, the flux linkage of each magnet is linked to each other. Since the *d*-axis reluctance is high, the magnetic flux density in the rotor core is lower than that of the P-HPMM.

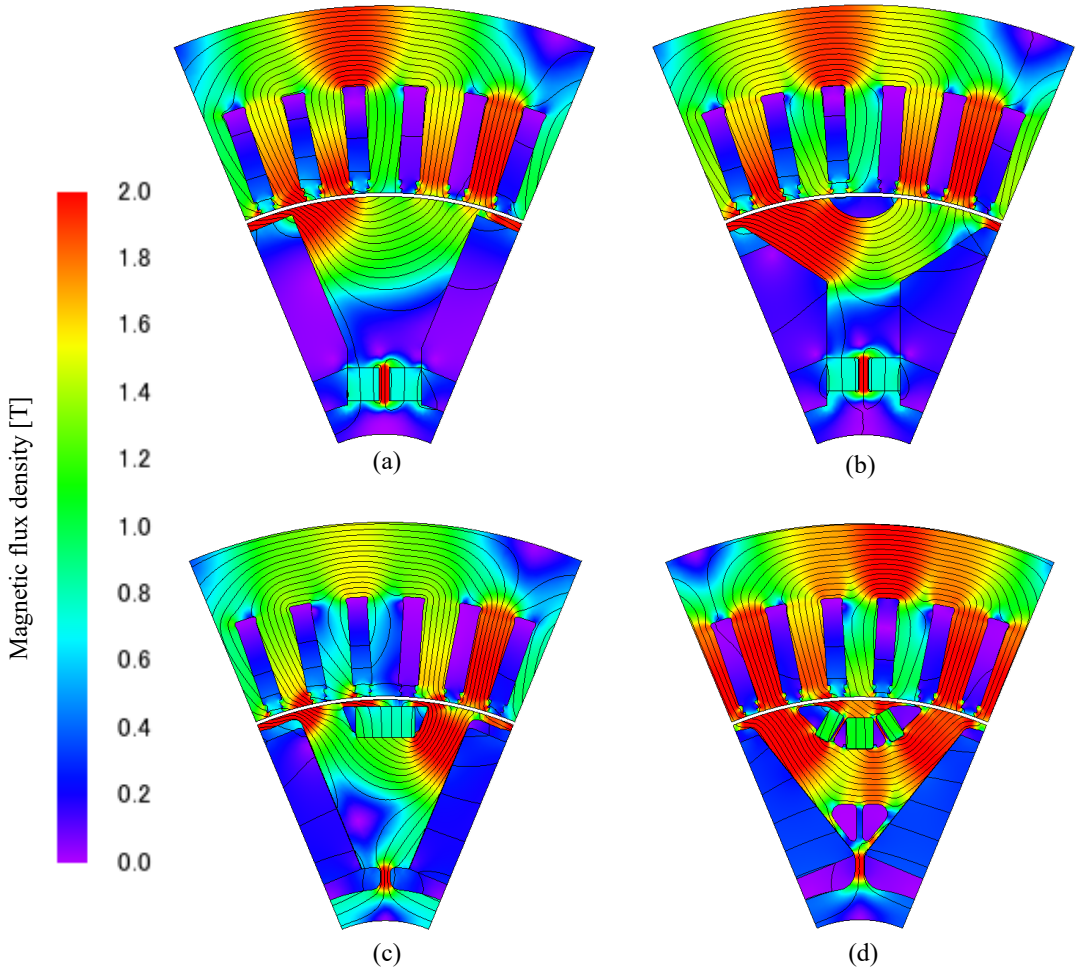

Fig. 4.25 Flux density distribution under load condition (a) P-HPMM-Model-A (b) P-HPMM-Model-B (c) S-HPMM-Model-A (d) S-HPMM-Model-B.

Fig. 4.25 shows the flux density distribution for each model under the maximum torque load condition. The flux linkage of each HPMM is mainly generated through the *q*-axis flux path. In particular, S-HPMM-Model-B has higher magnetic flux density in all areas of the rotor core compared to other models.

4.4.2 Irreversible Demagnetization

Fig. 4.26 and 4.27 show the back-EMF waveform before and after applying the demagnetization current at −40 ℃ and the flux density distribution of each magnet. The demagnetization current means applying a maximum current of 180Arms only in the *d*-axis

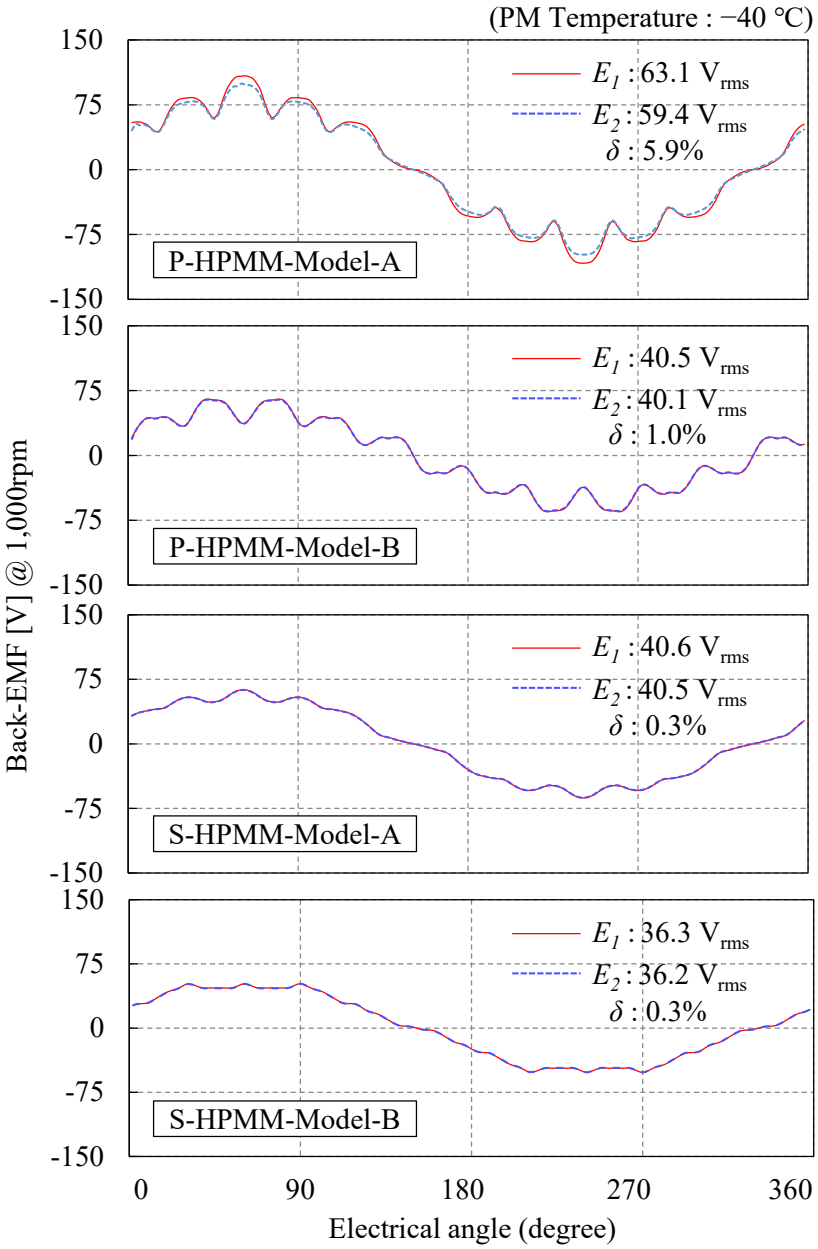

Fig. 4.26 Back-EMF waveform before and after applying the demagnetization curve at 180A at the PM temperature −40 °C.

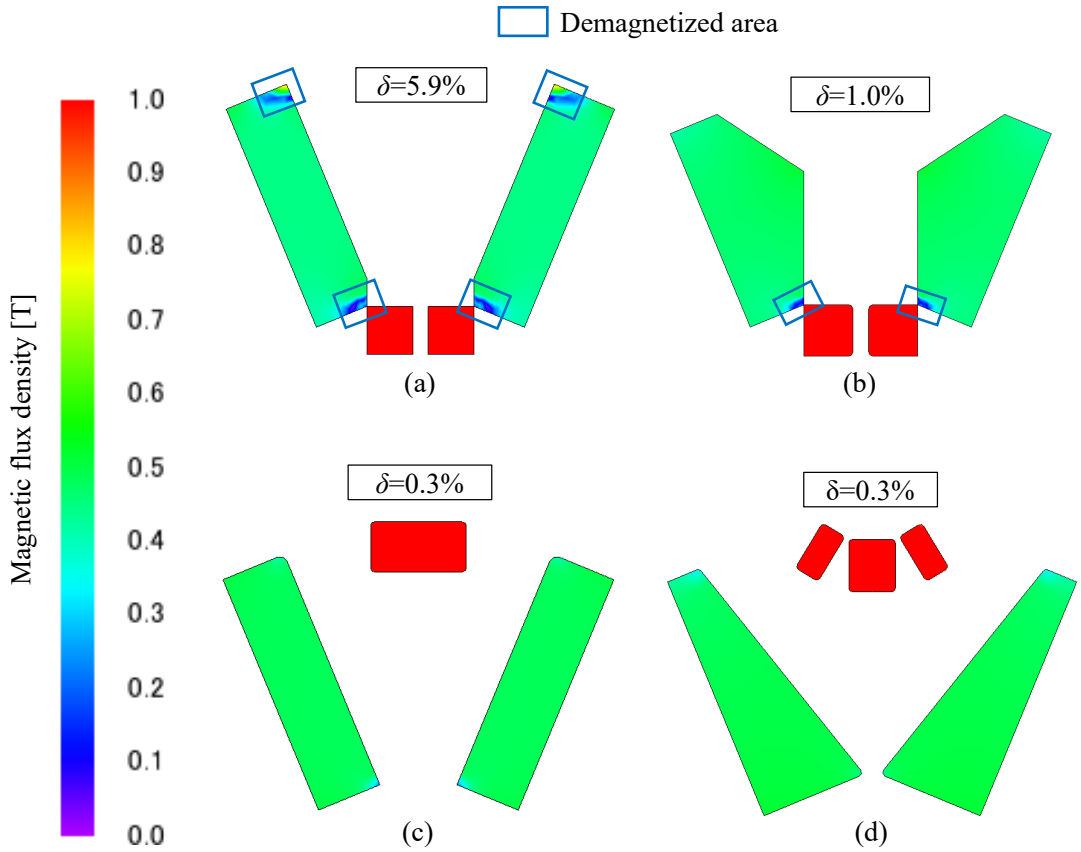

Fig. 4.27 Flux density distribution after applying demagnetization current 180A at t he PM temperature −40 °C (a) P-HPMM-Model-A (b) P-HPMM-Model-B (c) S-HPM M-Model-A (d) S-HPMM-Model-B.

direction. The demagnetization rate δ can be expressed as (3.4.6.1).

In Fig. 4.27(a) and (b), the P-HPMM-Model-A mainly has a low-temperature demagnetization in Fe-PM, and δ is 5.9 %. δ of P-HPMM-Model-B is 1.0 %, which is 4.9 % improved compared to the P-HPMM-Model-A. In Fig. 4.27(c) and (d), δ of the S-HPMM-Model-A and -B is 0.3 % respectively.

Fig. 4.28 and 4.29 show the back-EMF waveform before and after applying the demagnetization current at 180 °C and the flux density distribution of each magnet. In Fig. 4.29(a) and (b), Nd-PM of P-HPMM-Model-A is mostly demagnetized, and δ is 31.0 %. δ of P-HPMM-Model-B is 2.2 %, which is 28.8 % improved compared to the P-HPMM-Model-A. In Fig. 4.29(c) and (d), δ of the S-HPMM-Model-A and -B is 2.9 % respectively.

Therefore, P-HPMM has improved demagnetization durability at −40 °C and 180 °C through the proposed design concept. In addition, it can be seen that S-HPMM is basically advantageous in terms of demagnetization durability compared to P-HPMM.

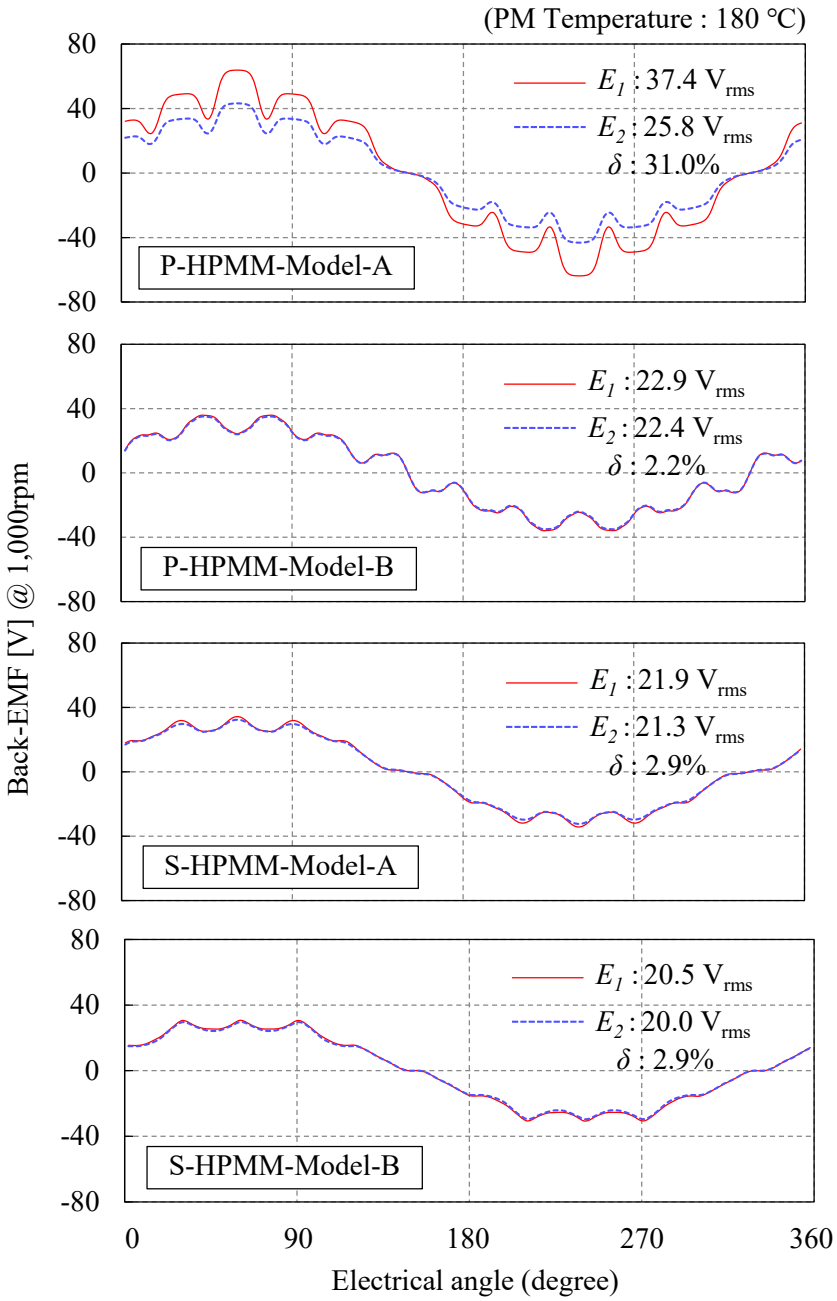

Fig. 4.28 Back-EMF waveform before and after applying the demagnetization current 180A at the PM temperature 180 °C.

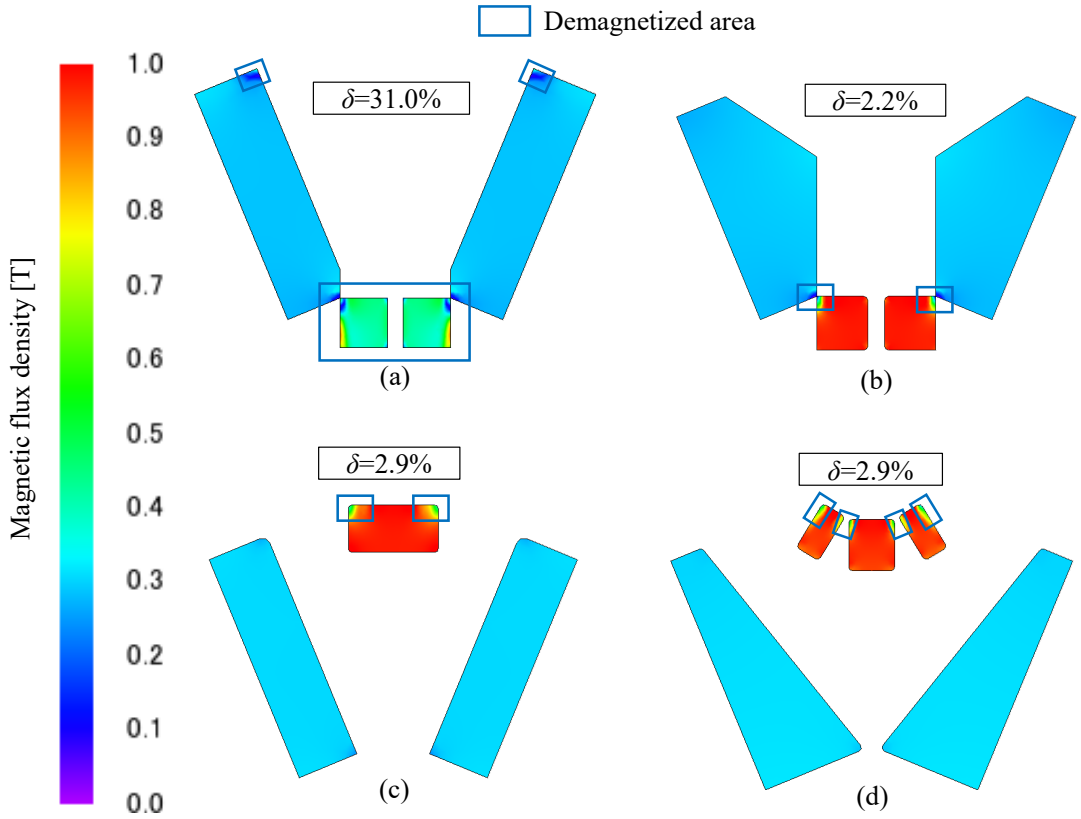

Fig. 4.29 Flux density distribution after applying demagnetization current 180A at the PM temperature 180 °C (a) P-HPMM-Model-A (b) P-HPMM-Model-B (c) S-HPMM-Model-A (d) S-HPMM-Model-B.

4.4.3 Inductance

Fig. 4.30 shows the L_d and L_q of each HPMM for each input current and phase angle. As shown in Fig. 4.30(a), Model-B of each HPMM has lower L_d than Model-A. The reason is that the flux barrier on the *d*-axis flux path is applied in the P-HPMM-Model-B, and the Nd-PM is inserted in the U shape in the S-HPMM-Model-B.

As shown in Fig. 4.30(b), Model-B of each HPMM has higher L_q than Model-A. P-HPMM-Model-B is because the *q*-axis magnetic flux path under the flux barrier is expanded, and S-HPMM-Model-B is because the *q*-axis magnetic flux path is expanded by applying trapezoidal Fe-PM.

Therefore, since each HPMM's Model-B has a large saliency ratio (L_d–L_q), it can be expected that the reluctance torque increases compared to each HPMM's Model-A.

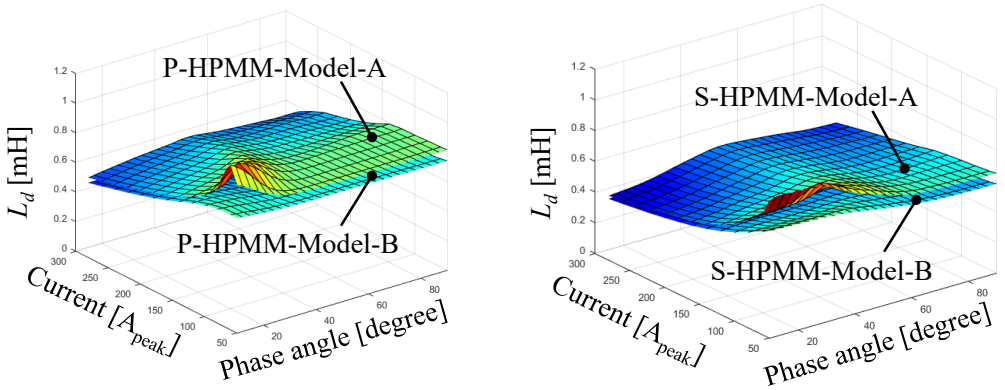

(a)

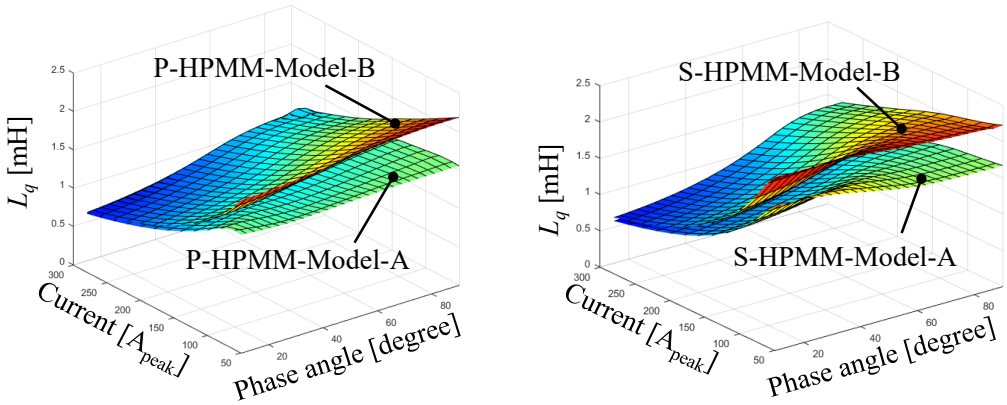

(b)

Fig. 4.30 Inductance by current and phase angle (a) *d*-axis inductance L_d (b) *q*-axis inductance L_q.

4.4.4 Average Torque by Current Phase Angle

Fig. 4.31 is the average torque by current phase angle. The input current is 180Arms and the coil and PM temperature are based on 100 ℃. In Fig. 4.31(a), the torque at a current phase angle of 0 degrees related to PM torque is 110 Nm for P-HPMM-Model-A and 76 Nm for P-HPMM-Model-B. Model-B is 34 Nm lower than Model-A because the flux barrier is applied on the *d*-axis flux path to improve demagnetization durability. The maximum torque is 157 Nm for Model-A and 152 Nm for Model-B, which are similar to each other. The reason is that, as in Fig. 4.30, Model-B has a higher saliency ratio (L_d–L_q) than Model-A, and the reluctance torque is increased. However, both models of P- HPMM do not meet the maximum torque of 181 Nm of the target motor.

In Fig. 4.31(b), The torque at a current phase angle of 0 degrees related to PM torque is 92 Nm

for S-HPMM-Model-A and 81 Nm for S-HPMM-Model-B. In Model-B, since Nd-PM is inserted in U-shape to improve reluctance torque, *d*-axis reluctance is increased, which is 11 Nm lower than Model-A. The maximum torque is 150 Nm for Model-A, 181 Nm for Model-B. The reason is that Model-B applies trapezoidal Fe-PM, and the *q*-axis flux path is expanded compared to

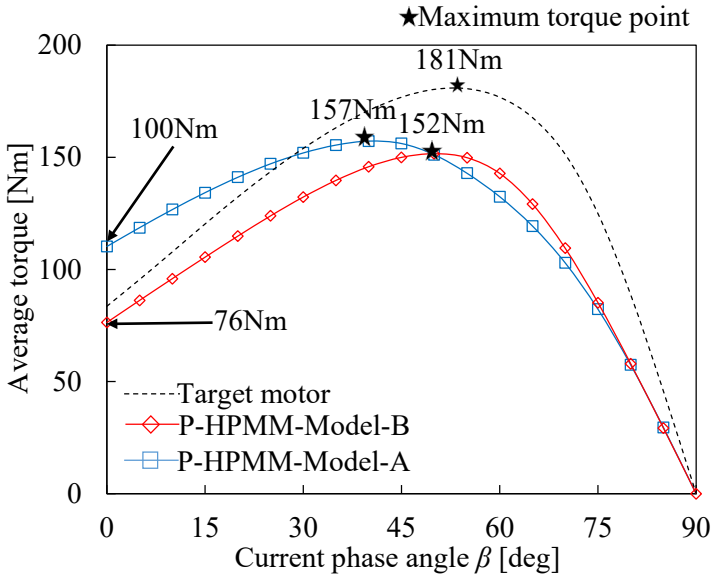

(a)

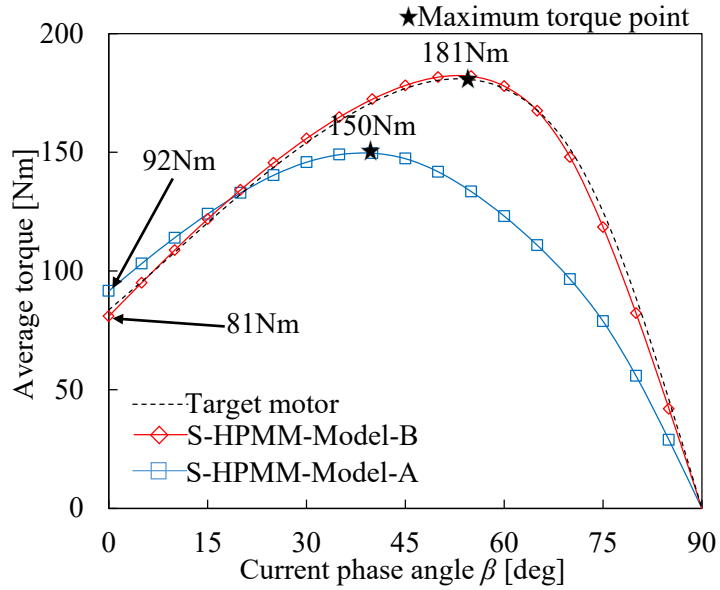

(b)

Fig. 4.31 Average torque by current phase angle (Input current : 180Arms) (a) P-H PMM (b) S-HPMM.

Model-A. As shown in Fig. 30, this is because the saliency ratio (L_d–L_q) is higher than that of Model-A, and the reluctance torque is greatly increased. In addition, Model-B satisfies the maximum torque of 181 Nm of the target motor.

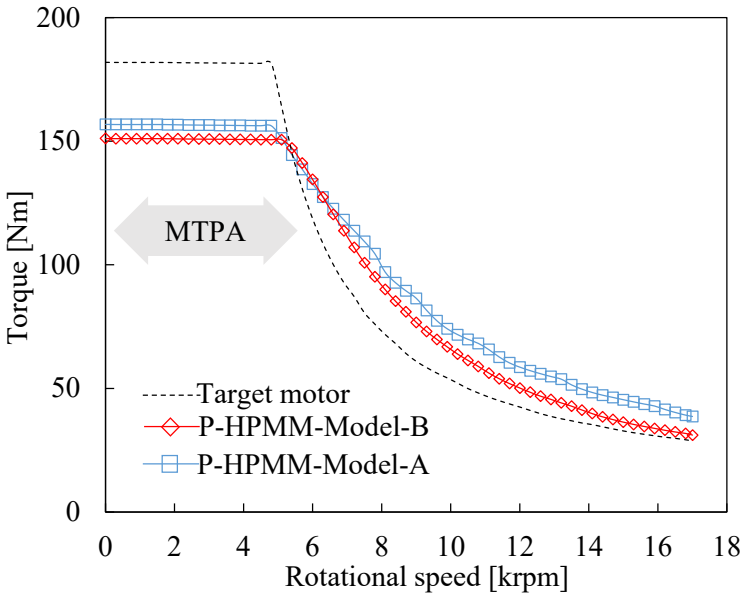

(a)

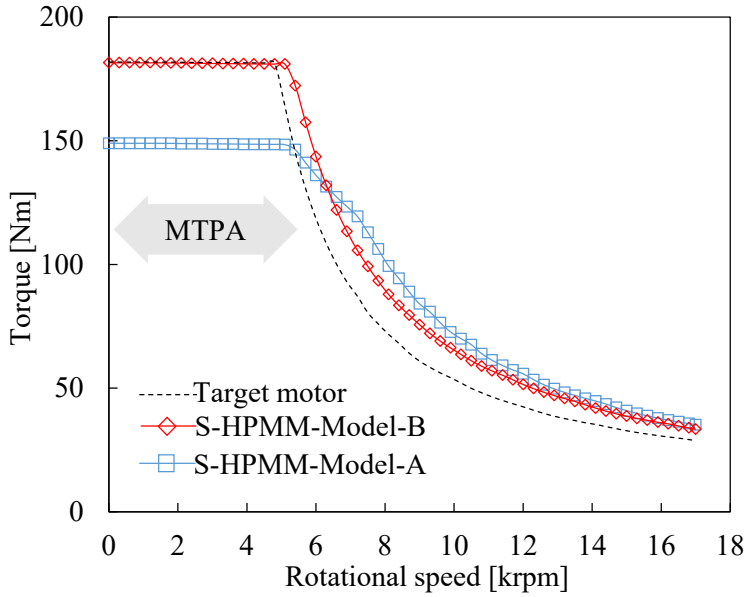

(b)

Fig. 4.32 Torque-Speed curve (Input condition : 600Vdc, 180A) (a) P-HPMM (b) S -HPMM.

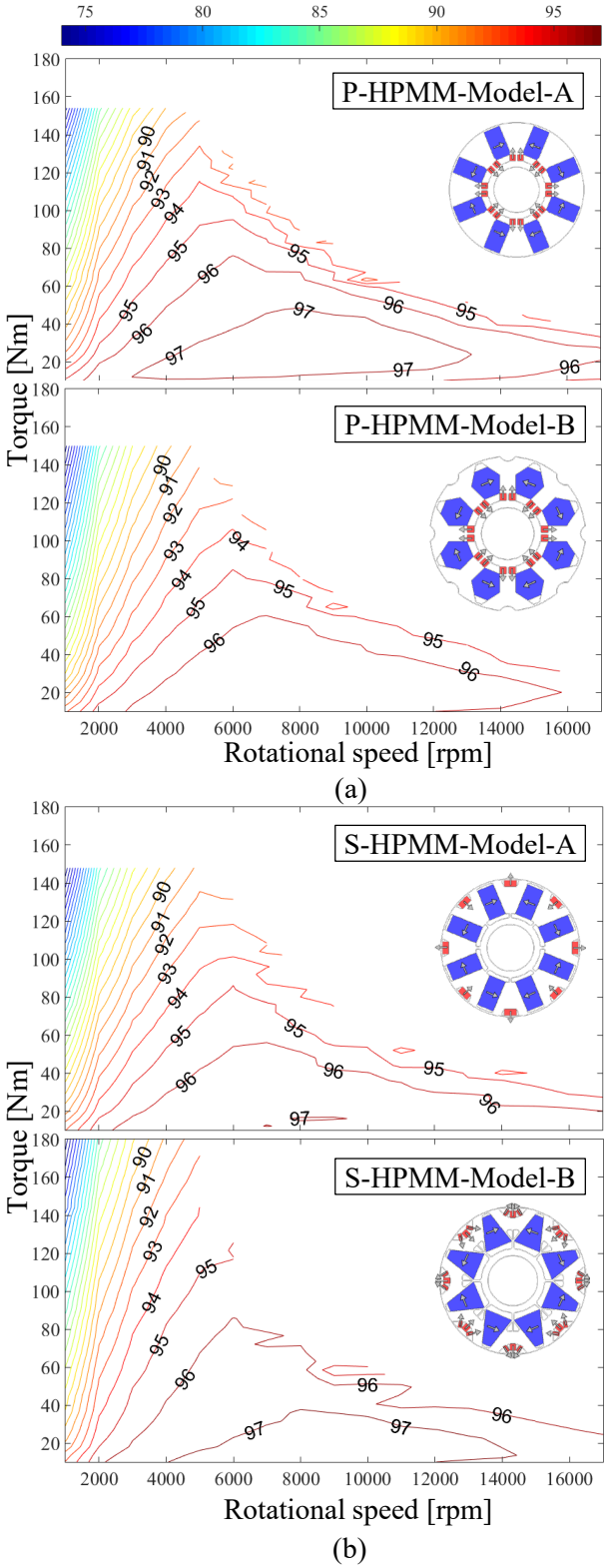

Fig. 4.33 Efficiency map (Input condition : 600Vdc, 180A) (a) P-HPMM (b) S-HP MM.

4.4.5 Characteristic Curve

Automobile traction motors operate in a wide speed range under limited voltage and current conditions. Therefore, in order to estimate the torque characteristics by rotational speed under limited input conditions, the voltage is calculated by (2.4.3) and (2.4.4) and the torque is calculated by (2.4.13). The input limit is expressed as (2.4.1) and (2.4.2).

Fig. 4.32 shows the torque-speed curve at DC link voltage 600 Vdc and input current 180 Arms. The coil and PM temperature are based on 100 ℃. In Fig. 4.32(a), the P-HPMM-Model-A and B do not meet the torque characteristics of the target motor in maximum torque per ampere (MTPA) control region. This is because MTPA is operating method that produces a given torque command with the smallest current through the optimal current combination of i_d and i_q, and the maximum torque of each P-HPMM model does not meet the target torque as shown in Fig. 31(a).

In Fig. 4.32(b), S-HPMM-Model-A does not meet the target torque in the MTPA control region, but S-HPMM-Model-B meets the performance characteristics of the target motor over the whole speed range.

4.4.6 Efficiency map

Fig. 4.33 shows the efficiency map for each HPMM model at DC link voltage 600 Vdc. The coil and PM temperature are based on 100 ℃. Efficiency η is calculated as (4.4.6.1).

$$\eta = \frac{P_m}{P_c + P_i + P_m} \times 100\,(\%) \tag{4.4.6.1}$$

where P_m is the mechanical output; P_c and P_i are the copper and iron loss, respectively.

In Fig. 4.33(a), In the case of P-HPMM-Model-B, demagnetization durability and reluctance torque are improved compared to Model-A, but the high-efficiency region tends to decrease.

In Fig. 4.33(b), In the case of S-HPMM-Model-B, while the torque performance is improved compared to Model-A, the high-efficiency region also tends to expand.

Therefore, the design concept proposed in Fig. 4.22 has the effect of reducing the efficiency in the case of P-HPMM, but improving the efficiency in the case of S-HPMM.

4.4.7 Stress Distribution at Maximum Speed Rotation

Table 4.6 shows the material properties of each part for structural analysis, and the yield point of the core material is 700 MPa at room temperature. A non-magnetic fixture was applied on the top of the Fe-PM to fix the Fe-PM position and to dissipate the stress on the outer diameter of the

rotor core. The contour plots of Mises stress for the rotor of P-HPMM-Model-B and S-HPMM-Model-B at 17,000 rpm are shown in Fig. 4.34. The maximum point is marked with a red box. The P-HPMM-Model-B has a maximum of 1,045 MPa in center-post of the rotor core, and the maximum stress exceeds the yield point of the rotor core. S-HPMM-Model-B is up to 581 MPa at the center-post of rotor core and has a safety factor of 1.2.

Table. 4.6 Material properties for structural analysis

Item	Unit	Core	Fe-PM	Nd-PM
Density	kg/m^3	7,650	5,100	7,620
Young's Modulus	GPa	183	190	160
Possion's Ratio	-	0.30	0.35	0.24
Yield Point	MPa	700	-	-

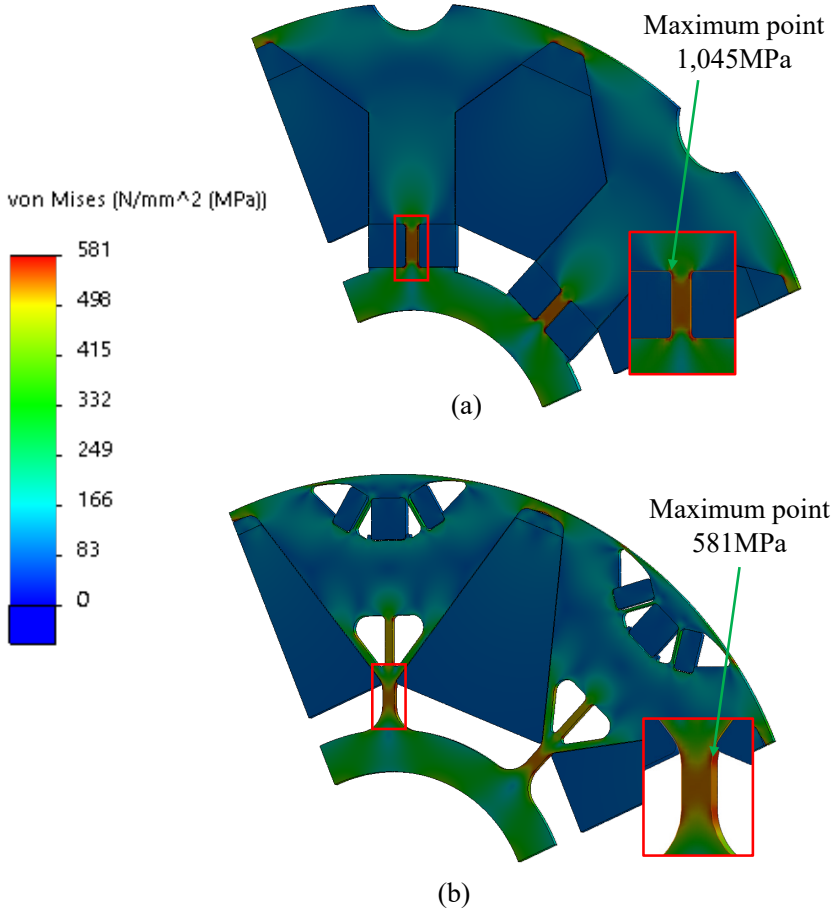

Fig. 4.34 Mises stress for the rotor core at maximum rotation speed 17,000rpm (a) P-HPMM-Model-B (b) S-HPMM-Model-B.

In order to alleviate the maximum stress locally generated in the rotor core, it is required to increase the radius value of the curve at the stress generating area. In P-HPMM, Nd-PM is inserted on the inner diameter side of the rotor core to improve demagnetization durability. However, this structure is disadvantageous compared to the S-HPMM in terms of complementing the rotational stiffness because it is difficult to improve the curvature radius of the center-post.

4.4.8 Final Proposal Model Suitable as Dy-Free Hybrid PM Motor

Therefore, this chapter proposes S-HPMM-Model-B as a Dy-free HPMM suitable for automobile traction motors, taking into account electromagnetic motor performance and rotational rigidity characteristics.

4.5 Summary for Chapter 4

In this chapter, new P-HPMM and S-HPMM models suitable for automotive environmental temperature conditions were proposed. As a result of comparing each of the proposed models in terms of performance characteristics, the S-HPMM-Model-B was finally proposed. The proposed model shows the reliability of demagnetization durability even when 21 kOe Nd-PM and 5.5 kOe Fe-PM are applied, and under the same torque and power density as the target motor, the usage of Nd-PM and the total PM cost were reduced by 47 % and 10 %, respectively.

Chapter 5. Evaluation of Switching Ripple Effect on Efficiency of Proposed HPMM

In general, IPMSMs for traction applications employ Nd-PM, but there is concern about cost and stable supply because Nd-PM includes Dy. Thus, a novel spoke-type HPMM employing Dy-free PM and ferrite PM is proposed to Chapter 4. The proposed HPMM can achieve same torque density as target IPMSM mounted in TOYOTA Prius 4th generation. As a results, the proposed HPMM realizes 10% lower PM cost than that of the target IPMSM. However, the proposed IPMSM has lower efficiency because high tensile steel sheet, which has high iron loss density, is needed for improving mechanical strength. On the other hand, in the previous research, comparison between the proposed HPMM and target IPMSMs have been carried out by FEA with sinusoidal current wave. In the actual operation, input current includes switching ripple caused by the inverter. The switching ripple dramatically increases the eddy current in magnet and winding due to Nd-PM and the rectangular copper wire. However, the proposed HPMM can restrain the increase in the eddy current loss caused by the switching ripple because the ferrite PM is dominant. In addition, the proposed HPMM has larger magnetic resistance than that of the target IPMSM due to large ferrite PMs. Hence, the variation of magnetic flux in the winding, and this means that the proposed HPMM can restrain the eddy current loss in the rectangular copper wire. In this research, two models are compared by FEA considering the eddy current loss in the winding and the effect on the switching ripple in various switching frequency of an inverter, and finally, effectiveness of the proposed model is shown.

5.1 Comparison of Electromagnetic Properties between the Target Motor and the Proposed HPMM

Fig. 4.12 and Fig. 4.22(d) show the cross-sectional shapes of the proposed HPMM and the target IPMSM, respectively. Table 4.5 shows the main specifications of each IPMSM. The rotor shape of the proposed HPMM is a structure in which a diamond-shaped ferrite PM on the q-axis and a U- shaped Nd-PM on the d-axis are inserted. Accordingly, each PM constitutes a series circuit on the d-axis magnetic equivalent circuit, and high d-axis reluctance can be obtained. That is, a low Ld can be expected. In addition, a high Lq can be expected as a q-axis flux path is secured between each PM. Therefore, since it is a structure in which a high saliency ratio can be generated, an improvement in reluctance torque can be expected.

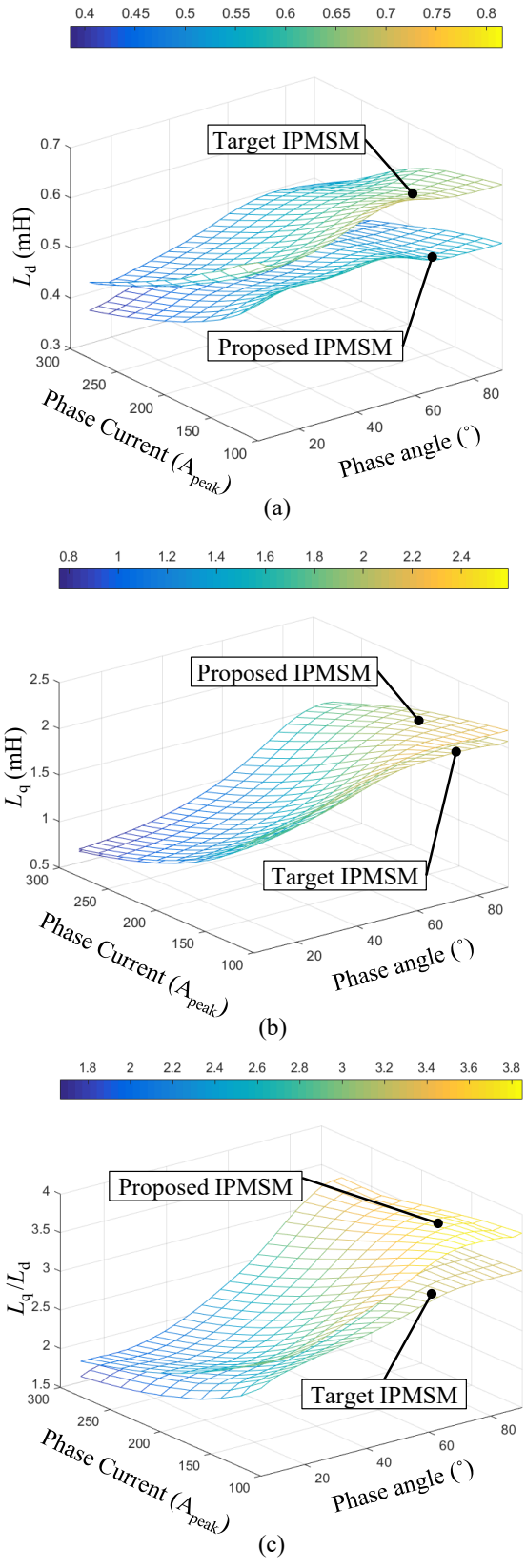

Fig. 5.1 Inductance comparison (a) L_d (b) L_q (c) saliency ratio (L_q/L_d).

Fig. 5.1 shows the comparison of the distribution of inductance in the entire input current region. As shown in Fig. 5.1(a), the proposed HPMM has a lower L_d distribution than the target IPMSM. Also, as shown in Fig. 5.1(b), L_q is generally high. Therefore, as shown in Fig. 5.1(c), the saliency ratio is high in the entire current region.

Ferrite PM's residual magnetic flux density is 1/3 of that of general Nd-PM. In addition, the proposed HPMM uses 47 % less Nd-PM than the target IPMSM. Therefore, it can be expected that the proposed HPMM will have low PM torque. Fig. 5.2 shows the comparison of the back-EMF according to the PM temperature at a rotation speed of 1,000 rpm. As shown in Fig. 5.2, since the proposed HPMM has a lower back EMF compared to the target IPMSM, it can be expected that the PM torque is also low. What is interesting is that the difference in back-EMF gradually increases as the PM temperature increases, and then decreases after the PM temperature is 120 ℃. The reason the difference increases is because of the difference in the β coefficient of each PM. The β coefficient of Nd-PM is 0.1 %/℃, whereas that of ferrite PM is 0.25 %/℃. That is, as the PM temperature increases, the decrease in the residual magnetic flux of

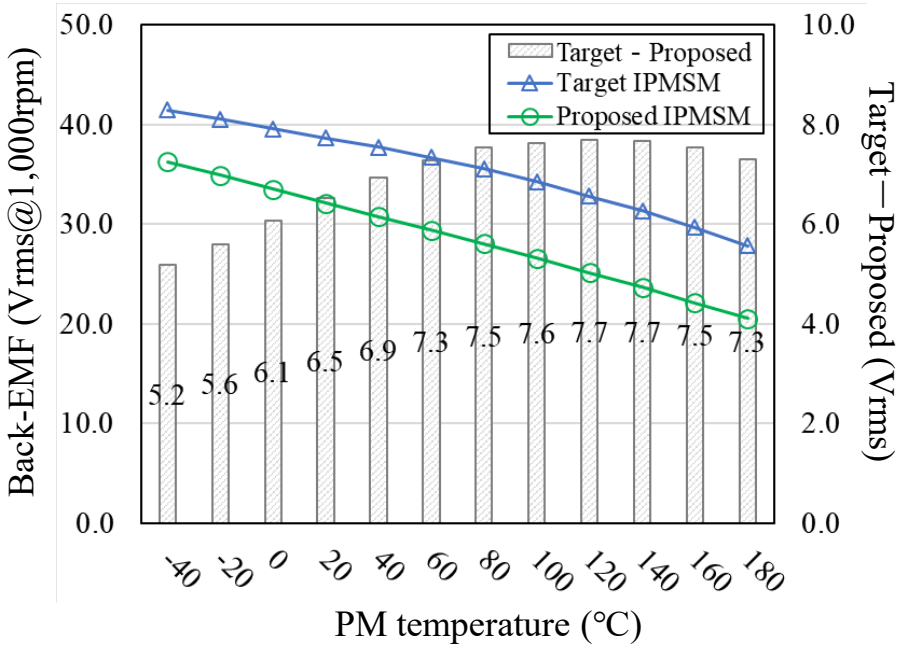

Fig. 5.2 Back-EMF comparison by PM temperature.

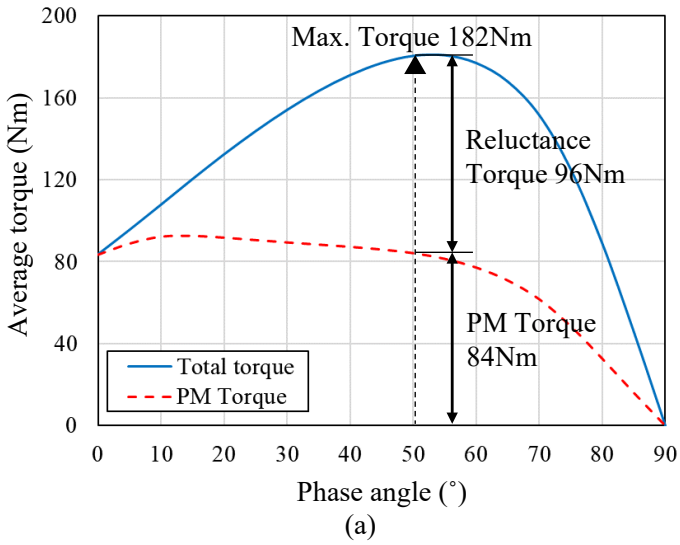

(a)

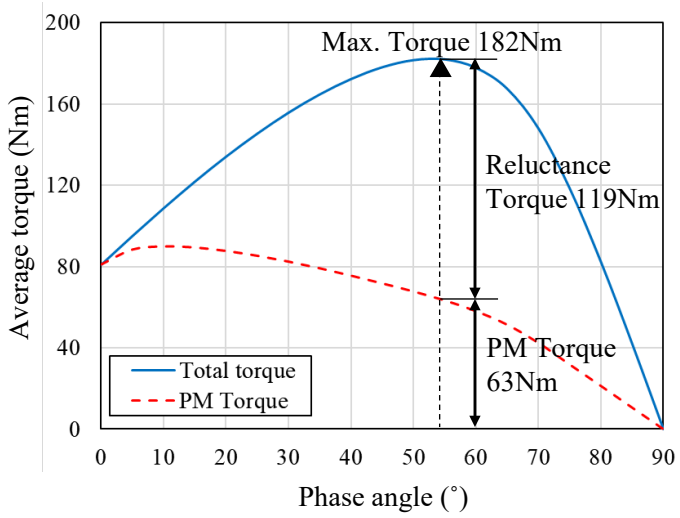

(b)

Fig. 5.3 Average torque by phase angle in input current 180Arms (a) Target IPMSM (b) Proposed HPMM.

the ferrite PM is greater. However, the reason the difference decreases after the PM temperature is 120 ℃ is due to the effect of leakage flux. As the temperature of the PM increases, the amount of leaked flux around the PM is gradually increased compared to the amount of flux linked to the stator coil. That is, the proposed HPMM has a structure in which the amount of leakage flux due to the increase of the PM temperature is smaller than that of the target IPMSM. Considering that the operating temperature range of the vehicle traction motor is mostly between 80 and 120 ℃, it can be expected that the proposed HPMM will exhibit lower PM torque compared to the target IPMSM. However, since the saliency ratio of the proposed HPMM in Fig. 5.1(c) is high in the

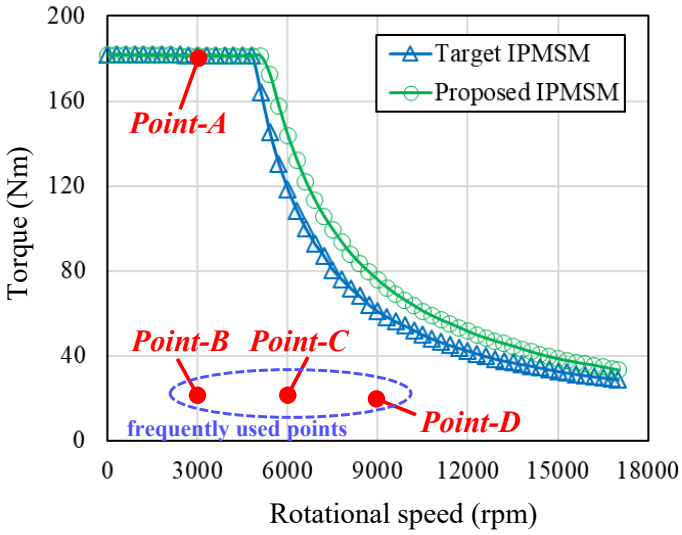

Fig. 5.4 Torque-speed curve in input current 180Arms and DC link voltage 600Vdc.

entire operating range, the reluctance torque is improved, so that the same torque density can be expected in terms of the total torque.

Fig. 5.3 shows the average torque for each current phase angle. The input current is 180 Arms, and the PM temperature is based on 100 ℃. Fig. 5.3(a) is for the target IPMSM. At the maximum torque point, the PM torque is 84 Nm and the reluctance torque is 96 Nm. Fig. 5.3(b) is for the proposed HPMM. At the maximum torque point, the PM torque is 63 Nm and the reluctance torque is 119 Nm. As shown in Fig. 5.3, although the PM torque of the proposed HPMM is 25 % lower than that of the target IPMSM, the reluctance torque is 24% higher, so the same torque density is realized in terms of the total torque.

Fig. 5.4 shows the torque-speed curve under the input current of 180Arms and the DC link voltage of 600Vdc. As shown in Fig. 5.4, the proposed HPMM shows higher output characteristics than the target IPMSM. The flux-weakening control performance is determined by the ratio of PM flux linkage λ_{pm} and d-axis inductance L_d. Although the proposed HPMM has low λ_{pm}, it has a relatively low L_d, so it tends to show high performance of weak flux control. In a traction motor with a wide variable speed operating range, this tendency is a good performance characteristic. Also, for the efficiency evaluation considering the switching ripple characteristics, Fig. 5.4 shows the main operating area from *point-A* to *point-D*.

5.2 Efficiency considering Switching Ripple Effect

5.2.1 Analysis of Input Current including Switching Ripple

In Fig. 5.4, *Points-A* to *D* are indicated for efficiency analysis considering the switching ripple current. *Point-A* is the maximum torque point, and *Points-B* to *D* are the main operating points. In addition, among the main operating points, the key point is the *Point-C*. Fig. 5.5 shows the circuit configuration for generating the switching ripple current. The circuit configuration was implemented in PSIM, a commercial tool.

Fig. 5.6 and 5.7 show the switching ripple currents at *Points-A* and *C*, respectively. Fig. 5.6(a) and 5.7(a) have a switching frequency of 5 kHz (f_{sw}=5kHz), and Fig. 5.6(b) and 5.7(b) have a switching frequency of 20 kHz (f_{sw}=20kHz). Also, in Fig. 5.6, the input current is 180 Arms and the rotation speed is 3,000 rpm, and in Fig. 5.7, the input current is 30 Arms and the rotation speed is 6,000 rpm.

The tendency of each current waveform is shown as the lower the rotational speed and the greater the switching frequency, the less harmonic the effect is. Conversely, the higher the rotation speed and the lower the switching frequency, the greater the influence of harmonics. Based on these current waveforms, the analysis results for the loss and efficiency characteristics of each IPMSM are as follows.

Fig. 5.8 shows the joule loss of the coil at *Point-A* of the proposed HPMM. Joule loss is divided into copper loss and eddy current loss. Eddy current loss is a loss caused by the skin effect and proximity effect, and is also called AC copper loss.

At f_{sw}=5kHz, the copper loss is 6,937W, and the eddy current loss is 330.7W. When f_{sw}=20kHz, the copper loss is the same, but the eddy current loss is 277.1W, which is reduced by 53.6W. This shows that as the switching frequency increases, the eddy current loss decreases.

Fig. 9 shows the joule loss of the coil at *Point-C* of the proposed HPMM. At f_{sw}=5 kHz, the copper loss is 193 W, and the eddy current loss is 71.9 W. When f_{sw}=20 kHz, the copper loss is the same, but the eddy current loss is 32.2W, which is reduced by 29.7W. Similarly, as the result at *Point-A*, this shows that as the switching frequency increases, the eddy current loss decreases.

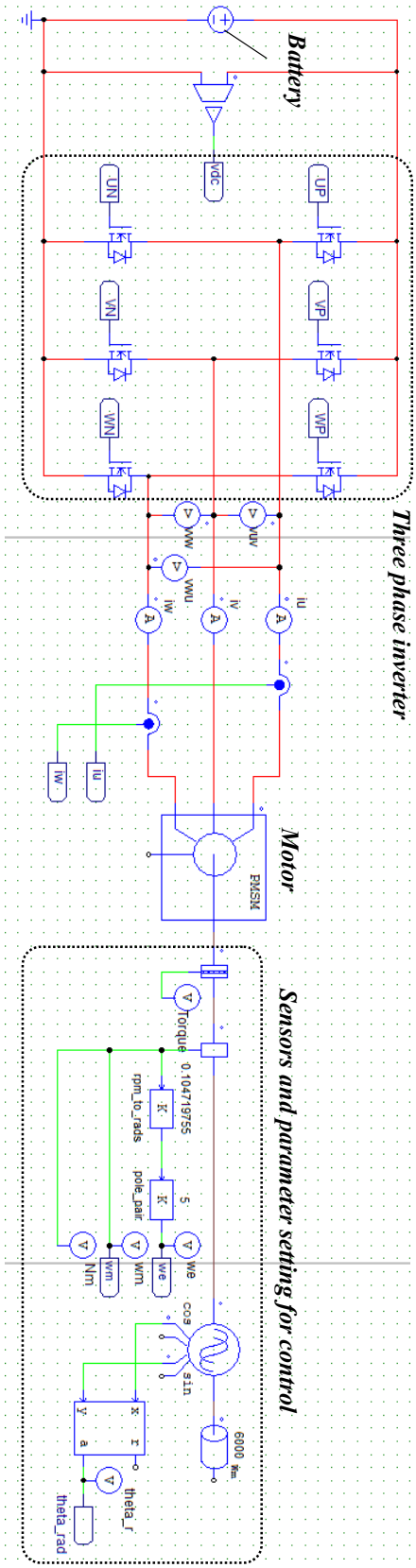

Fig. 5.5 Circuit configuration to analyze current waveform in PSIM.

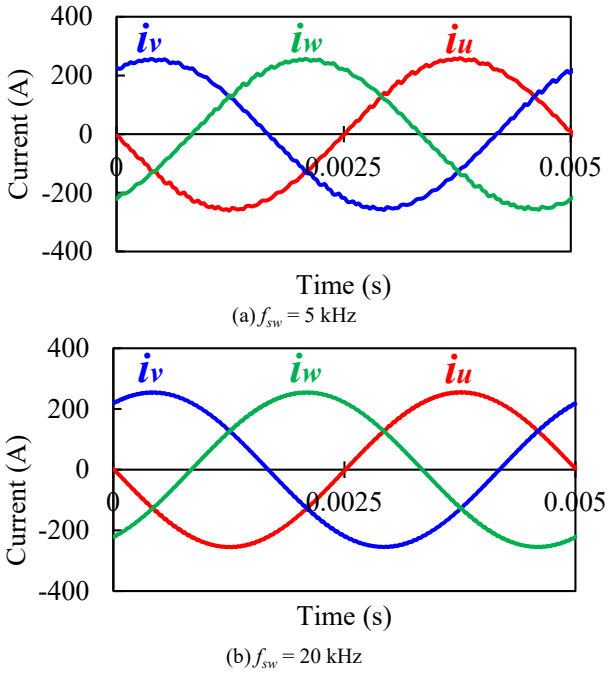

Fig. 5.6 Simulated input current at *Point-A* (@3,000 rpm, 180 Arms).

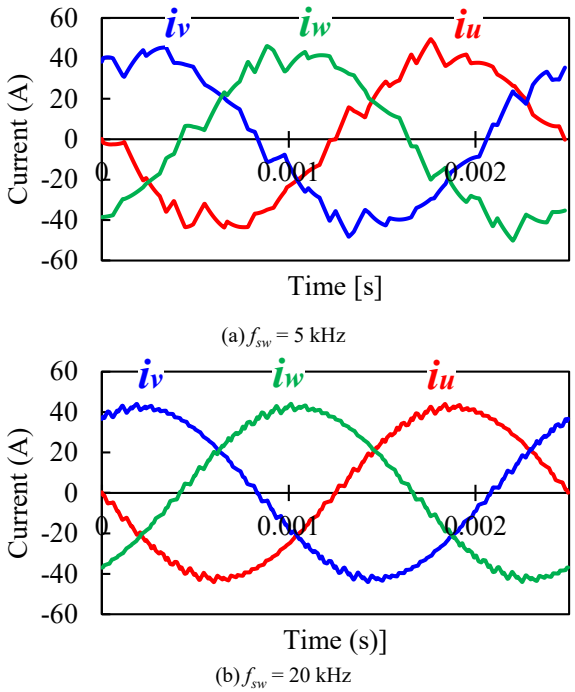

Fig. 5.7 Simulated input current at *Point-C* (@6,000 rpm, 30 Arms).

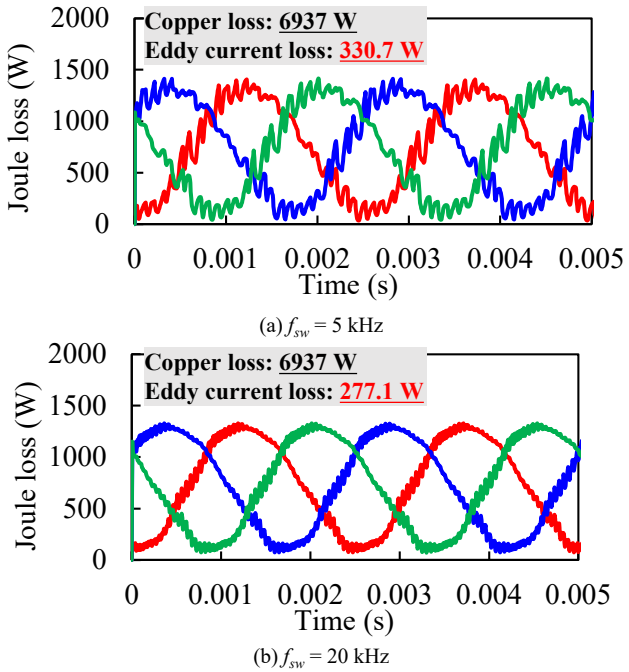

Fig. 5.8 Joule loss (eddy current and copper loss) in winding of the proposed IPMSMs at *Point-A* (@3000 rpm, 180 Arms).

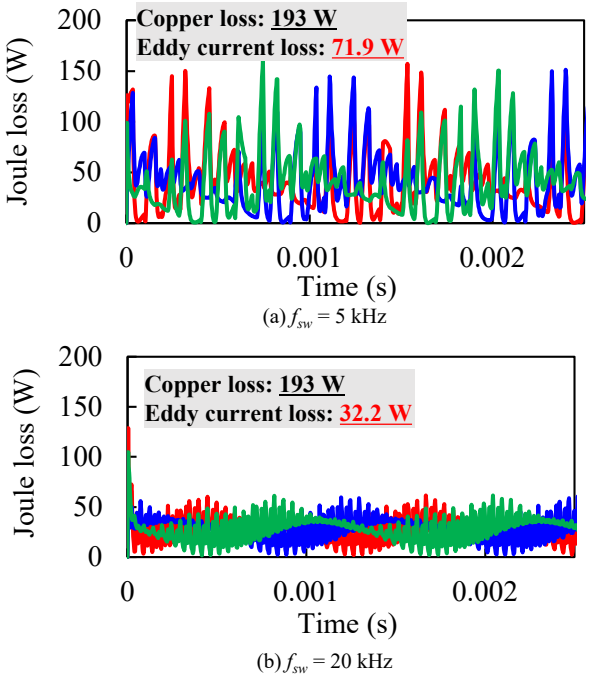

Fig. 5.9 Joule loss (eddy current and copper loss) in winding of the proposed IPMSMs at *Point-C* (@6,000 rpm, 30 Arms).

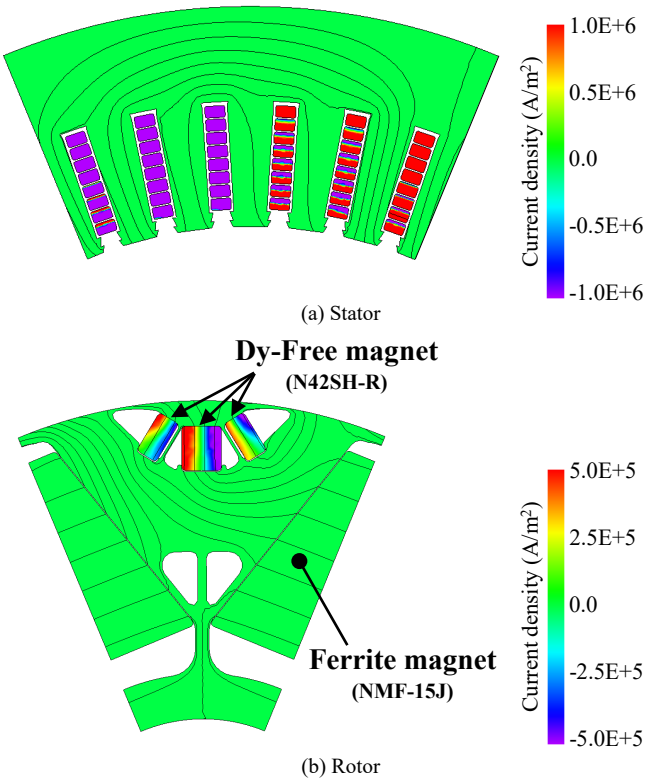

Fig. 5.10 Eddy current distributions of the proposed HPMM at *Point-C* when f_{sw} is 5 kHz (@6,000 rpm, 30 Arms).

Fig. 5.10 shows the eddy current distribution of the proposed HPMM at *Point-C*, and the switching frequency is 5kHz. First, the eddy current distribution in the coil shows a non-uniform distribution in the vertical and horizontal directions. This is due to the effect of the skin effect and the proximity effect. The stator structure of the proposed HPMM is the same as that of the Prius 4th generation traction motor, which is the target IPMSM. The stator has a structure in which a rectangular copper wire is inserted into the stator core as a coil. When the stator coil is inserted as a conductor with a large cross-sectional area, the fill factor increases and the phase resistance decreases. This has the effect of reducing the copper loss of the coil. However, if the cross-sectional area of the coil is increased, the skin effect may be prominent. As a result, due to a local increase in current density, high eddy current loss may be caused. In the case of the current analysis model, the eddy current loss does not appear to be dramatically high as shown in Figs. 5.8 and 5.9

Fig. 5.10 shows the eddy current distribution of the proposed HPMM at *Point-C*, and the switching frequency is 5 kHz. First, the eddy current distribution in the coil shows a non-uniform

distribution in the vertical and horizontal directions. This is due to the effect of the eddy current. The stator structure of the proposed HPMM is the same as that of the Prius 4th generation traction motor, which is the target IPMSM. The stator has a structure in which a rectangular copper wire is inserted into the stator core as a coil. When the stator coil is inserted as a conductor with a large cross-sectional area, the fill factor increases and the phase resistance decreases. This has the effect of reducing the copper loss of the coil. However, if the cross-sectional area of the coil is increased, the eddy current loss becomes large. As a result, a local increase in current density occurs in some conductors. Moreover, at *Point-C*, ratio of the eddy current in the joule loss is higher than *Point-A* since harmonic component is dominant as shown in Figs. 5.6 and 5.7.

In the case of the rotor, the eddy current appears non-uniformly only in the Dy-free magnet,

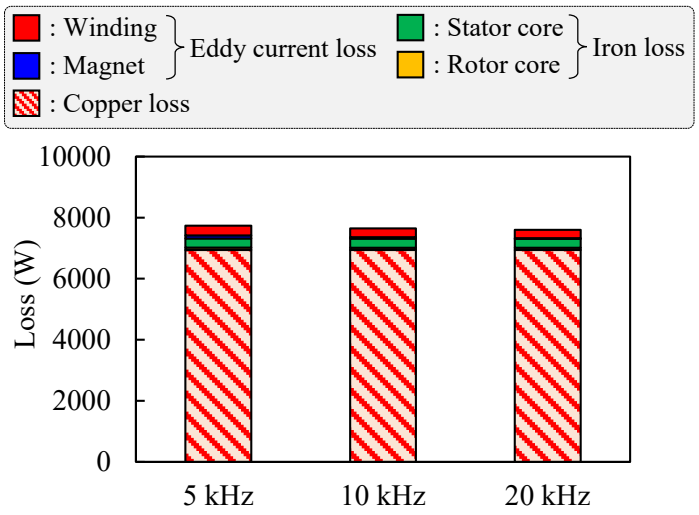

(a) Target IPMSM

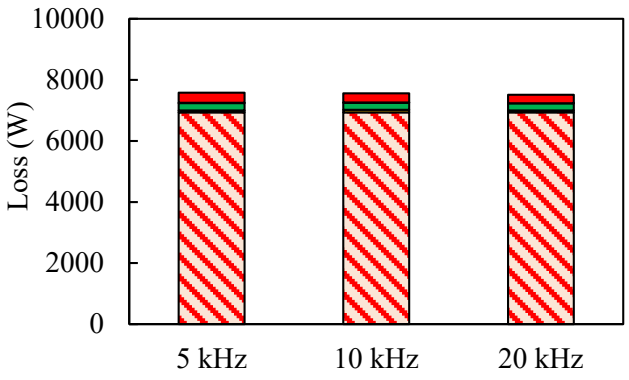

(b) Proposed IPMSM

Fig. 5.11 Loss in both IPMSMs at *Point-A* (@3,000 rpm, 180 Arms).

and hardly appears in the ferrite-magnet. This difference is due to electrical conductivity. Dy-free magnet is Nd-PM, and its electrical conductivity is almost similar to that of iron. On the other hand, the ferrite-magnet has almost zero electrical conductivity. As a result, eddy currents hardly appear in the ferrite-magnet. The proposed HPMM uses a smaller volume of Nd-PM compared to the target IPMSM. Therefore, the proposed HPMM can be expected to improve the eddy current loss in the magnet compared to the target IPMSM.

The above-mentioned analysis method is equally applied to the target IPMSM, and the results of comparison with the proposed HPMM are as follows.

Fig. 5.11 shows the loss characteristics at *Point-A* for the both models. In both models, the copper loss appears to be dominant. In the case of the target IPMSM, the eddy current loss of the

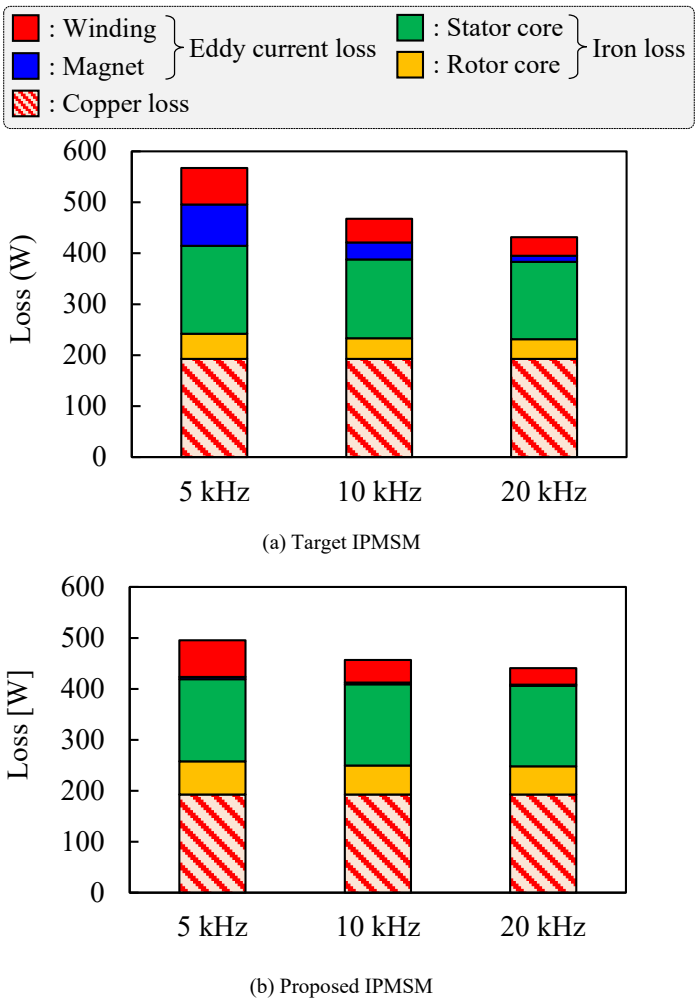

Fig. 5.12 Loss in both IPMSMs at *Point-C* (@6,000 rpm, 30 Arms).

magnet is higher than that of the proposed HPMM. As a result, the total loss tends to be slightly higher, and as the switching frequency increases, the total loss tends to decrease little by little. On the other hand, since the proposed HPMM has very low eddy current loss in the magnet, there is little change in total loss with increasing switching frequency. However, at *Point-A*, total loss in each IPMSM is not strongly affected by the switching frequency because the copper loss, which is constant, is dominant.

Fig. 5.12 shows the loss characteristics at *Point-C* for the both models. At this operating point, total loss of each model markedly varies with the switching frequency because the copper loss is small. Especially, the proposed HPMM shows significantly lower eddy current loss in magnets compared to the target IPMSM. This is because, as illustrated in Fig. 5.10, the amount of Nd-PM used is small and the eddy current of ferrite-PM is close to zero.

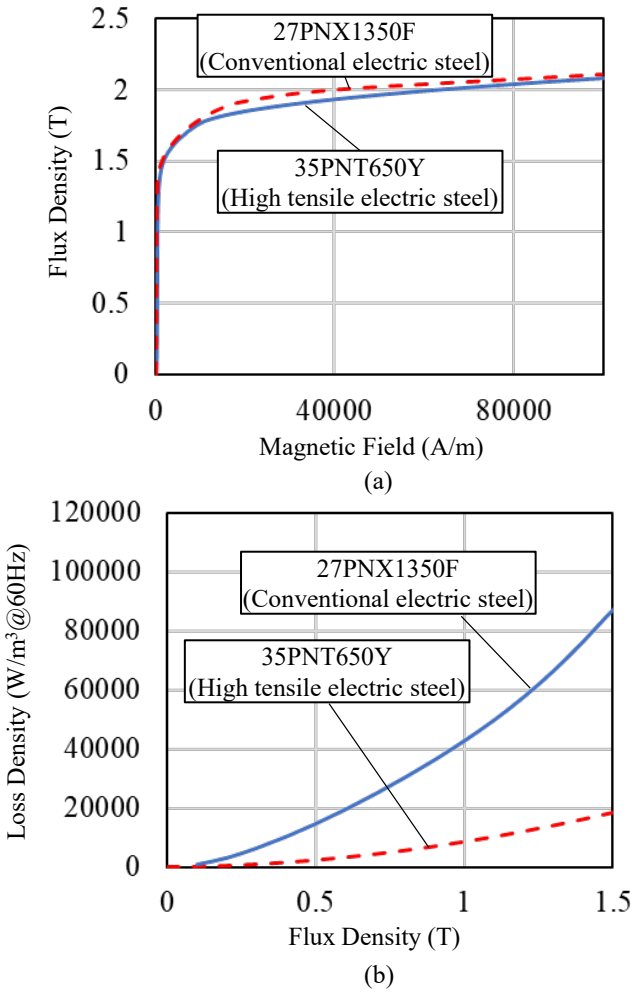

Fig. 5.13 Material properties of electromagnetic steel sheets.

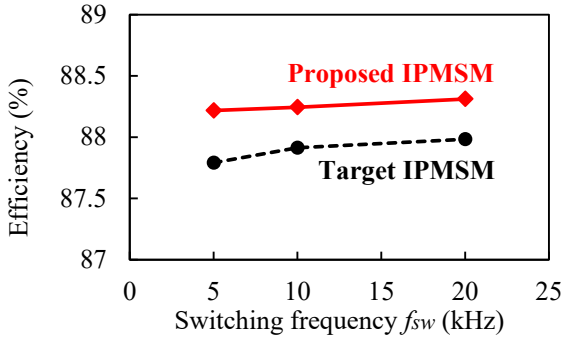

(a) *Point-A* (@3000 rpm, 180 Arms)

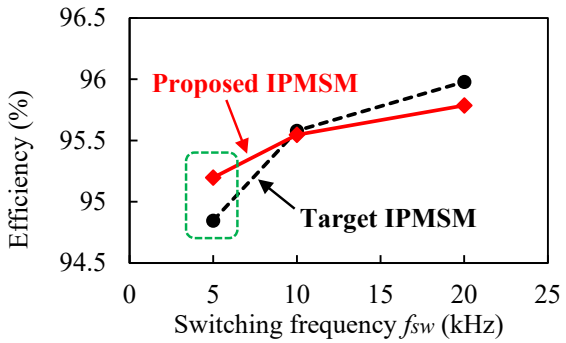

(b) *Point-B* (@3000 rpm, 30 Arms)

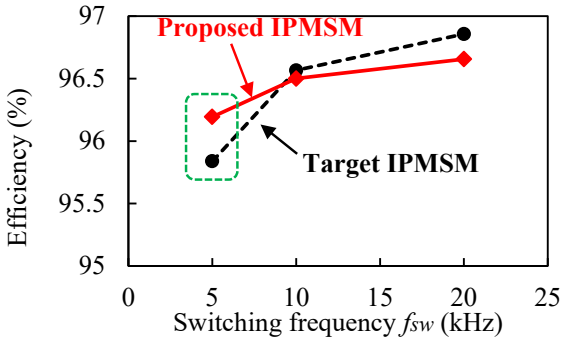

(c) *Point-C* (@6000 rpm, 30 Arms)

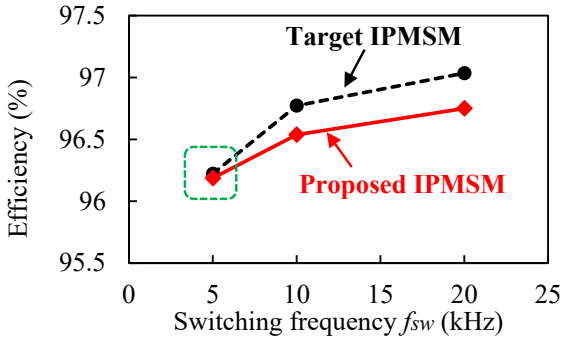

(d) *Point-D* (@9000 rpm, 30 Arms)

Fig. 5.14 Efficiency of both IPMSMs versus switching frequency fsw at four different operating points.

However, the proposed HPMM shows a higher overall iron loss in the rotor core compared to the target IPMSM. The reason is that a high-tensile electrical steel sheet is applied to the proposed HPMM.

The proposed HPMM basically assumes that the ferrite PM is inserted as a spoke type. The spoke type has an advantageous structure for concentrating magnetic flux, but is disadvantageous in terms of maintaining rotational rigidity at high rotation. To compensate for this, in the previous study, a high-tensile electrical steel sheet was applied to the rotor core. The yield point of the high tensile steel sheet applied to the proposed HPMM is 700 MPa, and the yield point of the target IPMSM is 420 MPa, which is about 1.67 times higher.

As shown in Fig. 5.13, although the saturated magnetic flux density of the high-tensile steel sheet is slightly lower than that of the conventional electrical steel sheet, the iron loss is very large. This means that the iron loss of the rotor core is increased during high-speed operation.

Fig. 5.14 shows the efficiency according to the switching frequency for both models. In *Point-A*, the proposed HPMM shows high efficiency in the entire frequency domain. In *Point-B*, the proposed HPMM shows lower efficiency than that of the target IPMSM if the switching frequency is over of 10 kHz. On the other hand, in realistic 5 kHz to 10 kHz region, the actual efficiency can be said to be superior to that of the target motor. This characteristic of the proposed HPMM is suitable for traction applications. *Point-C* shows a similar tendency to *Point-B*. In *Point-D*, the proposed HPMM shows lower efficiency compared with the target IPMSM in high switching frequency region. However, at 5 kHz, the proposed HPMM can show almost same efficiency as the target IPMSM although the high tensile steel sheet is used.

5.3 Summary for Chapter 5

In this chapter, due to the application of ferrite-magnet and the use of a small volume of Nd-PM, the proposed HPMM shows advantageous properties in terms of heat generation of the magnet. Also, in frequently used operating range, it exhibits equivalent or higher efficiency characteristics in the region under 10 kHz which is the main switching frequency range. In other words, the proposed HPMM achieves low cost and high efficiency at the same time. These advantages mean advantageous characteristics as a traction motor for automobiles.

Chapter 6. Conclusions of this Thesis and Future Work

6.1 Conclusions

In this study, a rotor topology for a new HPMM suitable for a vehicle traction motor was proposed. The proposed HPMM realizes the same power density and torque density as the target motor, and at the same time can reduce Nd-PM usage and cost.

This HPMM was aimed to be applied to a vehicle traction motor system. In addition, different types of magnets such as Nd-PM and Fe-PM are applied to HPMM, and the basic mathematical modeling is the same as that of IPMSM. Therefore, in Chapter 2, the structure and requirements of the vehicle traction motor system, the properties of magnets, and the governing equations of the IPMSM were discussed.

Based on this theoretical background, Chapter 3 proposed a novel HPMM suitable as a traction motor for BEV. HPMM is divided into parallel type and series type according to the *d*-axis magnetic equivalent circuit. When considering the manufacturing process of a traction motor for a vehicle, it is suggested that the serial type is suitable. In addition, the disadvantage of the series type is low PM flux. In order to overcome this, it is theoretically suggested that the reluctance torque improvement is necessary through securing the *q*-axis magnetic path. In conclusion, the proposed HPMM realizes the same torque density and reduces Nd-PM cost by 35%.

As mentioned in Chapter 3, the series type HPMM has low PM flux, but this means that the *d*-axis magnetic resistance is high. Based on these characteristics, Chapter 4 proposes a Dy-free Nd-PM-based HPMM suitable for HEV traction motors. The proposed HPMM realizes Dy-free and at the same time reduces the magnet cost by 10%.

The HPMM proposed in Chapter 4 has high magnetic resistance. This is an advantageous characteristic for reducing eddy current loss due to harmonic current. Based on the advantages of the series type HPMM, Chapter 5 analyzed the efficiency characteristics considering the switching ripple of the input current. Efficiency characteristics from 5 to 20 kHz of switching frequency at the main operating point were analyzed. As a result of the analysis, the proposed HPMM was advantageous in terms of efficiency compared to the target motor in the range of 5 to 10 kHz, which is the main driving frequency.

In conclusion, the structure of the new HPMM proposed in this study satisfies the durability

required for vehicles, reduces magnet cost, and proves advantageous in terms of efficiency.

6.2 Future Work

The proposed HPMM has high reluctance torque. High reluctance torque causes increased torque ripple, which is an unfavorable characteristic in terms of NVH. A way to improve this is to reduce torque ripple through harmonic current injection. Therefore, as the first future task, we propose a study on harmonic injection current for torque ripple reduction.

The second is the optimal design of HPMM through stator redesign. In this study, HPMM was proposed based on the same stator structure as the target motor. However, if the stator is redesigned, it is expected that the magnet cost can be reduced more dramatically.

The third is the optimal design of the rotor structure using an optimization algorithm. In the CAE-based motor design process, research cases in which various optimization algorithms are grafted to improve performance have been reported. Similarly, we propose a study on implementing a more improved rotor topology by grafting various optimization algorithms based on HPMM.

The fourth is the study of HPMM using various Dy-free magnets. In this study, 21 kOe of Nd-PM was applied as a Dy-free magnet. As a Dy-free magnet, there are various magnets such as MQ magnet series of hot press forming method and Nd bonded magnet series of injection method. By grafting these magnets, we propose to conduct research on a new topology of HPMM.

Reference

[1] G. Pellegrino, A. Vagati, and P. Guglielmi, “Design tradeoffs between constant power speed range, uncontrolled generator operation, and rated current of IPM motor drives,” *IEEE Trans. Ind. Appl*., vol. 47, no. 5, pp. 1995–2003, Sep./Oct. 2011.

[2] M. Barcaro, N. Bianchi, and F. Magnussen, “Permanent-magnet optimization in permanent-magnet-assisted synchronous reluctance motor for a wide constant-power speed range,” *IEEE Trans. Ind. Electron*., vol. 59, no. 6, pp. 2495–2502, Jun. 2012.

[3] G. Pellegrino, A. Vagati, P. Guglielmi, and B. Boazzo, “Performance comparison between surface-mounted and interior PM motor drives for electric vehicle application,” *IEEE Trans. Ind. Electron*., vol. 59, no. 2, pp. 803–811, Feb. 2012.

[4] A. Wang, Y. Jia, and W. L. Soong, “Comparison of five topologies for an interior permanent-magnet machine for a hybrid electric vehicle,” *IEEE Trans. Magn*., vol. 47, no. 10, pp. 3606–3609, Oct. 2011.

[5] Z. Q. Zhu and D. Howe, “Electrical machines and drives for electric, hybrid and fuel cell vehicles,” *Proc. IEEE*, vol. 95, no. 4, pp. 746–765, Apr. 2007.

[6] M. N. Uddin, T. S. Radwan, and M. A. Rahman, “Performance of interior permanent magnet drive over wide speed range,” *IEEE Trans*. *Energy Convers.,* vol. 17, no. 1, pp. 79–84, Mar. 2002.

[7] S.-M. Sue and C.-T. Pan, “Voltage-constraint-tracking-based fieldweakening control of IPM synchronous motor drives,” *IEEE Trans*. *Ind. Electron*., vol. 55, no. 1, pp. 340–347, Jan. 2008.

[8] S.-I. Kim, G.-H. Lee, J.-P. Hong, and T.-U. Jung, “Design process of interior PM synchronous motor for 42-V electric air-conditioner system in hybrid electric vehicle,” *IEEE Trans. Magn*., vol. 44, no. 6, pp. 1590–1593, Jun. 2008.

[9] Q. Chen, G. H. Liu, W. X. Zhao, L. G. Sun, and M. M. Shao, “Design and comparison of two fault-tolerant interior-permanent-magnet motors,” *IEEE Trans. Ind. Electron*., vol. 61, no. 12, pp. 6615–6623, Dec. 2014.

[10] S. S. Wu, D. D. Reigosa, Y. Shibukawa, M. A. Leetmma, R. D. Lorenz, and Y. D. Li, “Interior permanent-magnet synchronous motor design for improving self-sensing performance at very low speed,” *IEEE Trans. Ind. Appl*., vol. 45, no. 6, pp. 1939–1946, Nov./Dec. 2009.

[11] K. Yamazaki and M. Kumagai, “Torque analysis of interior permanent magnet synchronous motors by considering cross-magnetization: Variation in torque components with permanent-magnet configurations,” *IEEE Trans. Ind. Electron*., vol. 61, no. 7, pp. 3192–3201, Jul. 2014.

[12] J. Du, X. Wang, H. Lv, “Optimization of Magnet Shape Based on Efficiency Map of IPMSM for EVs,” *IEEE Trans. On Applied Superconductivity*, vol. 26, no. 7, 7 pages, Oct. 2016.

[13] R. Tsunata, M. Takemoto, S. Ogasawara, A. Watanabe, T. Ueno, K. Yamada, "Development and Evaluation of an Axial Gap Motor using Neodymium Bonded Magnet", *IEEE Trans. Ind. Appl*., vol. 54, No. 1, pp. 254-262, Jan.-Feb. 2018.

[14] M. Si, X. Y. Yang, S. W. Zhao, and S. Gong, "Design and analysis of a novel spoke-type permanent magnet synchronous motor," *IET Elect. Power Appl*., vol. 10, no. 6, pp. 571–580, Jan. 2016.

[15] Y. Zhang, W. Cao, S. McLoone, and J. Morrow, "Design and flux-weakening control of an interior permanent magnet synchronous motor for electric vehicles," *IEEE Trans. Appl. Supercond*., vol. 26, no. 7, Oct. 2016, Art. no. 0606906.

[16] K. M. Rahman, S. Jurkovic, C. Stancu, J. Morgante, P. J. Savagian, "Design and performance of electrical propulsion system of extended range electric vehicle (EREV) chevrolet volt," *IEEE Trans. Ind. Appl*., vol. 51, no. 3, pp. 2479-2488, May/Jun. 2015.

[17] Y. Asano, H. Inaguma, E. Ohtani, M. Sato, M. Okamura, and S. Sasaki, "High performance motor drive technologies for hybrid vehicles," in Proc. Power Convers. Conf., 2007, pp. 1584–1589.

[18] H. Staunton, L. D. Marlino, J. N. Chiasson, and T. A. Burress, "Evaluation of 2004 Toyota Prius hybrid electric drive system," Oak Ridge Nat. Lab., Oak Ridge, TN, USA, Tech. Rep. ORNL/TM-2006/423, 2006.

[19] K. T. Chau, C. C. Chan, and C. Liu, "Overview of permanent-magnet brushless drives for electric and hybrid electric vehicles," *IEEE Trans. Ind. Electron*., vol. 55, no. 6, pp. 2246–2257, Jun. 2008.

[20] M. Kamiya, "Development of traction drive motors for the Toyota hybrid system," in Proc. IPEC, Niigata, Japan, 2005, pp. 1474–1481.

[21] X. Y. Zhu, J. Huang, L. Quan, Z. X. Xiang, and B. Shi, "Comprehensive sensitivity analysis and multi-objective optimization research of permanent magnet flux-intensifying motors," *IEEE Trans. Ind. Electron*., vol. 66, no. 4, pp. 2613–2627, Apr. 2019.

[22] X. Y. Zhu, Z. X. Xiang, L. Quan, W. Y. Wu, and Y. Du, "Multimode optimization design methodology for a flux-controllable stator permanent magnet memory motor considering driving cycles," *IEEE Trans. Ind. Electron*., vol. 65, no. 7, pp. 5353–5366, Jul. 2018.

[23] B. Ma, G. Lei, J. Zhu, Y. Guo, and C. Liu, "Application-oriented robust design optimization method for batch production of permanent-magnet motors," *IEEE Trans. Ind. Electron*., vol. 65, no. 2, pp. 1728–1739, Feb. 2018.

[24] M. Ehsani, K. M. Rahman, and H. A. Toliyat, "Propulsion system design of electric and hybrid vehicles," *IEEE Trans. Ind. Electron*., vol. 44, no. 1, pp. 19–27, Feb. 1997.

[25] M. Zeraoulia, M. E. H. Benbouzid, and D. Diallo, "Electric motor drive selection issues for HEV propulsion system: A comparative study," *IEEE Trans. Veh. Technol*. vol. 55, no. 6, pp. 1756–1764, Nov. 2006.

[26] P. H. Nguyen, E. Hoang, and M. Gabsi, "Performance synthesis of permanent-magnet synchronous machines during the driving cycle of a hybrid electric vehicle," *IEEE Trans. Veh. Technol*., vol. 60, no. 5, pp. 1991–1998, Jun. 2011.

[27] V. Ruuskanen, J. Nerg, J. Pyrhonen, S. Ruotsalsinen, and R. Kennel, “Drive cycle analysis of a permanent-magnet traction motor based on magnetostatic finite-element analysis,” *IEEE Trans. Veh. Technol*., vol. 64, no. 3, pp. 1249–1254, Mar. 2015.

[28] A. Emadi, Advanced Electric Drive Vehicles, Boca Raton, FL: CRC Press, Oct. 2014.

[29] Mehrdad Ehsani, Yimin Gao, and Ali Emadi, Modern Electric, Hybrid Electric and Fuel Cell Vehicles Fundamentals, Theory and Design, second edition, New York: Taylor and Francis Group, LLC, 2010.

[30] Y. Yang and A. Emadi, "Hybrid and plug-in hybrid vehicles," in Wiley Encyclopedia of Electrical and Electronics Engineering, John Wiley & Sons, 2013, pp. 1-22.

[31] Y. Yang, K. Arshad-Ali, J. Roeleveld, and A. Emadi, "State-of-the-art electrified powertrains: hybrid, plug-in hybrid, and electric vehicles," International Journal of Powertrains, vol. 5, no. 1, pp. 1-29, 2016.

[32] "What is a Strong Magnet?". The Magnetic Matters Blog. Adams Magnetic Products. October 5, 2012. Archived from the original on March 26, 2016. Retrieved October 12, 2012.

[33] Lucas, Jacques; Lucas, Pierre; Le Mercier, Thierry; et al. (2014). Rare Earths: Science, Technology, Production and Use. Elsevier. pp. 224–225. ISBN 978-0444627445.

[34] M. Sagawa; S. Fujimura; N. Togawa; H. Yamamoto; Y. Matsuura (1984). "New material for permanent magnets on a base of Nd and Fe (invited)". Journal of Applied Physics. 55 (6): 2083. Bibcode:1984JAP....55.2083S. doi:10.1063/1.333572.

[35] J. J. Croat; J. F. Herbst; R. W. Lee; F. E. Pinkerton (1984). "Pr-Fe and Nd-Fe-based materials: A new class of high-performance permanent magnets (invited)". Journal of Applied Physics. 55 (6): 2078. Bibcode:1984JAP.55.2078C. doi:10.1063/1.333571.

[36] N. Schofield, Lecture notes of ECE 787, department of Electrical and Computer Engineering, McMaster University, 2014.

[37] Fraden, Jacob (2010). Handbook of Modern Sensors: Physics, Designs, and Applications, 4th Ed. USA: Springer. p. 73. ISBN 978-1441964656.

[38] "What are neodymium magnets?". wiseGEEK website. Conjecture Corp. 2011. Retrieved October 12, 2012.

[39] T. Nakada, S. Ishikawa, and S. Oki. "Development of an electric motor for a newly developed electric vehicle," SAE International, Volume 01, No. 1879, (2014).

[40] Trilateral EU-Japan-U.S. Conference on Critical Materials for a Clean Energy Future, Washington D.C., USA, 2011 [Online]. Available: http://energy.gov/sites/prod/files/DOE_CMS2011_FINAL_Full.pdf

[41] A. Chiba, N. Hoshi, M. Takemoto, S. Ogasawara, S. Morimoto, M. Sanada, and T. Kosaka, “Rare-earth-free AC motors—An alternative approach advances,” in Proc. IEMDC Keynote Lecture, 2011, pp. 1–5.

[42] J. Rowlatt, “Rare earths: Neither rare, nor earths,” BBC NEWS, [Online]. Available: http://www.bbc.com/news/magazine-26687605.

[43] X. Liu, H. Chen, J. Zhao, and A. Belahcen, “Research on the performances and parameters of interior PMSM used for electric vehicles,” *IEEE Trans. Ind. Electron*., vol. 63, no. 6, pp. 3533–3545, Jun. 2016.

[44] U.S Drive. [Online]. Available: https://www.energy.gov/sites/default/files/2017/11/f39/EETT%20Roadmap%2010-27-17.pdf

[45] Z. Q. Zhu and X. Liu, “Novel stator electrically field excited synchronous machines without rare-earth magnet,” *IEEE Trans. Magn*., vol. 51, no. 4, Apr. 2015, Art. no. 8103609.

[46] C. Stancu, T. Ward, K. M. Rahman, R. Dawsey and P. Savagian, “Separately Excited Synchronous Motor with Rotary Transformer for Hybrid Vehicle Application,” *IEEE Trans. Ind. Appl.*, vol. 54, no. 1, pp. 223–232, Jan./Feb. 2018.

[47] A. Chiba et al., “Torque density and efficiency improvements of a switched reluctance motor without rare-earth material for hybrid vehicles,” *IEEE Trans. Ind. Appl*., vol. 47, no. 3, pp. 1240–1246, May/Jun. 2011.

[48] A. Chiba, K. Kiyota, N. Hoshi, M. Takemoto, and S. Ogasawara, “Development of a rare-earth-free SR motor with high torque density for hybrid vehicles,” *IEEE Trans. Energy Convers*., vol. 30, no. 1, pp. 175–182, Mar. 2015.

[49] K. Imamura, M. Sanada, S. Morimoto, and Y. Inoue, “Design of switched reluctance motor competitive to 60-kW IPMSM in third-generation hybrid electric vehicle,” *IEEE Trans. Ind. Appl.*, vol. 48, no. 6, pp. 2303–2309, Nov./Dec. 2012.

[50] A. M. Omekanda, “A new technique for multi-dimensional performance optimization of switched reluctance motors for vehicle propulsion,” *in Proc. Ind. Appl*. Soc. Annu. Conf., vol. 1, Pittsburgh, PA, USA, Oct. 13– 17, 2002, pp. 22–26.

[51] S. Wang, Q. Zhan, Z. Ma, and L. Zhou, “Implementation of a 50-kW fourphase switched reluctance motor drive system for hybrid electric vehicle,” *IEEE Trans. Magn*., vol. 41, no. 1, pp. 501–504, Jan. 2005.

[52] B. A. Kalan, H. C. Lovatt, and G. Prout, “Voltage control of switched reluctance machines for hybrid electric vehicles,” in Proc. Power Electron. Spec. Conf., Queensland, Australia, Jun. 23–27, 2002, pp. 1656–1660.

[53] M. K. Rahman and S. E. Schulz, “Design of high-efficiency and high torque-density switched reluctance motor for vehicle propulsion,” *IEEE Trans. Ind. Appl*., vol. 38, no. 6, pp. 1500–1507, Nov./Dec. 2002.

[54] N. Bianchi, S. Bolognani, D. Bon, and M. D. Pre, “Rotor flux-barrier design for torque ripple reduction in synchronous reluctance and PM-assisted synchronous reluctance motors,” *IEEE Trans. Ind. Appl*., vol. 45, no. 3, pp. 921–928, May/Jun. 2009.

[55] E. Howard and M. J. Kamper, “Weighted factor multi-objective design optimization of a reluctance synchronous machine,” *IEEE Trans*. *Ind. Appl*., vol. 52, no. 3, pp. 2269–2279, May/Jun. 2016.

[56] H.W. Kim, K. T. Kim, Y. S. Jo, and J. Hur, “Optimization methods of torque density for developing the neodymium free spoke-type BLDC motor,” *IEEE Trans. Magn*., vol. 49, no. 5, pp. 2173–2176, May 2013.

[57] M. M. Rahman, K. T. Kim, and J. Hur, “Design and optimization of neodymium-free spoke-type motor with segmented wing-shaped pm,” *IEEE Trans. Magn*., vol. 50, no. 2, pp. 865–868, Feb. 2014.

[58] M. Barcaro and N. Bianchi, “Interior PM machines using ferrite to replace rare-earth surface PM machines,” *IEEE Trans. Ind. Appl*., vol. 50, no. 2, pp. 979–985, Mar./Apr. 2014.

[59] S. S. R. Bonthu, A. K. M. Arafat, and S. Choi, “Comparisons of rare-earth and rare-earth-free external rotor permanent magnet assisted synchronous reluctance motors,” *IEEE Trans. Ind. Electron*., vol. 64, no. 12, pp. 9729– 9738, Dec. 2017.

[60] A. Fasolo, L. Alberti, and N. Bianchi, “Performance comparison between switching-flux and IPM machines with rare-earth and ferrite PMs,” *IEEE Trans. Ind. Appl*., vol. 50, no. 2, pp. 3708–3716, Mar./Apr. 2014.

[61] K. Kondo, S. Kusase, T. Maekawa, and K. Hanada, “A new PM-assisted synchronous reluctance motor with three-dimensional trench air gap,” *IEEE Trans. Ind. Appl*., vol. 50, no. 4, pp. 2485–2492, Jul./Aug. 2014.

[62] S. Morimoto, M. Sanada, and Y. Takeda, “Performance of PM-assisted synchronous reluctance motor for high-efficiency and wide constant power operation,” *IEEE Trans. Ind. Appl*., vol. 37, no. 5, pp. 1234–1240, Sep./Oct. 2001.

[63] H. Huang, Y. S. Hu, Y. Xiao, and H. Lyu, “Research of parameters and anti-demagnetization of rare-earth-less permanent magnet-assisted synchronous reluctance motor,” *IEEE Trans. Magn*., vol. 51, no. 11, Nov. 2015, Art. no. 8112504.

[64] Buyukdegirmenci, V.T., Bazzi, A.M., Krein, P.T., et al., “Evaluation of Induction and Permanent-Magnet Synchronous Machines Using Drive-Cycle Energy and Loss Minimization in Traction Applications,” *IEEE Trans. on Ind. Appli*., vol. 50, no. 2, pp. 395-403, 2014.

[65] Christian Ruoff, “Q&A with Tesla’s lead motor engineer”, CHARGED [Online]. Available : https://chargedevs.com/features/qa-with-teslas-lead-motor-engineer-full-interview/

[66] EVANNEX, “Tesla's Chief Motor Engineer Discusses Model 3 Motor Tech”, INSIDE EVs [Online]. Available : https://insideevs.com/news/339825/teslas-chief-motor-engineer-discusses-model-3-motor-tech/

[67] X. Zhu, X. Wang, C. Zhang, L. Wang, and W. Wu, “Design and analysis of a spoke-type hybrid permanent magnet motor for electric vehicles,” *IEEE Trans. Magn*., vol. 53, no. 11, Nov. 2017, Art. no. 8208604.

[68] C. L. Lim, J. Hur. “Optimization design of PMSM with hybrid-type permanent magnet considering irreversible demagnetization,” *IEEE Trans. Magn*., vol. 53, no. 11, Nov. 2017, Art. no. 8110904.

[69] C. L. Lim, Y. K. Kim, J. Hur. “Optimized design of PMSM with hybrid-type permanent magnet for improving performance and reliability,” *IEEE Trans. Ind. Appl.*, vol. 55, no. 5, pp. 4692-4701, Sep/Oct. 2019.

[70] Z. Zhang. “High torque density spoke-type ferrite permanent magnet synchronous machine assisted by rare-earth magnets for traction applications,” *IEEE Energy Conversion and Exposition*, DOI: 10.1109/ECCE44975.2020.9235708.

[71] Q. C, G. H. Liu, and W. X. Zhao, “Design and analysis of the new high-reliability motors with hybrid permanent magnet material” *IEEE Trans*. *Magn*., vol. 50, no. 12, Dec. 2014, Art. no. 8207010.

[72] X. Zhu, W. Wu, L. Quan, Z. Xiang and W. Gu, and C. Zhang, “Design and Multi-Objective Stratified Optimization of a Less-rare-earth Hybrid Permanent Magnets Motor with High Torque Density and Low Cost,” *IEEE Trans*. E*nergy conv*., DOI 10.1109/TEC.2018.2886316.

[73] W. Wu, X. Zhu, L. Quan, Y. Du, Z. Xiang, X. Zhu, “Design and analysis of a hybrid permanent magnet assisted synchronous reluctance motor considering magnetic saliency and PM usage,” *IEEE Trans*. *IEEE Appl*. *Supercond*., vol. 28, no. 3, Apr. 2018, Art. no. 5200306.

[74] A. S. Aladsani and O. Beik, “Design of a multiphase hybrid permanent magnet generator for series hybrid EV,” *IEEE Trans. Energy Convers*., vol. 33, no. 3, pp. 1499–1507, Sep. 2018, doi: 10.1109/TEC.2018.2828027.

[75] B. Bilgin and A. Emadi. “Electric motors in electrified transportation: A step toward achieving a sustainable and highly efficient transportation system,” *IEEE Power Electronics Magazine*, volume. 1, no. 2, pp. 10-17, (2014).

[76] B. Bilgin, P. Magne, P. Malysz, Y. Yang, V. Pantelic, M. Preindl, A. Korobkine, W. Jiang, M. Lawford, and A. Emadi, "Making the case for electrified transportation," *IEEE Transactions on Transportation Electrification*, vol. 1, no. 1, pp. 4-17, 2015.

[77] Z.Q. Zhu and David Howe, "Electrical machines and drives for electric, hybrid, and huel cell vehicles," *in Proceedings of the IEEE*, vol. 95, no. 4, pp. 746-765, 2007.

[78] Shinetsu Rare Earth Magnet. [Online]. Available: http://www.shinetsurare-earth-magnet.jp/e/topics/pdf/detail_20_03.pdf.

[79] KISTI [Online]. Available : http://www.koreascience.or.kr/article/JAKO201432558388395.pdf

[80] L. Chen, X. Cao, S. Guo, J. Di, G. Ding, C. Yan, R., et al. “Coercivity enhancement of Dy-free sintered Nd–Fe–B magnets by grain refinement and induction heat treatment,” *IEEE Trans. Magn*., vol. 51, no. 11, 3- pages, Nov. 2015.

[81] C. Lin, H. Peng, J. W. Grizzle, and J. Kang, “Power management strategy for a parallel hybrid electric truck,” IEEE Transactions on Control Systems Technology, vol. 11, no. 6, pp. 839-849, Nov. 2003.

[82] V. Freyermuth, E. Fallas, and A. Rousseau, "Comparison of powertrain configuration for plug-in HEVs from a fuel economy perspective," SAE International, 2007.

[83] J. Liu, "Modeling, configuration and control optimization of power-split hybrid vehicles," Ph.D. dissertation, Horace H. Rackham School of Graduate Studies, The University of Michigan, Ann Arbor, MI, United States, 2007.

[84] Jim Harrison, “The technology behind the soon-to-arrive Chevrolet Bolt EV”, Electronic Products [Online]. Available: https://www.electronicproducts.com/the-technology-behind-the-soon-to-arrive-chevrolet-bolt-ev/

[85] Romain Nicolas, “The 2016 Volt and its Voltec propulsion system”, Car engineer [Online]. Available: https://www.car-engineer.com/2016-volt-voltec-propulsion-system/

[86] PRESSROOM, “CHEVROLET SHOWCASES SPARK EV ELECTRIC MOTOR”, CHEVROLET [Online]. Available: https://media.gm.com/media/us/en/chevrolet/news.detail.html/content/Pages/news/us/en/2011/Oct/1026_spark_elec_mtr.html/

[87] R. Tsunata, M. Takemoto, S. Ogasawara, K. Orikawa, "Variable Flux Memory Motor Employing Double Layer Delta-Type PM Arrangement and Large Flux Barrier for Traction Applications", *IEEE Trans*. *Ind*. *Appl*., vol. 57, No. 4, pp. 3545-3561, 2021.

[88] J. H. Kwack, S. J. Min, and J. P. Hong, “Optimal stator design of interior permanent magnet motor to reduce torque ripple using the level set method,” IEEE trans. Magn., vol. 46, no. 6, pp. 2108-2111, Jun. 2010.

[89] Nissan leaf motor specification. [online (confirmed on Jan. 26, 2022)]. Available: https://www.nissanusa.com/vehicles/electric-cars/leaf/specs/compare-specs.html#modelName=S|40%20kWh

[90] Magnetic Hysteresis [online (confirmed on Jan. 26, 2022)]. Available: https://www.electronics-tutorials.ws/electromagnetism/magnetic-hysteresis.html

[91] Automotive Industry Portal MarkLines [online (confirmed on Jan. 26, 2022)]. Available: https://www.marklines.com/en/report_all/rep1879_201906#:~:text=The%20THS%20II%20drive%20motor%20has%20a%20maximum%20power%20output,the%20magnetic%20circuit%20and%20core

Publication

This Ph.D. study has resulted in following publications:

Journal Paper:

J. Park, R. Tsunata , M. Takemoto, S. Ogasawara, K. Orikawa, S. Ogasawara "Hybrid-Type PM Motor for Electric Vehicle Traction with improved Reluctance Torque", *Journal of the Japan Society of Applied Electromagnetics and Mechanics (JSAEM)*, Vol30, No.3, pp.324-334, 2022

Conference Paper:

J. Park, R. Tsunata , M. Takemoto, S. Ogasawara, K. Orikawa, S. Ogasawara "Evaluation of Switching Ripple Effect on Efficiency of Novel Spoke-Type IPMSM Using Dy-Free Magnet - Comparison to IPMSM using NbFeB Magnet" *in Proc. of IEEE International Conference on Electrical Machines and Systems (ICEMS 2022)*, Online, Nov/Dec. 2022.

J. Park, R. Tsunata , M. Takemoto, S. Ogasawara, K. Orikawa, S. Ogasawara "Investigation of Dy-Free Hybrid PM Motor Based on Spoke-Type Rotor for Automotive Applications" *in Proc. of IEEE International Electric Machines & Drives Conference (IEMDC2021)*, pp.1-8, online, May. 2021, DOI: 10.1109/IEMDC47953.2021.9449493

J. Park, R. Tsunata , M. Takemoto, S. Ogasawara, K. Orikawa, S. Ogasawara "Design of Hybrid-Type PM Motor for Electric Vehicle Traction using Trapezoidal Ferrite-PM to improve Reluctance Torque" *in Proc. of IEEE International Magnetics Conference (INTERMAG2021)*, France, April. 2021.

Acknowledgments

This thesis was written while the author was a doctoral student at Hokkaido University. There was a lot of help and hard work from many people for the writing of this thesis. First of all, I would like to express my deep gratitude to my advisor, Professor Takemoto of Okayama University. He helped me a lot to learn a creative perspective in motor research. I would also like to express my deep gratitude to Professor Ogasawara, who has always been a diligent researcher, an excellent advisor to the students, and a model for the laboratory. I would also like to express my gratitude to Professor Orikawa, who drank a lot with me on a hot spring trip. Professor Tsunata, who guided me and helped me on my first day of school at Hokkaido University. Sometimes like a teacher, sometimes like a friend, thank you so much for helping me in many ways. I think the time spent with such great professors is a precious asset that cannot be exchanged for anything.

I would also like to thank Tao-kun and Nakazawa-kun, who are my classmates. Also, I would like to express my gratitude to Kajii-kun and Suzuki-kun who helped me a lot because I was not good at Japanese.

I would also like to express my deep gratitude to my supervisor at work, Lee kyeong-hoon, Director of Development at LG Electronics, who recommended the degree course. I would also like to express my gratitude to Professor Yongmin Yoo of Honam University and Dr. Daun Choi who gave advice in various ways for the preparation of the thesis. I would also like to express my gratitude to Researcher Jiwon Lee, who supported research samples and research materials. I would like to express my gratitude to Kang-Min Yoo, Hyo-Eun Lee, and Nyeong Wang, who worked together at the company before entering the school. I am deeply grateful to Professor Jeong Sang-yong, who guided me as an advisor during the master's course. At that time, he taught me a lot and gave me a lot of insight. They have become a great strength to me now. Senior Seongil from the Faculty of Agriculture, Hokkaido University, I just want to thank you for giving me so much.

I also express my gratitude to my father and mother. May both of you always be healthy. I would also like to express my gratitude to my father-in-law and mother-in-law who helped me a lot. I would also like to express my gratitude to my sister-in-law, Kim Da-jeong, who took care of and cherished the children closely.

Above all, I would like to express my love and gratitude to my wife Kim Si-eun, who has always supported, cared for, and helped me. Lastly, my children Seojin, Seoah, and Seowoo. Dad always supports you and loves you.